Politecnico di Torino

ScuDo
Scuola di Dottorato ~ Doctoral School
WHAT YOU ARE, TAKES YOU FAR

Doctoral Dissertation
Doctoral Program in Chemical Engineering (35^{th}cycle)

Fluid dynamics and mass transfer in porous media

Modelling fluid flow and filtration inside open-cell foams

By

Enrico Agostini

******

Supervisor(s):
Prof. Daniele Marchisio, Supervisor
Prof. Gianluca Boccardo, Co-Supervisor

Doctoral Examination Committee:
Prof. Urs Peuker, Referee, Technische Universität Bergakademie Freiberg
Prof. Niels Deen, Referee, Eindhoven University of Technology
Prof. Paolo Canu, Università degli Studi di Padova
Prof. Stefania Specchia, Politecnico di Torino
Prof. Rajandrea Sethi, Politecnico di Torino

Politecnico di Torino
2023

Declaration

I hereby declare that, the contents and organization of this dissertation constitute my own original work and does not compromise in any way the rights of third parties, including those relating to the security of personal data.

Enrico Agostini
2023

* This dissertation is presented in partial fulfillment of the requirements for **Ph.D. degree** in the Graduate School of Politecnico di Torino (ScuDo).

Acknowledgements

I would like to acknowledge Politecnico di Torino and DISAT for the financial and technical support during these years of research. I would like to express my gratitude to my supervisors Daniele Marchisio and Gianluca Boccardo, for their support, guidance and advises throughout the project. I also would like to acknowledge IFP Energies Nouvelles for hosting me multiple times as a visiting Ph.D. student and for making available precious laboratory hours as well as computational resources. A special thanks goes to Frederic Augier, Yacine Haroun, Marion Servel, Maxime Moreaud and Floriant Montjovet for their guidance and advice which was fundamental for the progress of this Ph.D. project. I would also like to extend my thanks to my collegues at Polito and IFPEN for their support and friendship during these years. A special thank to my family and friends on whom I could always count on for help and support. Finally, but most importantly, thanks to Giulia, who was there the whole time, by my side, who kept me sane throughout the all process, giving me good advises and supporting me without questions.

Abstract

Open-cell foams are porous materials characterized by high porosity and large specific surface, industrially employed as catalyst supports or particulate filters. The work reported in this manuscript aims to propose possible methodologies for the modeling of the geometric structure of these materials, using in-silico tools for their generation and Computational Fluid Dynamics (CFD) numerical simulations for the investigation of the transport phenomena of a fluid flowing within the porous medium. Moreover, the performances of solid foams for the filtration of colloidal and fine particles are investigated with CFD and analyzed by means of classic clean-bed filtration models, commonly employed for the evaluation of the deposition efficiency. The first Chapter introduces open-cell foams and their principal geometric and morphological features as well as giving an outline of the state of the art in the literature for such porous media, focusing on the use of CFD and other computational methods for the generation of the geometry and the transport phenomena investigation. The second Chapter provides a synthesis of the equations governing the simulated systems and the framework used for the analysis of the filtration phenomena. Furthermore, the theoretical background of the main algorithm used for the generation of foam digital geometries is reported, with particular focus on the ideal Kelvin's Cell model, the random Voronoi tessellations and the processing of binary images. Chapter 3 introduces and tests an open-cource workflow able to reproduce a great varieties of geometries and numerically explore the flow field and mass transfer on the created geometries, eventually obtaining an effective deposition rate coefficient K_d. The results, interpreted using known constitutive equations and other functional forms of the main geometric descriptors, are insufficient in explaining the variations in filtration performances, highlighting the need for both more detailed exploration and modelling. This last issue is tackled in Chapter 4, where an updated and improved geometry generation workflow is proposed and validated. Pressure drops measurements across foam pellets samples, ceramic and metallic, are obtained

both via experiments and through CFD simulations using geometries reconstructed from tomography images. The workflow is tested by generating replicas of the examined foams: a geometric comparison shows that the in-silico workflow is able to reconstruct models whose common porous media macro-descriptors, porosity, specific surface and tortuosity, lie within a 5-6 % range compared to the original foams. Also from the fluid dynamic point of view the results of the CFD simulations using the replicas are in good agreement with both experiments and simulations on the digitally reconstructed real foams. The novel in-silico tool proves to be accurate in reproducing the behavior of real foams as well as effective, because of the low computational costs required to generate a digital sample. Chapter 5 focuses on a practical problem affecting the refinery industry, the separation of fine particles from hydrocarbon streams ahead of catalytic reactions. The system is simulated coupling CFD for the solution of the flow field and Lagrangian simulations for the calculation of the particles trajectories. The model is first validated by comparing the results obtained for a granular bed configuration with the deposition model proposed by Yao [1]. Then, the same methodology is employed to three ceramic foams geometries, with the aim of identifying which characteristic lengths can be used to describe the deposition phenomena interpreted according to the filtration model of Yao. The results highlight how the complex structure of the materials in exam can not be described by a single geometric parameter and stress the need of further detailed investigation on the topic. Finally, Chapter 6 concludes the manuscript, identifying the main results and proposing possible future perspectives on the topic and potential applications for the workflow presented.

Contents

List of Figures

List of Tables

Nomenclature

Roman Symbols

δ_{Eucl}	Euclidean Distance
δ_{geod}	Geodesic Distance
$\langle c \rangle$	Average Particle Concentration
$\mathscr{D}$	Diffusion Coefficient
As	Happel Function
Da	Advective Damköhler Number
Pe	Peclèt Number
Re	Reynolds Number
ρ_p	Particle Density
τ_0	Particles Relaxation Time
a	Kelvin's Cell Edge Length
A_{surf}	Superficial Area of Porous Matrix
c	Scalar Particles Concentration
C_0	Inlet/Upstream Particle Concentration
C_{KC}	Kelvin's Cell Coefficient
$CV(x)$	Coefficient of Variation of Size Distribution

d_C Foam Cells Average Diameter

d_c Collector diameter

D_g Granular Bed Grain Diameter

d_h Foam Hydraulic Diameter

d_h Hydraulic Diameter

d_p Particles Average Diameter

D_pore Foam Pore Diameter

d_S Foam Struts Average Diameter

d_W Foam Windows Average Diameter

$d_{3,2}$ Foam Sauter Diameter

$E(x)$ Expected Value

$F_{tot}^{in}(c)$ Total Inlet Particles Flux

$F_{tot}^{out}(c)$ Total Outlet Particles Flux

F_i Generic Force Acting on Particles

g Gravitational Accelleration

$g(\varepsilon)$ Kuwabara Function

h Heat Transfer Coefficient

k Porous Medium Permeability

k_B Boltzmann Constant

k_b Reaction Rate Coefficient

K_d Effective Deposition Rate

k_d Particles Deposition Rate

k_L Mass transfer Coefficient

L	Bounding Box Size
L_0	Solid Collector Characteristic Length
m_p	Particle Mass
N	Node Radius Size in Voxel
N_{tot}^{sph}	Number Total Packed Spheres
P	Macro-scale Fluid Pressure
P	System Pressure
p	Hydrostatic Fluid Pressure
P_i	i-th Point in 3D Space
q	Superficial Velocity in Porous Media
q	Superficial Velocity
R_{edge}	Radius of Foam Skeleton Edge
R_{node}	Radius of Foam Skeleton Node
R_{sph}	Radius of Aggregated Spheres
S	Strut Radius Size in Voxel
S_V	Specific Surface
T	System Temperature
t	Time
tv	Closing Operation Size in Voxel
U	Fluid Pore-scale Velocity
$U_{p,i}$	Particle Velocity
V	Darcian Velocity
V_0	Superficial Velocity at Computational Domain Inlet

V_{total} Total Volume of Porous Matrix

V_{void} Void Volume of Porous Matrix

x Generic Spatial Coordinate

x_{inlet} Inlet X Coordinate

x_{outlet} Outlet X Coordinate

St Stokes number

Greek Symbols

α Sphere Aggregate Compactness Factor 1

α_D Particles Attachment Efficiency

β Sphere Aggregate Compactness Factor 2

β_I Inertial Friction Coefficient

Δ Difference

η_0 Single Collector Efficiency

η_B Single Collector Diffusive Mechanism Efficiency

η_G Single Collector Sedimentation Mechanism Efficiency

η_I Single Collector Interception Mechanism Efficiency

η_{glob} Global Deposition Efficiency

γ Macroscopic Friction Coefficient

γ_H Happel Coefficient

μ Fluid Viscosity

μ_S Sphere Distribution Average Size

ν Fluid Kinematic Viscosity

Ω Total Domain Volume

Ω_b Total Fluid Volume

ρ Fluid Density

σ_S Sphere Distribution Standard Deviation

τ_r Particle Relaxation Time

ε Porous Medium Porosity

Superscripts

in Inlet

out Outlet

Subscripts

as Asymptotic

dual Foam Corresponding Dual Packing

i, j Generic Subscript Indexes

min Minimum

sph Spheres

tot Total

Other Symbols

$\mathtt{Al_2O_340}$ Alumina 40 PPI Foam

$\mathtt{Al_2O_360}$ Alumina 60 PPI Foam

$\mathtt{Al_2O_320}$ Alumina 20 PPI Foam

`NiCr14` Nichel-Chrome 14 PPI Foam

`NiCr30` Nichel-Chrome 30 PPI Foam

f_{scale} Isotropic Scaling Factor

R Sphere Radius Size in Aggregate

$Repul$ Repulsion Distance Sphere Aggregate

Acronyms / Abbreviations

$\mu - CT$ Micro Computed Tomography

CFD Computational Fluid Dynamics

DPM Descrete Particles Method

KC Kelvin's Cell

PPI Pore Per Inch

REV Representative Elementary Volume

Chapter 1

State of The Art

1.1 Porous materials in the process industry

Porous media are a class of materials characterized by pores, which are void volumes inside a *matrix* of solid, which constitute the main structure. These materials can be commonly found in nature, e.g. sand, soil, fractured rocks underground, but are also of great importance in the field of the process industry and chemical engineering equipment, such as packed bed reactors. Most commonly, these reactors fillings are made of spherical beads and are of great importance in the field of heterogeneous catalysis and filtration beds. Beside spherical particles, many other kind of shapes have been designed and are used for catalytic applications, such as cylindrical pellets, Raschig rings and other more complex types. Another example are the fixed bed reactors, whose filling media are made of rigid porous materials, such as honeycomb or other ordered lattices monoliths, characterized by an ordered pore structure, or open-cell foams, which instead are characterized by an un-ordered and often random pore-structure. The solid structure, the shape and sizes of the grains or the pores and the void fraction for a given volume can change significantly between different types of media. However, there is a set of macro-descriptors that are commonly used to describe and compare different types of media, to quantify their ability to let fluids flow through them, or the amount of *dead* zones where fluid remains trapped. These properties are:

- *Porosity*, usually indicated with the greek letter ε, represents the void fraction of a porous medium and it is defined as $\varepsilon = V_{void}/V_{total}$. Porosity can be

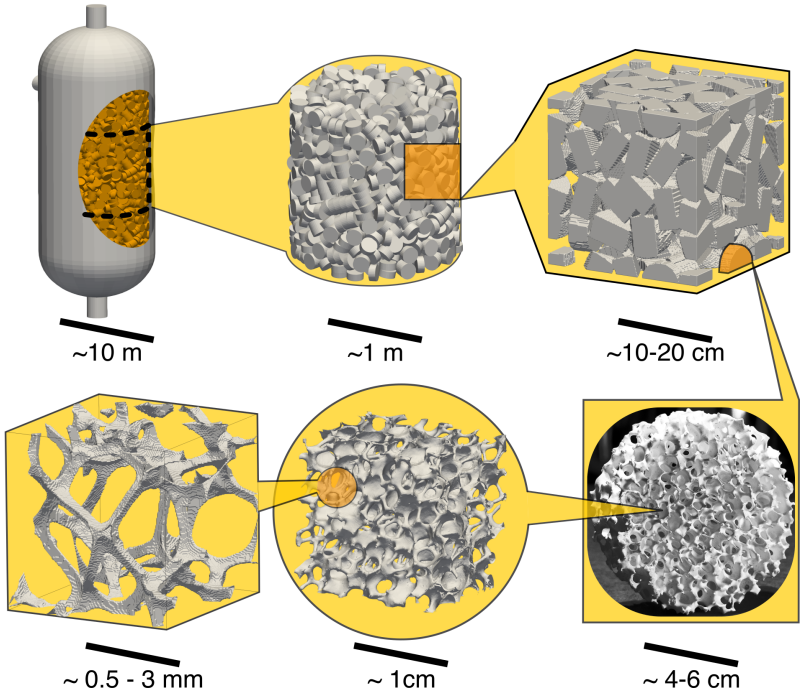

Fig. 1.1 An example of the different scales coming into play when porous media are used as packing materials for reactors in the process industry. At each scale different approaches can be used, and different properties can be measured. For instance, representative elementary volumes have different size according to the scale in exam. Another example is the porosity ε, which has different reference values if measured at the pore scale or at the foam pellet scale and so on.

measured at different scales, from the nano-scale for catalyst particle up to the the meters, in case of a packed bed catalytic reactor charge;

- *Specific Surface*, usually indicated as S_V, it is defined as the ratio between superficial area of a porous material and the volume of the whole sample, $S_V = A_{surf}/V_{sample}$. The higher the value of the specific surface, the larger is the exchange surface for transport phenomena, given a fixed volume;

- *Permeability*, indicated with the letter k, it measures the intrinsic ability of a porous material of letting fluids flow through it with more or less resistance. Low permeable materials are rocks made of limestone or granite ($k \approx 10^{-9} - 10^{-10}$ m/s). Oil reservoir rocks or fractured rocks have higher values ($k \approx 10^{-6} - 10^{-8}$ m/s). Sand and granular beds are on the upper side of the permeability scale ($k \approx 10^{-5} - 10^{-8}$ m/s) and even higher are highly porous materials such as open-cell foams;

- *Tortuosity*, indicated with the greek letter τ, it is defined as $\tau = \delta_{geod}/\delta_{Eucl}$, $\tau \geq 1$, which is the ratio between the effective distance travelled by a fluid flowing through two points in a porous material (δ_{geod}) and the Euclidean distance between those points (δ_{Eucl}) . It is important in characterizing porous media because it gives an indication regarding residence time, presence of dead zones, hydraulic dispersion and it influences pressure drops, and many other transport phenomena. There is not a unique way of calculating it, since many authors defined it differently, depending on the phenomena in exam.

1.2 Open-cell foams

Let's now come to the subject of this manuscript, by focusing on open-cell foams and their properties. These porous materials have seen an increase in interest and usage over the last twenty/thirty years, because of their peculiar characteristics: they are characterized by an open cellular structure, with porosity ranging between 75 to 95 % and a very high bulk specific surface [4]. The combination of these factors results in the features for which they became appreciated: lower pressure drops compared to classic reactor packings, such as granular beds, and improved radial heat and mass transfer due to reduced channeling effects [5]. Notable uses of ceramic

foams are: molten metal filters [6], catalyst supports [5, 7, 8], soot filters [9], column packing for packed bed reactors [10]. Metallic foams are also commonly used as filters, catalyst supports and reactor or heat exchanger filling material due to their great performances in heat transfer applications([11]). The classic manufacturing process involve inflating a gas, usually air, into molten polymers and inducing polymerization. The polymeric structures obtained are then impregnated by ceramic pastes/slurries or metallic powders, together with wetting and binding agents. Finally these wet foams are calcinated, obtaining a *positive* replica of the polyurethane foams. The foams manufactured through this process have the peculiarity of presenting hollow ligaments, due to the destruction of the polymeric foam inside. Many other techniques have been developed in recent years, such as direct blowing of melted metal alloys or metallic powders sintering [12]. As a result of these manufacturing techniques open-cell foams are monolithic structures composed by a solid skeleton. Three elements can be identified to describe the microscopic geometry: the *cells*, which are the macroscopic alveoli, the *windows*, which are the channels connecting each cell with the neighbouring one and finally the *struts*, which are the solid structuring elements of the porous materials. Figures 1.2a,1.2b show an example of Al_2O_3 foam pellets, 20 and 40 PPI respectively, Fig. 1.2c show an example of metallic aluminum piece of foam, whereas Fig. 1.2d highlights the geometrical features mentioned above.

Because of the increasing potential applications of these porous media the modeling and characterization of open-cell foams is of great importance but remains a challenging issue. Often the main parameters used as describing metrics are the porosity ε and the *pores per inch* (PPI), a number indicating the average pore dimension. However, these parameters does not lead to any direct estimation of important descriptors such as the specific surface S_V, required for the estimation of transport coefficients, such as the pressure drops $\Delta P/L$ or the heat and mass exchange coefficient h and k_L, necessary for the design of industrial equipment. Moreover, a better understanding of the geometric structure and its interaction with the transport phenomena occurring inside the foams is crucial to address the problem of the design optimization of the foam structure for different applications, which remains an open problem.

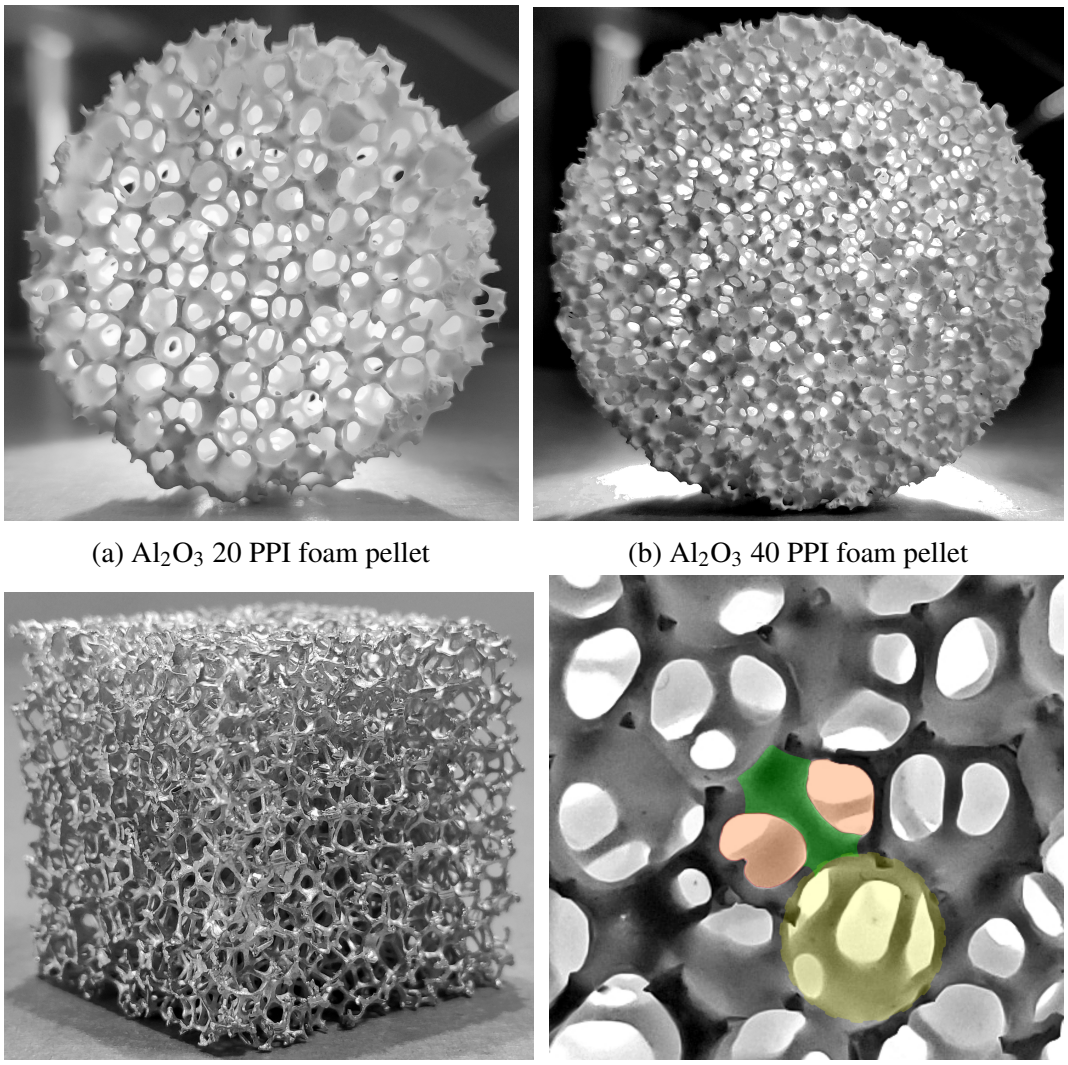

(a) Al_2O_3 20 PPI foam pellet

(b) Al_2O_3 40 PPI foam pellet

(c) Aluminum 20 PPI foam pellet

(d) A detailed view of the foam pellet

Fig. 1.2 The first and second image from the top show two Al_2O_3 foam pellets, reprectively 20 and 40 PPI, used during the experimental phase of this work. The image on the second row, on the right, show a metallic Aluminum piece of foam. Finally, the fourth image highlight with colors the geometrical features of open-cell foams : in green the outline of a *strut*, in red two *windows* adjacent to the strut and in yellow the volume delimited by a *cell*.

1.3 Modeling open-cell foams

Over the years many attempts have been made to address the modeling of the geometry of foams. At first ideal periodic geometries were the most common because of their simplicity and repeatability in space. However, the need to capture the randomness of the foams structures required the use of more complex approaches, leading to the use of tessellation algorithms, which generate random graphs that closely resemble the skeleton of ceramic or metallic foam and are able to capture the random structure of real open-cell foams. This section offers a brief summary of the most common geometric models used to describe the structures of open-cell solid foams.

1.3.1 Ideal periodic models

The term *ideal periodic models* refers to ideal convex polyhedra, with regular polygonal faces, which can perfectly fill the space in a repeating fashion, forming a structure with congruent repeating cells. The advantage of using such geometries resides in the fact that analytical correlations can be derived to describe the geometrical structure, such as edges length, area of the windows and the volume of the pores. This also allows for an easier estimation of the porosity and specific surface. Common polyhedra with such properties are cubes, dodecahedra and truncated octahedra, also known as *tetrakaidecahedron*. The latter is the shape that Lord Kelvin [13] proposed for the description of a foam or froth produced by soap bubbles. The reason resides in the fact that this polyhedron attains minimal surface tension. This structure, better known as *Kelvin's cell*, has 14 faces (6 squares and 8 hexagons) and 36 edges of equal size. The tetrakaidecahedron is still widely considered the ideal shape that a solid foam cell would attain if the structure would be allowed to reach equilibrium during the synthesis process. A graphical representation of the tetrakaidecahedron and the *Kelvin's cell* is reported in Fig. 1.3.

Many authors used the Kelvin's Cell as a geometric model in their investigation of transport phenomena inside porous open-cell foams. In their review on solid foams and their application in the process industry Twigg and Richardson [4] reported analytical correlations for the estimation of the specific surface S_V, pressure drops $\Delta P/L$ and heat transfer coefficients h, based on the Kelvin's cell geometry. Sullivan et al. [14], proposed a general geometric model based on the tetrakaidecahedron reporting

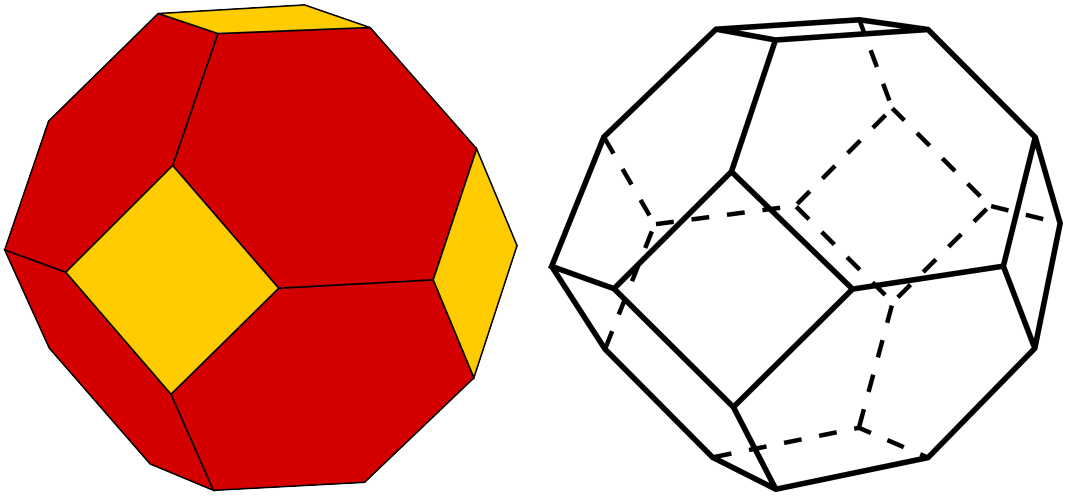

(a) A truncated octahedron (b) A Kelvin's Cell structure

Fig. 1.3 The image on the left shows a *truncated octahedron*, or *tetrakaidecahedron*, obtained truncating an octahedron with a smaller cube, which cut out the vertices. It has eight hexagonal and six square faces. On the right, the geometrical representation of the Kelvin's Unit Cell: the edges of the cell are the *struts* of the ideal foam model, the *windows* are composd by the faces of the polyhedron. Finally the foam *cell* is represented by the whole periodic unit cell. This polyhedron is space filling, thus it can be repeated along its periodic direction and form an ordered lattice, representing an open-cell foam.

several parametric correlation to describe such geometrical structure based on the edge length L, varying the aspect ratio of the cell. Incera Garrido et al. [15] proposed mass transfer and pressure drops correlations based both on experimental measurements and analysis of geometries obtained with an MRI technique, highlighting the influence of the pore size and porosity. Inayat and co-authors [16–18] developed analytical geometrical correlations based on the Kelvin's Cell model comparing them to data obtained by characterization of real foams with μ-CT tomography. Kumar and Topin [19] used an analytical approach, based on the tetrakaidecahedron unit cell, to investigate the thermohydraulic aspects (pressure drops and thermal conductivity) of several different foams structure, comparing a large amount of experimental results found in literature. Ambrosetti et al. [20] developed a very detailed analytical model, based on experimental data. Della Torre et al. [21] used the Kelvin's Cell model for numerical simulations of a catalytic reaction in open-cell foams substrates.

1.3.2 Adding complexity: random tessellations

To overcome the limits imposed by a simplified analytical model, such as the Kelvin's Cell, many authors focused their research on developing more realistic approaches, in order to better describe the random nature of open-cell foams. Lautensack et al. [22], Redenbach et al. [23], Wejrzanowski et al. [24], were among the first to propose the use of random tessellations as an optimal model to represent the cellular random nature of solid foams. Random Voronoi or Voronoi-Laguerre algorithms subdivide the space into regions, which can be taken to represent the pores of a real foam. Fig. 1.4 shows an example of two and three-dimensional Voronoi and Voronoi-Laguerre diagrams. The generation of a tessellation starts from a initial set of point, called *seeds*, that are usually randomly distributed in the computational space of the tessellation algorithm. Then, the tessellation algorithm computes the subdivision of space into *cells*, creating a cellular structure that forms the core of the foam model. The advantage of this approach lies in the fact that a large range of parameters affecting the final geometry can be explored. This allows the creation and the study of many structures and configurations that would not otherwise be possible to experimentally investigate. Many authors, such as Bracconi et al. [25], Nie et al. [26, 27], Das et al. [28] used random tessellations to generate geometries and investigated transport phenomena using numerical simulations. Different algorithms and software were used by these authors to create the geometries: `LIGGGHTS` [29] or `LAMMPS` [30] to compute the initial random seeds of the tessellation, `voro++` [2] to compute the tessellations and `Surface Evolver` [31] to create the superficial mesh. These computational models are often used in combination with numerical simulations to study transport phenomena and fluid dynamics inside foam materials.

1.3.3 Fluid dynamics and CFD

The investigation of fluid dynamics inside porous media is made difficult by the complex nature of these materials and because of the small scale at which most of the phenomena occur. At a macroscopic level, global measurements (such as pressure drops or heat exchange) can be carried out to obtain some macroscopic/global transport coefficients. However, the investigation of what takes place at the scale of the pore is hindered by the costs and complexity required by experimental devices. For this reason, alongside analytical and experimental models, in the last 20 years

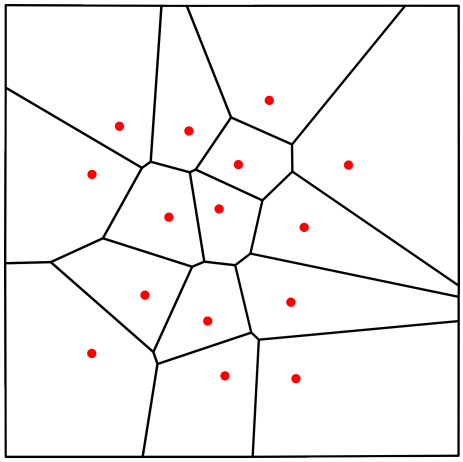

(a) A 2D Voronoi tessellation with its *seeds*

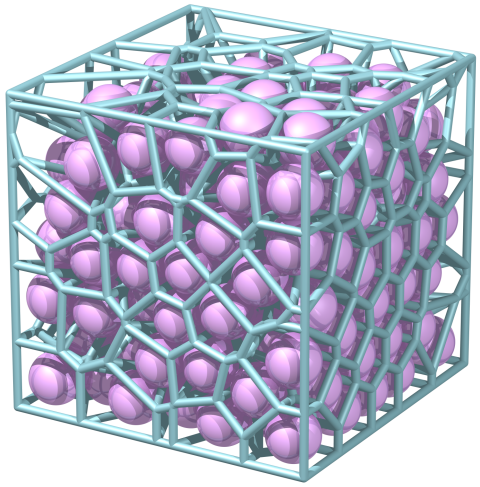

(b) A 3D Voronoi tessellation with its *seeds*

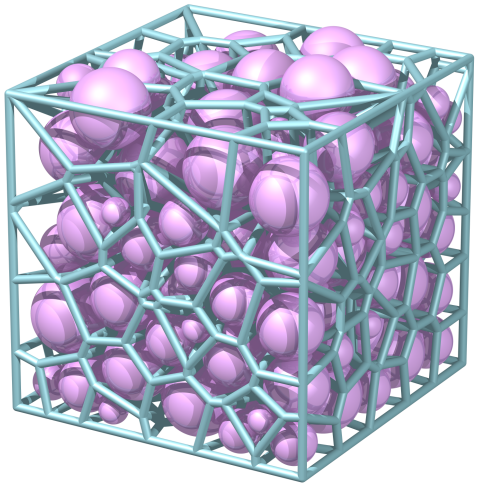

(c) A 3D Voronoi-Laguerre tessellation with its *seeds*

Fig. 1.4 The first image represents a two dimensional Voronoi tessellation in a confined square box. The red dots are the starting seeds of the algorithm which subdivides the space accordingly. The second and third image are a three-dimensional representation of a Voronoi and Voronoi-Laguerre tessellation, respectively: the spheres inside each cell are once again the original seed of the algorithm. For the Laguerre-Voronoi case, the spheres have different sizes. It is clear the analogy between the structure generated by such random tessellation and the underlying skeleton of an open-cell foam: the edges of diagram are the *struts* of the in-silico foam, the *windows* are composed by the faces between neighbouring polyhedral cells. Fig. 1.4b and 1.4c are taken from [2].

many authors used numerical methods to study and characterize the fluid dynamics inside porous materials. The first system to be widely explored were spherical granular beds, for their great importance in the process industry. For instance, Boccardo, Icardi and their co-authors [32–35]) carried out several studies using numerical simulations to investigate the micro-scale fluid dynamics of randomly packed spherical beds. The use of CFD numerical simulation for the solution of the flow field and the exploration of the transport phenomena inside open-cell foams is well reported in literature: the work of Krishnan et al. [36] is one of the first reported, studying fluid flow and pressure drops with DNS methods. The works of Lucci and co-authors [37–39] focused on momentum, heat, mass transfer and catalytic reactions using a regular and a randomized Kelvin's cell model coupled with CFD. For the same geometrical model Della torre et al. [40] explored the flow field over different fluid dynamic regimes. Das et al. [41, 42] and Chandra et al. [43] studied momentum and mass transfer inside a periodic Kelvin's cell using CFD with an *Immersed Boundary Method*. As already cited in the previous section many authors ([25–28]) used numerical methods to solve the flow field inside geometries generated using random tessellations. The great number of works using numerical simulations as a tool for the investigation of micro-scale transport phenomena, of which the previously cited ones are but a small fraction, show how much importance and reliability CFD simulations have acquired in the last years in the in the field of fluid dynamics modeling of porous media.

1.4 Structure of the manuscript

What is reported in the previous sections testifies the significant increase in interest towards open-cell foams over the past years. Many authors proposed different types of model for the geometric structure and correlations for the estimation of pressure drops or heat and mass transport coefficients. However, even now a great deal of knowledge is missing regarding the influence that the specific geometric features characterizing open-cell foams have on the transport processes. Moreover, the optimization of the geometric structure for specific areas of application remains an open problem. To approach such issues it is crucial to develop an *in-silico* tool that is able to generate a great variety of structures, exploring large parameter ranges. The aim of this work is to propose, test and validate different approaches towards the

generation of digital open-cell foams models and investigate the transport phenomena occurring between fluid and solid matrix, with particular focus towards filtration applications.

The following brief overview of the work will serve as a reading guide of the organization of the chapters composing this manuscript.
Chapter 2 gives a theoretical background regarding the flow of an incompressible fluid inside porous media, the mass transport and particles deposition and filtration phenomena. Then the main theoretical concepts used for the creation of in-silico foam geometries, originated both from tomography images or digitally generated, will be addressed: random tessellation algorithms, the generation of their starting seeds, and the processing of binary images.
In **Chapter** 3 a workflow for the generation of different *balls-and-sticks* foam models is presented and tested. The geometries thus obtained are used to investigate and solve the fluid flow of an incompressible fluid. Then the scalar transport equation is solved to investigate phenomena associated with the deposition of colloidal particles on the foam walls. Different geometric models are digitally explored: the Kelvins's Cell, mono-disperse and poly-disperse Voronoi-like structures. Hydraulic permeability and filtration efficiency are calculated for each model and compared.
In **Chapter** 4, an innovative and improved foam generation workflow is proposed. This novel procedure is tested and validated both from a geometric and a fluid dynamics point of view. Four types of real foam samples are used to carry out pressure drop measurement on packed column set-up. Then, the geometry of such samples is digitally reconstructed from X-ray tomography images. Numerical simulations of the fluid flow are carried out on both the digitally reconstructed foams and the digital replicas geometries generated with the proposed workflow. This work has been carried out in collaboration with *IFP-Energies Nouvelles*.
While the topics exposed in Chapter 3 and 4 are more focused on the methodology proposed and its testing and validation, the main topic of **Chapter** 5 addresses a more practical problem of the process industry: the purification of hydrocarbon streams fed to a catalytic packed bed, from iron oxide fine particles. The investigation was carried out in close collaboration with *IFP-Energies Nouvelles*. The fluid flow is solved using CFD simulations, and Lagrangian Discrete Particle Model (DPM) ones are used to solve the particles trajectories. This method is first tested on a granular bed configuration and then filtration efficacy of open-cell foams is compared with results obtained from classical filtration models ([1]) to validate the results and

retrieve the characteristic parameters involved in the filtration process.
In **Chapter** 6 the final conclusion on the topic of this research work will be drawn, with particular focus on the objectives of the different subjects taken into account and the models proposed. Finally, future perspectives on the use of the proposed workflows and where their use could give a better understanding on open-cell foams as well as improve and optimize their applications, in the field of the process industry, will be addressed.

Chapter 2

Governing Equations

In this chapter, the main notions and governing equations for single-phase flow in porous media, particle deposition, scalar transport, and Lagrangian particle simulations will be covered and explained. Particular care will be given to the analysis and modelling of surface particle deposition processes, since it is the focus of two chapters of this work. Finally, the geometrical tools to generate in-silico the geometries used throughout the work will be described in detail.

2.1 Single-Phase Flow in Porous Media

The characteristic length scale involved in transport phenomena inside porous media is very small: the pores have dimensions of the order of hundreds of μm. However, the continuum hypothesis still holds true, and for this reason the governing equations of a fluid moving through an open-cell foam are the continuity and the Navier-Stokes equations, which for an incompressible fluid, with constant density ρ and viscosity μ, read as follow:

$$\frac{\partial U_i}{\partial x_i} = 0 \tag{2.1}$$

$$\frac{\partial U_i}{\partial t} + U_j \frac{\partial U_i}{\partial x_i} = -\frac{1}{\rho}\frac{\partial p}{\partial x_i} + \nu \frac{\partial^2 U_i}{\partial x_j^2} \tag{2.2}$$

where U_i is the i-th component of the fluid velocity, p is the fluid pressure, and ν is the fluid kinematic viscosity. Here the Einstein or index notation has been used. These are the equations that are discretized and solved by a Computational Fluid Dynamics (CFD) software. In most cases the porous media systems under investigation have extensive dimension, with a huge number of pores, thus it would be impractical to describe the results of the solution of the flow field of a fluid through the medium using a micro-scale formulation. Therefore, it is necessary to use a macro-scale description, which is the result of an averaging operation carried out on the microscopic element of the geometry in exam. This procedure, well explained by Whitaker [44], is a spatial *smoothing* of the micro-scale equations, leading to a new macro-scale continuum formulation which entails a loss of distinction between the solid and the fluid fraction of the entire domain. Thus, the elementary element of the description is a solid-fluid zone, characterized by its porosity. The resulting equations are written as follows:

$$\frac{\partial V_i}{\partial x_i} = 0 \tag{2.3}$$

$$\frac{\partial V_i}{\partial t} + V_j \left(\varepsilon \frac{\partial V_i}{\partial x_i} \right) = -\frac{1}{\rho} \frac{\partial P}{\partial x_i} + g_i + \gamma V_i \tag{2.4}$$

where V_i is the Darcy velocity (or superficial velocity) in the porous medium, ε is the medium porosity and g_i is the i-th component of the gravitational acceleration. The friction coefficient γ can be expressed as $\gamma = \mu/\rho k$, where k is the porous medium permeability and μ is the fluid viscosity.

The earliest example of the use of such macroscopic approach for the flow of fluid though porous media is the search for a constitutive equation between the pressure drop measured across it and the inlet superficial velocity V_0. This means finding an analytical expression for the γ term of Eq. 2.4. A famous example is work of Henry Darcy [45] focused on the filtration system employed by the city of Dijon for purification of the ground water and for the design of its fountains. This work resulted in the well known *Darcy's Law*, which is still a relevant equation for the description of flow through porous media in general:

$$\frac{\Delta P}{L} = -\frac{\mu q}{k} \tag{2.5}$$

where $\Delta P/L$ is the pressure drop per unit volume and q is the superficial velocity. The linear relationship existing between q and the pressure drops, depends on the properties of the fluid, the viscosity μ, and the permeability of the porous medium k. This equation can be obtained directly from Eq. 2.4 under the hypothesis that the flow is stationary, in laminar regime, and gravity effects are unimportant. It is important to highlight the relationship between the velocity of the fluid inside the pores and the superficial velocity. Taking into account the cross-section of the porous medium, it is not entirely crossed by the fluid, since a fraction of this area is occupied by the solid medium. The ratio between the void and solid fraction is the porosity ε, and therefore a relationship between the pore scale velocity and the superficial one can be written as follow:

$$U = \frac{q}{\varepsilon} \tag{2.6}$$

Eq. 2.5 is very useful but it has a limited range of application, mainly in the field of aquifer flows. In the field of chemical engineering the velocities considered are much higher, thus it is necessary to characterize the flow regime. This can be done by introducing the Reynolds number, as reported by Bear [46]:

$$Re = \frac{qD_g}{\nu}, \tag{2.7}$$

where the term D_g is the characteristic length of the porous media. In case of a granular bed it uniquely refers to the average grain diameter, however for materials such as open-cell foams different characteristic lengths can be used: the average *cell* diameter, the average *windows* diameter, or the hydraulic diameter, which represent the ration between the surface area a sample of the porous media and the volume it occupies, $d_h = A/V$.

For conditions in which the inertial forces are more significant ($\mathrm{Re} > 10-20$), even if the flow is not fully turbulent, an additional term dependent on the superficial velocity V can be added to the friction factor, which becomes $\gamma = \mu/\rho k + \beta|V|$. Substituting in Eq. (2.5) as before, this yields the Darcy-Forchheimer's Equation:

$$\frac{\Delta P}{L} = -\frac{\mu|V|}{k} - \frac{\rho|V|^2}{k_1} \tag{2.8}$$

where $k_1 = 1/\beta_I$ is the inertial flow parameter or inertial permeability and like k depends only on the micro-structure of the porous medium.

2.2 Particle Transport and Deposition/Filtration

The description of the concentration of particles transported by the fluid, within a porous medium, is of great interest to describe phenomena such as the filtration of colloidal particles in the soil or capture/deposition of microscopic particles from flow-streams that can be detrimental to subsequent steps of an industrial process.

Depending on the dimensions of the particles to capture, different models can be used: if the particles are orders of magnitude smaller than the characteristic length of the flow or the obstacle, and unaffected by gravitational forces, then a Eulerian framework can be used. This is the case of of colloidal particles with sub-micrometer average size On the other hand, if the particles are larger and the density difference between solid and fluid is not negligible, then a Lagrangian framework must be adopted.

2.2.1 The Eulerian Framework

When using a Eulerian approach particle concentration and deposition can be described by a scalar transport and reaction equation. This is the case of the well-known advection-diffusion-reaction equation, which at the micro-scale is written as:

$$\frac{\partial c}{\partial t} + \frac{\partial}{\partial x_i}(U_i c) - \frac{\partial}{\partial x_i}\left(\mathscr{D}\frac{\partial c}{\partial x_i}\right) = k_b c \ \text{ on } \ \Omega_b \subset \Omega \subset \mathbb{R}^3 \tag{2.9}$$

with Ω_b the volume of fluid, Ω the total volume, c is the scalar concentration , U is the pore-scale velocity, which can be obtained by Eq. (2.2), and k_b is the bulk reaction coefficient. The diffusion coefficient $\mathscr{D}$, in the case of colloidal particles, is the diffusion due to the Brownian motion, and can be estimated using Einstein equation [47]:

$$\mathscr{D} = -\frac{k_B T}{3\pi\mu d_p} \tag{2.10}$$

where k_B is the Boltzmann constant, T is the system temperature, and d_p is the particles average diameter. This equation can be used to model the transport of colloidal particles under the assumption that the system concentration is low enough to be considered dilute, enabling to describe the diffusive flux with Fick's law. Moreover, the diameter of the particles in exam must be much smaller than the collector characteristic length, d_c, namely ($d_p/d_c \approx 10^{-3}$), as pointed out by Boccardo and co-authors [35]. Another necessary assumption for this kind of treatment is that the particles will follow the motion of the fluid along its streamlines: the particles Stokes number, namely the ratio between the characteristic time of the fluid flow and the relaxation time of the particles transported, will be very small, $\mathrm{St} \ll 1$. This condition is met for particles with average dimension around 1 μm or lower. Under certain conditions, such as those present in the early stages of filtration before a noticeable solid cake or deep solid deposits are formed, the deposition of colloidal particles on the solid wall of a collector (grains in a granular bed or struts of open-cell foams), can be modelled as an instantaneous reaction at the solid walls, where all the transported particles which come into contact with the collecting solid will irreversibly react (i.e. deposit) and disappear from the system. This is called then *clean-bed filtration* model of filtration [1]. This can be achieved in a numerical model by an homogeneous Dirichlet boundary condition $c = 0$ on the solid surface, meaning that all the colloids impacting on the walls of the collector are captured. The reacting term k_b in Eq. 2.9, is referred to a first-order homogeneous bulk reaction occurring in the fluid volume Ω_b, and for a system as the one in exam it will be considered equal to zero, since at the micro-scale all the reactions occur at the wall of the porous medium, and no bulk reaction is considered.

In analogy to the equation of motion, Eq. 2.9 has a corresponding macro-scale equation, obtained with the volume averaging procedure used for Eq. 2.4. This equation read as follow:

$$\frac{\partial \langle c \rangle \varepsilon}{\partial t} + \frac{\partial}{\partial x_i}\left(V_i \langle c \rangle\right) - \frac{\partial}{\partial x_i}\left(\mathbf{D}_h \frac{\partial \langle c \rangle \varepsilon}{\partial x_i}\right) = K_d \langle c \rangle \tag{2.11}$$

The averaging procedure is carried out over the whole porous domain Ω, and thus $\langle c \rangle$ is the average concentration of the scalar within the porous material, $\mathscr{D}_h$ is the scalar hydraulic dispersion, which is a tensor quantity, and K_d is the reaction/deposition rate at the macroscopic scale within the porous medium bulk. This last quantity takes into account all the reactive phenomena taking place within the porous matrix, either

at the solid walls, as in case of particle deposition or instantaneous reaction, or in the liquid domain at the pore scale.

2.2.2 The Lagrangian Framework

In a system with dispersed solid particles moving through a continuous medium, the trajectories of such particles can be solved with a Lagrangian approach, namely solving the balance of forces acting on individual particles. This method is implemented in the computational fluid dynamics software Ansys Fluent [48], through the equations that follow, which are those used for the simulations carried out in this work. This approach requires that the dispersed phase occupies a low volume fraction in the system, even if the mass flow-rate of the solid fraction is high, for instance in case of solid particle with density much higher than the fluid transporting them. Under such circumstances the particle is modelled as a *point mass*, that is a zero-dimensional point with a mass associated to it, traveling along the fluid flow, as reported by Loth [49]. The individual particle force balance is written as:

$$m_p \frac{\mathrm{d}U_{p,i}}{\mathrm{d}t} = m_p \frac{U_i - U_{p,i}}{\tau_r} + m_p \frac{g_i(\rho_p - \rho)}{\rho_p} + F_i \tag{2.12}$$

where g is the gravitational acceleration, m_p is the individual particle mass, $U_{p,i}$ is the particle velocity, ρ_p is the solid density, whereas U_i and ρ are the fluid pore-scale velocity and density, respectively. The particle relaxation time τ_r, is the characteristic time of a particle transported by a continuous fluid, and it is expressed as:

$$\tau_r = \frac{\rho_p {d_p}^2}{18\mu} \tag{2.13}$$

where d_p is the particle diameter and μ is the fluid viscosity. The term F_i in Eq. 2.12 indicates additional forces that may play an important role on the particles of the systems in exam. Notable examples are those due to the movement of the fluid surrounding the particle in motion, known as *virtual mass* forces, or the force caused by the pressure gradient in the fluid. For the system taken into exam, both aforementioned forces are negligible. However, an additional *Brownian* force is included, to take account of the random effect on the motion of the smallest particles. This force is expressed as:

$$F_{b_j,i} = m_p \zeta_j \sqrt{\frac{\pi S_0}{\Delta t}} \tag{2.14}$$

where ζ_j is a random zero-average, unitary variance Gaussan random number. The term S_0 is the intensity of the Brownian white-noise applied to the trajectory of the particle and is written as:

$$S_0 = \frac{216 \nu k_B T}{\pi^2 \rho {d_p}^5 \left(\frac{\rho_p}{\rho}\right)^2 C_c} \tag{2.15}$$

where ν is the cinematic viscosity, k_B is the Boltzmann constant, T is the system temperature, and C_c is the Cunningham correction to the Stokes' drag law for spherical objects and is written as:

$$C_c = 1 + \frac{2\lambda}{d_p}\left(1.257 + 0.4 \exp\left(-1.1 \frac{d_p}{2\lambda}\right)\right) \tag{2.16}$$

where λ is the molecular mean free path. In the case of the Lagrangian approach, the capture of particles is modelled using a *trapping* boundary condition. This means that when the trajectory of the zero-dimensional particle is calculated, if it goes through the walls surface, the trajectory is terminated and the fate of the particle is marked as *trapped*.

2.2.3 Particle Deposition and Filtration

For the design of process equipment for the filtration of solid particulate it is required to have a good estimate of the rate of deposition coefficient as well as the efficiency of deposition on the collector. To calculate these quantities, in analogy to what was done for the transport of momentum in section 2.1, the micro-scale concentration profiles of the transported particles must be interpreted according to macro-scale models. An important framework for the interpretation of such processes is given by the constitutive equation proposed by Yao et al. [1] in its seminal paper. This publication was originally proposed for filtration of solids and colloids in water through simple spherical granular beds systems, common in the field of water treatments and purification. It makes use of the fluid dynamic structure of flow past

a simple spherical collectors, first proposed by Levich [50], and later expanded for multiples collectors through the work of [51]. The original model was later improved and expanded by several authors in the field of filtration theory ([52–54]). According to this model, the expression for the particle deposition rate onto the solid wall of the porous medium can be written as:

$$k_d = \frac{3}{2}\frac{q}{D_g}\frac{1-\varepsilon}{\varepsilon}\alpha_D\eta_0, \tag{2.17}$$

where η_0 is the collection efficiency and α_D is the attachment efficiency. This latter parameter, that can assume values $0 \leq \alpha_D \leq 1$, is an indication of the balance between the attractive and repulsive forces acting on the particles approaching the solid collector. It is the result of the sum of viscous drag forces, hydrodynamic friction between the fluid and the wall, and London attraction forces ([50], [52], [55]). In this work it will be considered the case where chemical conditions are favorable to the perfect attachment of the particles and thus $\alpha_D = 1$. This deposition rate is equivalent to the reaction coefficient in the right-hand side of Eq. 2.11.

The collection efficiency η_0 of a single collecting element, otherwise known as single collector efficiency, is defined by Yao [1] as the ratio between the rate of collision of particles with the collector and the rate of particles flowing towards it:

$$\eta_0 = \frac{\text{rate of particles colliding the collector}}{qC_0\left(\frac{\pi {D_g}^2}{4}\right)}, \tag{2.18}$$

where the term C_0 indicate the inlet particle concentration, or the concentration at a long distance upstream the collector. The single collector efficiency is the sum of three deposition mechanism: Brownian diffusion, interception and sedimentation.

Fig. 2.1 shows a graphical representation of the three sedimentation mechanism, as proposed by Yao. The diffusion mechanism is the phenomenon which brings particles to settle on the collector, due to their random Brownian motion while transported by the fluid flow. This is the relevant mechanism for nano-particles up to 1 µm in size. The interception mechanism is the steric effect occuring when particles moving along the fluid streamlines get in contact with the collector at a certain distance depending on their finite dimension, where they stick to the surface of the solid. Finally, the sedimentation mechanism occur when a particle directly

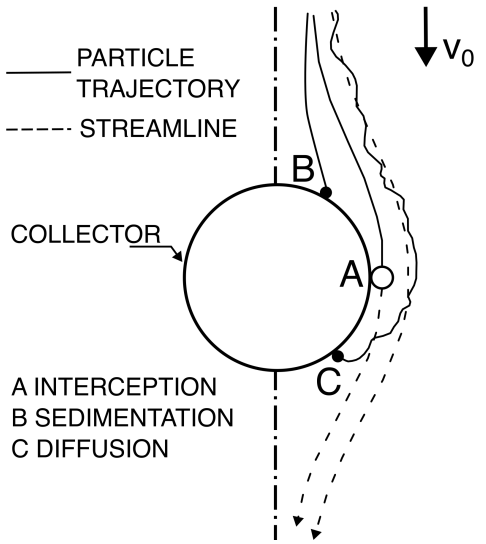

Fig. 2.1 A graphical representation of the three particle deposition mechanism as proposed by Yao [1]. The velocity V_0 is the upstream velocity at a long distance from the collector. The latter is represented by an isolated spherical grain on which particles impacts according to the different mechanisms. The present image is taken from [1].

impacts with the solid collector surface as it deviates by its transporting streamline direction, owing to additional inertial or gravitational forces. The latter is the leading deposition mechanism for bigger particles, with average particle size of at least 5 - 10 μm. A single collector efficiency can be written for each of the individual transport mechanisms reported above, namely η_B for the Brownian diffusion, η_I for interception and η_G for sedimentation. An analytical expression for these efficiencies is reported by Yao [1] in its seminal paper on particle deposition. This expression is not the only possible one and it should be considered valid only in the simplified condition for which it was developed, namely a single spherical collector immersed in an infinite fluid field in creeping flow. These expressions are:

$$\eta_B = 4.04 \mathrm{Pe}^{-\frac{2}{3}}, \tag{2.19}$$

$$\eta_I = \frac{3}{2}\left(\frac{d_p}{D_g}\right)^2, \tag{2.20}$$

$$\eta_G = \frac{(\rho_p - \rho)\, g {d_p}^2}{18 \mu q}, \tag{2.21}$$

$$\eta_0 = \eta_B + \eta_I + \eta_G, \tag{2.22}$$

where Pe is the Peclet number, namely the ratio between the advective and diffusive transport mechanisms. The ratio d_p/D_G is often referred to as $\mathrm{N_R}$. Eq. 2.22 report the total single collector efficiency of Eq. 2.18 as a function of the single individual mechanisms. It is worth noting that over the years different approaches has been used for the analytical expression of the collection efficiency, between which is import to mention the modification [52] to η_B using the coefficient proposed by Happel [56]:

$$\eta_B = 4\mathrm{As}^{\frac{1}{3}}\mathrm{Pe}^{-\frac{2}{3}}, \tag{2.23}$$

$$\eta_I = \frac{3}{2}\mathrm{As}{N_R}^2, \tag{2.24}$$

with the As coefficient being:

$$\mathrm{As} = \frac{2\left(1-{\gamma_H}^5\right)}{2-3\gamma_H+3{\gamma_H}^5-2{\gamma_H}^6}, \tag{2.25}$$

with the coefficient γ_H being a function of the porous medium porosity and its written as $\gamma_H = (1-\varepsilon)^{\frac{1}{3}}$. Another important mention is the work by Konstandopoulos and co-authors [57], which is based from the analysis made by Kuwabara [58], developed for an arrangement of cylinders instead of spheres, and introduces another porosity coefficient in the expression of the Brownian and interception efficiencies:

$$\eta_B = 3.5g(\varepsilon)\mathrm{Pe}^{-\frac{2}{3}}, \tag{2.26}$$

$$\eta_I = \frac{3}{2}\frac{{N_R}^2}{(1+N_R)^s}g(\varepsilon), \tag{2.27}$$

with the exponent $s = (3-2\varepsilon)/(3\varepsilon)$ and $g(\varepsilon)$ is the Kuwabara porosity function:

$$g(\varepsilon) = \left(\frac{\varepsilon}{2-\varepsilon-\frac{9}{5}(1-\varepsilon)^{\frac{1}{3}}-\frac{1}{5}(1-\varepsilon)^2}\right) \tag{2.28}$$

A global approach

A global approach to the problem of particle sedimentation can be used, taking into account Eq. 2.11, in steady-state conditions and considering only the macroscopic particle fluxes entering and exiting the control volume containing the porous media collector. Following this approach, Boccardo and co-authors [35] derived an expression for an effective particle deposition rate K_d, in the case of sole superficial reaction (again $k_b = 0$). This results in:

$$K_d = \frac{F_{tot}^{in}(c) - F_{tot}^{out}(c)}{|\Omega|\langle c \rangle}, \tag{2.29}$$

where the numerator represents the total effective flux of the scalar c through the system, $\langle c \rangle$ is the average scalar concentration and $|\Omega|$ is the total volume of the system. This expression is a valid substitute of Eq. 2.17 since it is easier to calculate the total particle flux across the system in exam. Moreover, since it depends on the total volume and the average particle concentration, it is scalable with different equipment sizes and dimension. Finally it is useful to introduce an *advective* Damköhler number Da, defined as:

$$\mathrm{Da} = \frac{K_d \cdot D_G}{q} \tag{2.30}$$

where K_d is the deposition rate previously defined, q is the superficial velocity and D_g the diameter of the mean grain or pore of the geometry in exam. This latter coefficient can be used in substitution of the single collector efficiency η_0 as an indication of the system deposition rate or in case of a superficial instantaneous reaction.

2.3 Generation of Open-Cell Foam Geometries

Different models can be used to represent the structure of an open-cell foams and several methods can be implemented to generate in-silico structures, with the help of some `Python` code and different software that will be mentioned in detail in the following sections. A foam can be represented by the ideal polyhedron devised by Lord Kelvin,the Kelvin's Cell, or the basic skeleton can be obtained by using the

diagram, composed of nodes and edges, produced by a random tessellation. The same basic skeleton can be used for the creation of geometries with different degree of description of the real foam solid surface: a *ball-and-sticks* model is similar to a foam but is not an exact reproduction of the real porous medium, since it lack a good description of the foam struts and nodes matter distribution.

Finally, a real geometry can be obtained by the processing of stack images obtained from exposing a foam sample to an X-ray tomography. This images, if properly treated, can be used to generate a three-dimensional model which is an approximation of the foam in exam but, at the same time, is the closest digital representation of a real foam. Before diving deep into these model, it is useful to mention the concept of Representative Elementary Volume (REV), which is, according to Whitaker [44], the smallest volumetric portion of a porous medium for which a certain property remain unchanged at increasing dimensions. Most commonly, a REV based upon the porosity ε is identified in the field of porous media, an this would be the one employed throughout this manuscript.

2.3.1 The Kelvin's Cell

This ideal approach to the modeling of solid foams, the Kelvin's Cell, was first proposed by Lord Kelvin as the shape taken by bubbles during the formation of liquid foams, being the configuration which attains the minimal surface tension. It consists of a *tetrakaidecahedron*, an ideal polyhedron, with 14 faces, 36 edges and periodic in space. The coordinate of its 24 vertices are all the possible combination of the numbers $\{0, \pm 1, \pm 2\}$ combined as coordinates in three-dimension. The *connectivity* between vertices is then easily obtainable. Given an edge of length a, the cell diameter is equal to $d_C = \sqrt{(2)}a$

Because of its periodicity the REV coincide with the cell itself. Its properties are also used as comparison in the analysis of random generated geometries, to assess how closely this structure resemble ideal shapes.

2.3.2 The Voronoi-like models

Modeling open-cell foams by means of ordered lattice is often not sufficient to catch some of the important properties, result of their embedded randomness, and therefore

other approaches were conceived in order to cope with the higher level of complexity. The creation of foam-like geometries is process involving several steps and touching different fields in computational geometry. Among these there is the use of random Voronoi tessellation which create cellular-like structures, subdividing the space into regions or *cells*. These structures have comparable randomness to that of real foams and can be used as a skeleton for the final model. The Voronoi Diagram is a well known type of random tessellation which, starting from an initial set of point, the *seeds*, subdivide space into convex polyhedra in such a way that the region around a seed consists of all the points closer to that seed than to any other. More rigorously, given a starting set of N random seeds $S = \{P_1, P_2, ..., P_n\} \subset \mathbb{R}^3$ and considering a generic point $\boldsymbol{x} \in \mathbb{R}^3$, being $d(\boldsymbol{x}, P_i)$ the Euclidean distance, a generic Voronoi region $\mathrm{R}(\boldsymbol{x}, P_i)$ is defined by

$$R(\boldsymbol{x}, P_i) = \{\boldsymbol{x} \in \mathbb{R}^3 \mid d(\mathbf{x}, P_i) < d(\mathbf{x}, P_j),\ j \neq i\} \tag{2.31}$$

Power Diagrams are another important type of cellular-like geometric graphs. They are a generalization of a Voronoi tessellation, introducing a weighing factor $w(P_i)$ to the initial seeds, as reported by Aurenhammer [59]. In particular, the Laguerre-Voronoi tessellation is a second order Power Diagram whose weighing factors are the square of the radii r_i of the spheres centered in the initial set of seeds $S = \{P_1, P_2, ..., P_n\} \subset \mathbb{R}^3$, resulting in Eq. (2.32):

$$R(\boldsymbol{x}, P_i) = \{\boldsymbol{x} \in \mathbb{R}^3 \mid d(\mathbf{x}, P_i) - r_i^2 \ < \ d(\mathbf{x}, P_j) - r_j^2,\ j \neq i\} \tag{2.32}$$

The use of a mono-disperse set of spheres combined with a Voronoi tessellation results in a structure with regular-shaped and homogeneous cells, closer to the ideal structure of the Kelvin's Cell. This kind of structure is attained whenever the foam creation process allows the structure to reach the *mechanical equilibrium*. However, most production processes result in foams with irregular-shaped and widely heterogeneous cells. The use of the Laguerre-Voronoi tessellation coupled with poly-disperse spheres packing, together with a wise choice of the cells volume distribution, can result in more realistic geometrical structures, able to better describe the phenomena occurring in such materials.

The tessellation algorithm

The computation of the tessellation is carried out using the `python` module `Tess` [60], which is a Python binding to the C++ code `voro++`, developed by Rycroft [2], a software library which carries out three-dimensional Voronoi and Laguerre-Voronoi tessellations. This code carries out cell-based calculations, storing all the outputs in the *class* `tess.Cell`, which contains information regarding vertices and centroids locations, facets connectivity and neighbour cells, to cite a few. The input parameters are the initial *seeds* coordinates and the *bounding box* coordinates; in the case of Laguerre-Voronoi diagrams the spheres radii acting as the tessellation algorithm weights. Additionally, the code can compute a periodic or non-periodic diagram, by enabling or disabling a Boolean parameter. The output is in the form of a list of instances of the `Cell` class, each corresponding to the convex polyhedron computed starting from the initial sphere packing. An additional feature to compute and list each edge by its vertices was added, both for singular cells and the global structure, inspired by the code developed by Gostick [61]. Finally, a list of all the edges is computed (purged of all the duplicates) containing the arrays of the coordinates of each pair of vertices defining an edge. Then, this list can be safely passed as input to the next step of the workflow which generates the geometry file.

2.3.3 The starting seeds generation

The random points to be used as starting *seeds* for the Voronoi-like tessellations can be created with different methods. A classical approach is to use a sphere packing process, which simulate the settling of a group of N_{tot}^{sph} spherical objects being poured inside a rigid container. The results of this type of simulations, following the Discrete Element Method (DEM), is a randomly closed pack of spheres, whose main drawback is the high computational cost, because all the interactions/collisions between sphere-sphere and sphere-container must be calculated. This method works well with both mono or poly-disperse population of spheres. An alternative and innovative method is the use of an aggregation algorithm, which uses a stochastic process to position the spherical objects inside the computational domain. This method has a very low computational cost, if the sphere size is mono-disperse. However, the heterogeneity of the sphere spacial location is achieved varying the

total compactness of the aggregate inside the containing box. The principle governing each of these methods will be reported in the following sections.

The Sphere Packing Process

The creation of a mono-disperse or a poly-disperse hard-sphere packing is carried out using the open-source code `BSand`, first proposed by Boccardo and co-authors [34]. It uses the computer graphics code `Blender` which solves the Newton's equation of motion for each of the N input objects. The dynamics of collisions of a system of N rigid-body spheres is solved by means of the Bullet Physics Library (BPL). This collection of codes provides several iterative algorithms to simulate the packing process of a large number of elements in a robust and accurate way, in a relatively low computational time. The geometrical input parameters to be set are: the container shape, its size, and the hard-spheres size distribution main parameters. For the generation of the random sphere packings of Chapter 3 of this manuscript, the grain size distribution chosen is Gaussian. A random variable X is normally distributed when its associated probability density function is:

$$f_X(x) = \frac{1}{\sigma_S\sqrt{2\pi}} \exp\left(-\frac{1}{2}\frac{(x-\mu_S)^2}{\sigma_S^2}\right) \tag{2.33}$$

$$CV(x) = \frac{\sigma_S}{\mu_S} \tag{2.34}$$

where μ_S and σ_S are respectively the mean value and the standard deviation of the random variable. For such distribution one can define the coefficient of variation $CV(x)$, reported in Eq. (2.34), the ratio between the standard deviation and the mean value of the distribution. Such coefficient, together with the mean sphere diameter μ_S are the input parameters provided to `Blender`, by means of `python` code, to compute the sphere packing. Finally, the locations and dimensions of each sphere inside the container are retrieved.

The Sphere Aggregation Process

For the present work a novel method for the generation of the starting *seeds* is introduced. This innovative procedure is based on the a aggregation model developed by Moreaud and co-authors [62], in which spherical objects are sequentially inserted in the domain following a stochastic process. The fractal dimension of the aggregate is tuned by means of two compactness parameters, namely α and β. In this aggregation process objects can be either in contact or at a pre-defined repulsion distance $Repul$. The location of already positioned objects is used to calculate the positions of the ones that follow, taking into account potential concave locations in the aggregate. Thus, the probability that the next sphere will be positioned in a concave zone is α, whereas the probability that a concave zone is closer to the center of mass is governed by β. Despite the fact that the radius of the spheres population is kept constant, the virtually infinite amount of combinations between α, β, and $Repul$ leads to multiples different realizations of a stochastic process - each one with different degree of heterogeneity - that can be used as seed for a random tessellation, similar to what can be achieved using poly-disperse spheres populations. Most importantly, this requires very low computational cost, since this model is purely geometrical, based on spheres of constant radius on a discrete grid, and does not require a sedimentation simulation.

2.3.4 Digital reconstruction from x-ray tomography

A tomography image of a foam sample can obtained using the x-ray technique. This results in a three-dimensional stack of grey-scale images, in TIFF format, representing cutting planes of the sample along the depth coordinate. The amount of voxels, i.e. three-dimensional pixels, for each x-y plane and the amount of planes in the z-direction depend on the voxel resolution of the measurement device. A three-dimensional reconstruction of the sampled foam can be obtained from the TIFF image, by application of a segmentation algorithm which provide a threshold value within the grey-scale voxel distribution, allowing the determination of the void and the solid phases, resulting in a binary the stack image. Afterwards, a contouring algorithm can be used to obtain the solid surface of the foam sample, in a format that can be eventually used by a meshing software for the creation of a computational domain. The threshold selection method used for all the sample used

throughou this work is the one developed by Otsu [63] which, given the initial image grey-scale color distribution histogram, returns a threshold value which separates the pixels/voxels of an image into two classes, background and foreground. In the case of x-ray tomographies this represents the void and solid phases. Once a binary image is obtained the solid surface of the foam sample can be reconstructed using the well known *Marching cubes* algorithm [64], which creates a triangulated iso-surface representing an approximation of the original real surface, that can be exported in the commonly used `.stl` file format.

2.3.5 Morphological operations on binary three-dimensional volumes

The solid geometry representing an open-cell foam can be defined within a binary framework. The latter is charactrized by a three-dimensional structured grid divided into cells, called voxels, that can assume a binary value, namely 1 or 0, which usually refer respectively to the solid or void fraction. This type or representation is in toto similar to the geometry obtainable from tomography images, once the segmentation algorithm is applied, as reported in section 2.3.4. Thus, an open-cell foam is represented by a subset of the overall volume, and its geometry can be modified using specific functions defined by morphological theory.

Morphological operations are functions commonly used in the domain of binary images processing, that transform the starting object according to the four basic operators, i.e. *Erosion*, *Dilation*, *Opening* and *Closing*. These operators works on sets in space. First the working set of points is introduced as $X = \{z \in \mathbb{R}^3\}$, with its complementary $X^c = \{z \in \mathbb{R}^3, z \notin X\}$ and its position, denoted as the position of one of its points in $\mathbb{R}^3$. Then, the following additional set can be defined: $X_z = \{x+z; x \in X\}$ is the set translated at point z, and $\check{X} = \{-x, x \in X\}$ is the transposed set of X. The dilation operator of a set Y by X is denoted as $\delta_X(Y)$ and the erosion as $\varepsilon_X(Y)$. These are reported in Eq.2.35 and Eq. 2.36, as defined by Serra [65]:

$$\delta_X(Y) = \{z : \check{X}_z \cap Y \neq \emptyset\} \tag{2.35}$$

$$\varepsilon_X(Y) = \cap\{Y_z, z \in \check{X}_z\}. \tag{2.36}$$

Dilation is the locus of the possible z positions of the $\check{X}_z$ transposed element when the latter intersect Y, whereas erosion is the location of the possible z positions of the X_z element when it is contained in Y, as reported by Moreaud et al. [62]. The closing operator $\phi = \varepsilon(\delta(Y))$ is defined as the combination of a dilation followed by an erosion operator of the set Y by X. Analogously, the opening operator $\gamma = \delta(\varepsilon(Y))$ is the combination of an erosion, followed by a dilation operation of the set Y by X. Thus, given a structuring element of arbitrary shape, most commonly a voxelized cube, sphere or cross of given dimension, it is possible to modify the starting geometry. In particular, the closing operation creates "bridges" across the binary volume, which are essential in transforming a foam *skeleton*, into a morphologically realistic foam geometry.

Chapter 3

A Simplified Approach To Open-cell Foams Modelling

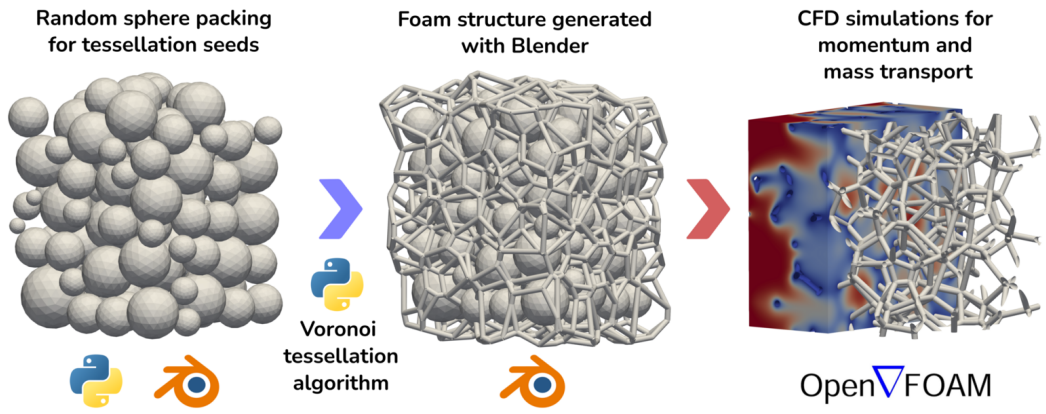

Fig. 3.1 A graphical representation of the workflow proposed in the present chapter.

As already mentioned in the Introduction of this manuscript (§1.3.1 and §1.3.2), many authors in literature developed method to reproduce open-cell foam geometries using computational methods. Most of the aforementioned software can produce good results, however, to the best of the authors' knowledge, there is no example in literature of any open-source tools which fit in a unique platform the geometry generation and the transport simulation workflow, for the modeling of this kind of foams. Therefore, the work detailed in this chapter is to introduce, test and validate an open and flexible *in-silico* tool, that is able to reproduce a great variety of structures, exploring large parameter ranges, in order to be able to optimize the

geometric structure according to the different application areas. Fig. 3.1 is a graphical abstract of the work presented in this chapter, that has been published in form of peer-reviewed article [3].

This tool rely only on the open-source computer graphics code `Blender` and on `Python` programming language code to calculate and create the final geometry. The initial set of random points are generated by a random sphere packing (either mono- or poly-dispersed), following an already validated workflow proposed by Boccardo et al. [34]. The position of the edges and nodes of the tessellation, generated from the starting random seeds, is retrieved from the Voronoi algorithm. Then `Blender` creates cylinders and sphere at the supplied coordinates to generate the foam structure. The resulting geometry will be used to define a computational domain in which to run CFD simulations in the `OpenFOAM` environment. First, the flow field is solved, to estimate the pressure drop and hydraulic permeability of the generated geometries. Then, micro-scale mass transfer simulations are carried out to explore transport and surface reaction through these porous media. This problem is of great importance in chemical and environmental engineering, and as such it has been investigated by many authors dealing with a variety of applications, such as particle deposition in filtration [1], catalytic processes through filter beds in the automotive industry [66], aquifers remediation [67], to cite a few.

This work will focus on phenomena of fast deposition/reaction of colloidal particles on the solid surface. This circumstance usually occurs either in the event of clean-bed filtration [1] or in case of a very fast catalytic reaction, whose coefficient of reaction tends to infinity. In this particular cases deposition is driven by Brownian motion and steric interception mechanisms. Following the model and methodology proposed by Boccardo and co-authors [32, 35], and then used in subsequent works by Marcato et al. [68] and Crevacore et al. [69], the results of the scalar transport simulations will be used to calculate an effective macroscopic particle deposition rate coefficient K_d, which would be used to estimate the efficiency of clean-bed filtration of open-cell foams.

3.1 Test cases and numerical details

The current section will describe the different test cases explored for this work, along with the operating conditions and numerical details of the simulations. The

generation of the geometry will be described first, then the meshing strategy, and finally the simulations setup. All the technical information regarding hardware and computational times are reported in the Supporting information available in Appendix A.

3.1.1 Geometry model generation

The geometry creation is carried out by the open-source software `Blender`, which takes as input the edges coordinates previously computed by `Python` code using the Voronoi and Voronoi-Laguerre algorithm. The output is a `.stl` file which is then ready to be meshed and used as input for the CFD code. The geometrical model explored for this work are of two types: the Kelvin's Cell simplified model (a truncated octahedron), and structures originated from random tessellation, in particular Voronoi and Laguerre-Voronoi tessellation. For each type of geometry four values of *pore per inch* (PPI) have been considered, namely PPI $= \{10, 20, 30, 45\}$, and five values of porosity ε, namely $\varepsilon = \{0.77, 0.79, 0.85, 0.89, 0.95\}$, for a total of 20 cases.

The Kelvin's Cell geometry creation is straightforward, since all vertices positions are permutations of $(0, \pm\sqrt{2}/2, \pm\sqrt{2})$, resulting in a tetrakaidecahedron with edge length equal to 1. The connectivity between nodes is simply obtained from observing the figure and the edges are calculated as the vectors linking vertices. In the case of foams generated by random tessellation, the geometry aims instead to represent a small cubic portion belonging to the bulk of the real structure. First the random sphere packing is generated using the code `Bsand`, as reported in the previous section. In order to assure independence from any wall effects due to the container, a very large packing is generated with up to 6000 grains packed inside a cubic container with side dimension equal to 15 times the average grain diameter μ_S. This procedure, despite computationally burdensome, ensures random disposition of the spheres in the bulk part of the packing, whose resulting distance from the container walls is around 4 to 5 times mean grain diameters, as reported in [34] and also ensure that the most inner part, which is the one from which the random seed are extracted, has dimension at least equivalent to five mean grain diameter. More details regarding the dimension of this part is given in Section 3.2.1 where the REV grid independence study is described.

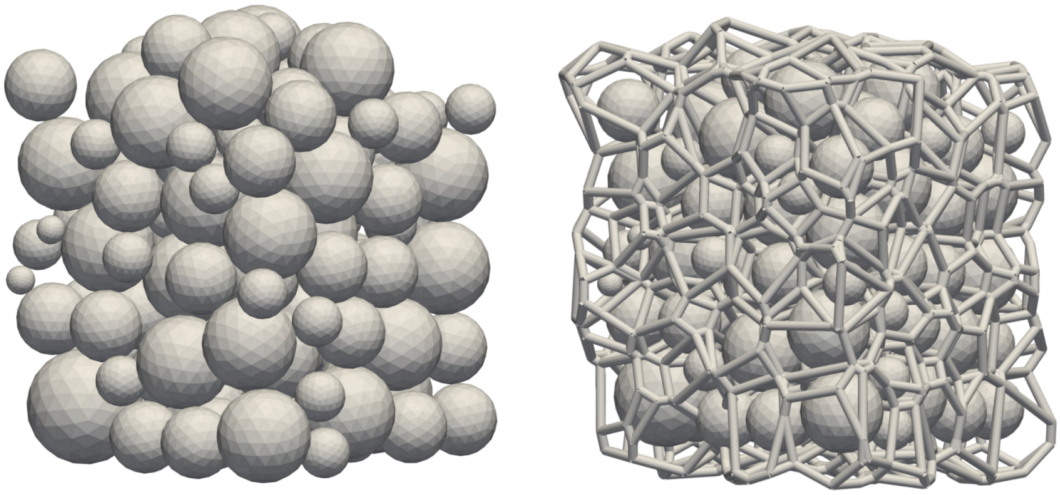

(a) Packed spheres (b) Resulting foam

Fig. 3.2 Example of the two main steps in the creation of a foam REV. In (a) it is reported the original random sphere packing. In (b) the resulting open-cell foam, obtained with a periodic Laguerre-Voronoi algorithm, is reported overlapped to its generating sphere packing. Larger spheres have a larger area of influence, hence their resulting "cells" are much larger.

In the case of mono-disperse sphere packings, the grains are constituted by spheres with unitary diameter. In the case of poly-disperse packing, two different instances have been generated with same mean sphere volume $E(V)$, which is equal to the volume of sphere with unitary diameter, and two values of the coefficient of variation $CV(V)$, namely 0.2 and 0.35. Once the packings are generated, the coordinates and dimensions of the spheres are used to calculate the tessellation over a small cubic portion at the core of the volume. The two steps of this procedure are visualized in Fig. 3.2.

The dimension of this portion and its choice would be discussed in details in the next Section. The output of the code is a collection of all the cell edges and nodes, in the form of point coordinates in space. The information regarding nodes and edges position and orientation are passed to `Blender`, via a `Python` script, which places cylinders and spheres in to reproduce struts and vertices. In order to achieve the chosen pore density (PPI), the geometry file is scaled down, either using `Blender` or `OpenFOAM`, by a factor calculated as follow:

$$f_{scale} = \frac{\left(\frac{0.0254}{PPI}\right)}{D_{tess,mean}} \tag{3.1}$$

where the numerator is the pore size (in meters) of a foam having a certain PPI and the denominator is the mean cell size of the tessellation, calculated as the diameter of sphere having the same volume as the average cell. The strut diameter is chosen so as to reach the desired foam porosity, which is calculated from the computational volume mesh generated by `OpenFOAM`. By a trial-and-error procedure, a correlation between the strut dimension and the porosity ε has been derived.

3.1.2 Mesh generation

Once the foam geometry is generated it is exported in *.stl* format. An *.stl* file describe a solid volume by means of its surface, which is discretized by a triangulated mesh. This type of file formatting, being supported by a wide range of CAD/CAE software, is very common and portable. It is also the format of choice to define geometries to be meshed in `OpenFOAM`. The geometry exported from `Blender` represents the solid fraction of the domain, whereas the void/fluid fraction in-between is the part to be meshed by `OpenFOAM`. The meshing procedure is carried out in two main steps: first a *background* structured hexahedral mesh is generated by the `OpenFOAM` utility `blockMesh`. This hexahedral mesh is used as a starting point to build a *body-fitted* grid generated bythe utility `snappyHexMesh`, also part of the `OpenFOAM` suite. The computational grids created in this manner are predominantly constituted by hexahedral cells, ensuring good numerical performance for the solver, and are then subsequently refined close to the solid walls, resulting in cells of increasing dimension moving farther away from the walls, towards the bulk of the fluid. This allows to have a large number of small cells in the areas where gradients are higher, whereas in the bulk of the fluid, where stresses are lower, the cell density is lower, thus reducing the total computational cost. The mesh generation process and the choice of optimal parameters are crucial steps in order to obtain a grid independent solution and an accurate representation of the original geometry. The strategy to achieve an accurate computational grid is to compromise between small initial background cells dimension, the refinement level and the amount of cells in each refinement layer. This is particularly true for geometrical structures such as open-cell foams, which have a void fraction ranging from 70% to well beyond 90%, meaning that a very large amount of cell is required to properly describe the fluid motion within the foam pores. In order to achieve solution grid independence, the mesh was progressively refined, both by decreasing the background cell dimension and

increasing the refinement level on the solid surface. The comparison between the different meshes is carried out by confronting the values of porosity obtained as well as the solution of the flow field. For this work it has been determined that the optimal number of background cells per pore diameter of around 22, the best refinement level value is $R = 2$, with 4 consecutive layers of refined cells from the solid surface. The details of the grid independence work would be shown in the next section.

3.1.3 Fluid flow simulations

As previously mentioned, the numerical simulations were carried out using the open-source CFD code `OpenFOAM 7`. The computational domain used in all the simulations carried out for this work has cubic shape with side L, with the origin of the axis at its center, with the diagonal vertices respectively $x_{min}, y_{min}, z_{min} = -L/2$ and $x_{max}, y_{max}, z_{max} = L/2$. The flow field is initialized by setting a fixed pressure difference $\Delta P/\rho$ in x-normal direction between the inlet and the outlet patches of the domain, which are x-normal surfaces with coordinates respectively $x_{inlet} = -L/2$ and $x_{outlet} = L/2$. The value of L is equal to the linear dimension of the REV (defined as a cubic volume), which in the case of the Kelvin Cell coincide with the cell itself, whereas for the random foam was determined with a study which is thoroughly explained in the next section. This allows to have a fully developed flow field inside a small computational domain; although in this set-up there is no a-priori knowledge of the characteristic velocity of the system (and thus of the Reynolds number), it can be estimated using equation (2.5). A *no-slip* condition for the velocity U is applied at the solid surface of the foam, a condition of zero gradient at the outlet patch, whereas at the remaining sides of the domain a *symmetry* boundary conditions is applied, implying no fluid motion across those. The Newtonian incompressible fluid here considered is water, with density ρ = 997.78 kg m^{-3}, kinematic viscosity μ = 9.77×10^{-4} kg m^{-1}s^{-1}. The system is solved using the solver `simpleFoam`, at a constant temperature $T = 293K$ (the energy equation was not solved) in steady-state condition, under laminar flow regime ($1 \cdot 10^{-4} < \mathrm{Re} < 1 \cdot 10^{-3}$). The Reynolds number for this work is defined as $\mathrm{Re} = U \cdot D_{pore}/\nu$, with D_{pore} being the mean pore diameter of the foam, defined as the diameter of a sphere having the same volume as the mean pore.

3.1.4 Scalar transport simulations

The results of the momentum transport simulations have been used for the mass transfer simulations solving Eq. (2.9), using the same mesh. Five different operating conditions, for each combination of pore density and porosity, have been explored, changing the Pe number, namely $\mathrm{Pe} = \left\{5, 5\sqrt{10}, 50, 50\sqrt{10}, 500\right\}$, which was used to estimate the value of the diffusivity $\mathscr{D}$ from:

$$\mathscr{D} = \frac{UD_{pore}}{\mathrm{Pe}} \tag{3.2}$$

The system is solved at constant temperature, in steady-state condition using the solver `scalarTransportFoam`. The colloidal particles are represented by a scalar, acting as the normalized concentration, with an inlet value C_0 set equal to 1, a condition of zero gradientat the outlet patch and at the remaining sides of the domain a *symmetry* boundary condition is applied. On the solid walls a Dirichlet boundary condition, with a normalized concentration with a fixed value C_{walls} equal to 0, was imposed. The effective deposition rate coefficient K_d is estimated by the solver from the fluxes on the solid surfaces, using Eq. (2.29).

3.2 Results and discussion

3.2.1 Grid independence study

The meshing procedure used during all the simulation campaign was presented in section 3.1.2. The first goal of this study was to determine the optimal meshing strategy by tuning two parameters: the number of the starting `blockMesh` background cells and the level of refinement R performed by `snappyHexMesh` on the cells close to the solid surface.

In order to reduce the computational cost of such investigation, it was chosen to perform these simulations on the simplified Kelvin's Cell model, which is a single-pore periodic geometry. The values of the subdivision of the initial bounding box considered were $C_{background} = \{10, 12, 15, 17, 20, 25, 30, 35, 45, 55, 75, 85\}$ and the values of the refinement level taken into account were $R = \{0, 1, 2\}$. The grid independence study, whose results are reported in Fig. 3.3 show the calculated value for

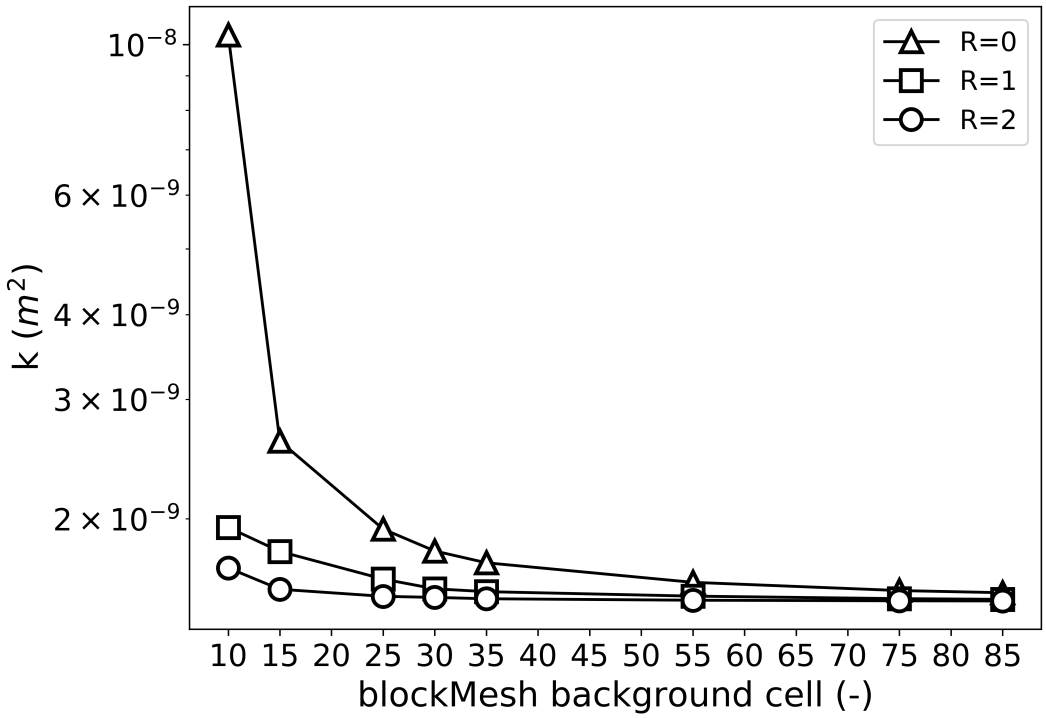

Fig. 3.3 Values of calculated permeability with increasing overall mesh refinements expressed as number of background cells per equivalent pore diameter. Curves with different lines represent three different levels of mesh refinement close to the foam walls (R=0 means no refinement, R=2 means two subsequent refinements).

the permeability k as a function of the `blockMesh` background cells number. For values of the refinement parameter $R > 1$ and for more than 25 background cells/pore the permeability reaches an asymptotic value. The best performance overall is achieved with R=2 because of the inferior wall-clock time for the solution to converge, indicating that a good trade off between accuracy and computational time could be achieved, with a number of subdivision ranging of 22. An additional grid independence investigation at different porosity values, $\varepsilon = \{0.77, 0.79, 0.85, 0.89, 0.95\}$ and $R = 2$, was carried out to ensure that the accuracy of the solution, previously calculated, remained in the same range of error varying the porosity. Fig. 3.4, reporting the relative error with respect to the asymptotic value of the permeability, $e_r = |k_{as} - k|/k_{as}$, illustrate how the error lies below 2% except for the highest value of porosity ($\varepsilon = 95\%$), where it slightly depart from the other curves.

The results previously obtained were used to tune the meshing procedure for the randomly generated geometries. In particular, the aim was to determine the

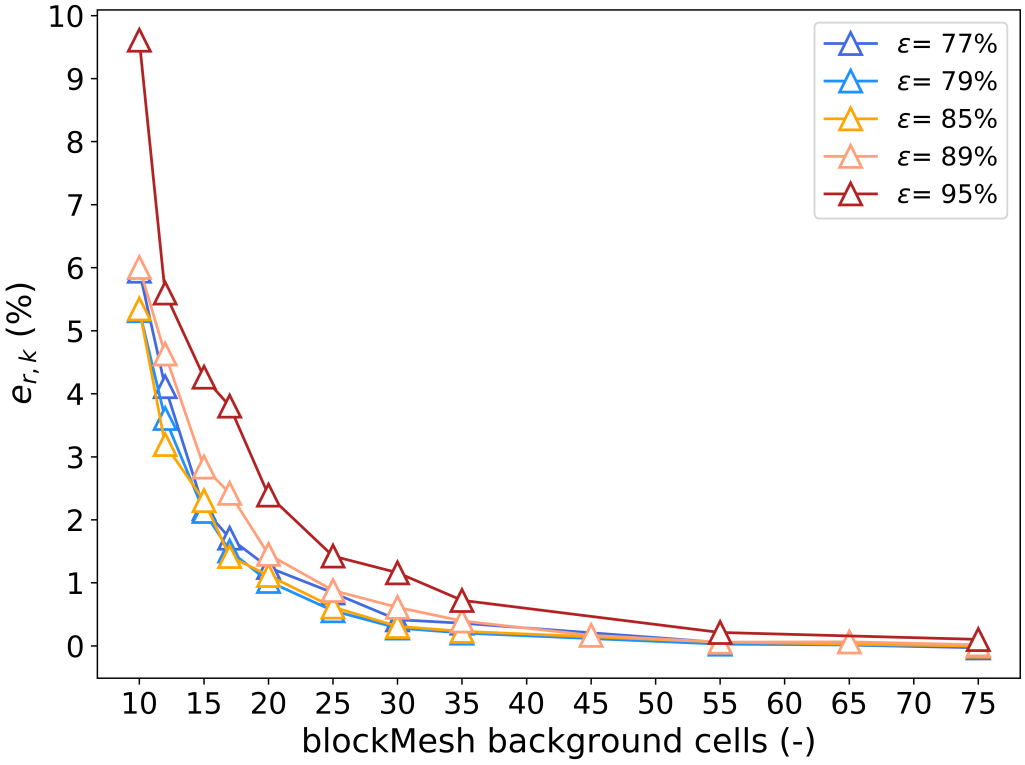

Fig. 3.4 The relative error of the permeability e_r, for increasing overall mesh refinements, again expressed as number of background cells per equivalent pore diameter. Curves with different colors represent five different values of porosity $\varepsilon = \{77, 79, 85, 89, 95\}$

dimensions of the *Representative Elementary Volume* (REV), in terms of the number of foam pores contained. Flow field simulations were run on increasingly larger cubic portion of the same *monodisperse* foam, with sides respectively equal to the length of 2, 3, 4 and 5 pore diameters. The values of porosity ε, superficial porosity ε_s and permeability k were considered in order to determine the optimal size of the computational domain. Following the meshing strategy exposed above, to generate the computational grid were used 20 mesh-cells per pore and R = 2, while the simulations were run at Re $= 1e-03$, in steady-state condition.

The results are reported in Tab. 3.1. Considering the rapidly increasing computational costs and the small incremental geometrical differences between the two bigger computational domains, the choice was made to consider a cubic foam portion whose side equals four equivalent pore diameters to be a representative elementary volume for the cases considered in this work.

Pores/side	ε	ε_s	k (m^2)	$e_{r,k}$ $(\%)$	Mesh Cells
2	0.900	0.878	3.24×10^{-9}	3.73	8.7×10^5
3	0.908	0.903	3.53×10^{-9}	5.01	2.8×10^6
4	0.902	0.917	3.32×10^{-9}	1.26	6.7×10^6
5	0.905	0.893	3.36×10^{-9}	0.00	1.3×10^7

Table 3.1 The results of computational domain dimension study carried out increasing progressively the dimensions of the computational domain. Along with the number of mesh cells, the table reports the calculated values for the porosity ε, the superficial porosity ε_s, permeability k and the error $e_{r,k}$ with respect to the most accurate case (5 pores/side)

Finally, a grid independence study was also carried out for the scalar transport cases. The value used to compare the results was the scalar total flux, defined as $F_{tot} = F_{tot}^{in} - F_{tot}^{out}$. These simulations were run, again, on the Kelvin's Cell geometry, considering the same range of subdivision $C_{background}$ as previously mentioned, with a refinement level R = 2. The operating condition used were $\mathrm{Re} = 1e-03$, $\mathrm{Pe} = 50$, in steady-state conditions. The simulations were carried out for a high value of porosity, $\varepsilon = 0.89$,in order to account for effects on the colloidal deposition due to the great void fraction of the system. The plot in Fig. 3.5 show the error relative to the asymptotic value, $e_{r,F} = |F_{tot}^{as} - F_{tot}|/F_{tot}^{as}$, as parameter for comparison between the different meshes, in analogy to the momentum transport study.

The results showed that 20 cells per pore were an adequate trade off to describe scalar transport phenomena, with an error with respect to the asymptotic value $e_r \approx 1\%$. Therefore, for grid independent simulations on a computational domain representing a REV for the considered foams, this would results in meshes size of approximately eight to nine million cells.

3.2.2 Numerical analysis

An example of the flow field simulations is reported in Fig. 3.6 for the case of 30 PPI and porosity ε = 85%. The results for the permeability k, reported in Fig. 3.8, confirm the fact that the higher the porosity, the higher the permeability, which instead decreases rapidly with increasing PPI. Moreover the histogram show how the poly-disperse cases systematically present a higher permeability with respect to more ideal cases such as Kelvin's Cell or mono-disperse foams.

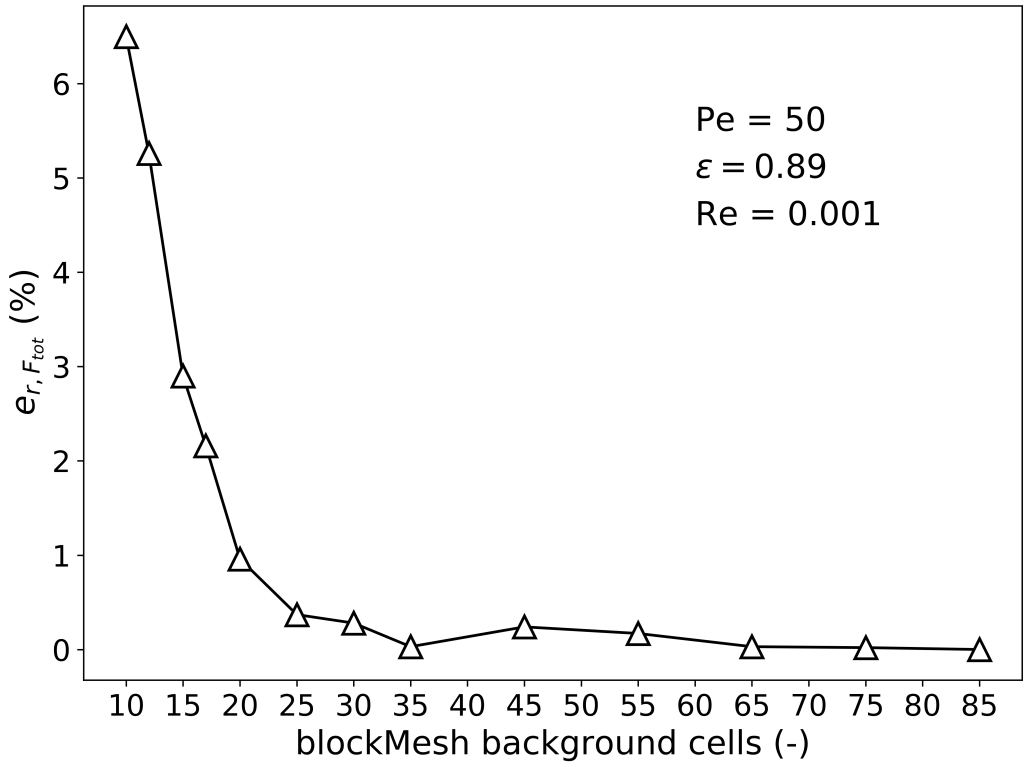

Fig. 3.5 The relative error of the total flux F_{tot}, e_r, for increasing overall mesh refinements.

A global overview of the simulations and geometry is illustrated in Fig. 3.7 where there are reported and example of `scalartTransportFoam` solution together with foam solid structure.

From the scalar transport simulations a macroscopic measure of the filtration efficiency can be obtained. An example of the solution of the simulations is reported in the contour plot of Fig. 3.9 for the case of 30 PPI and porosity $\varepsilon = 85\%$. Fig. 3.10 shows the relationship between the advective Damköhler number Da, defined in Eq. (2.30), as a function of the Péclet number.

In particular, Da number is reported for the all values of PPI (10, 20, 30, 45) as well as for different geometrical models. However, it can be noticed that keeping constant the Pe value and the geometry model, the Da values for different PPI collapse to the same point. This comes from the fact that the Damköhler number normalizes the deposition rate with respect to the dimension of the computational domain and that in laminar regime these cases are proportionally scaled. Globally, at increasing Pe number, the quantity of colloids impacting on the solid surface

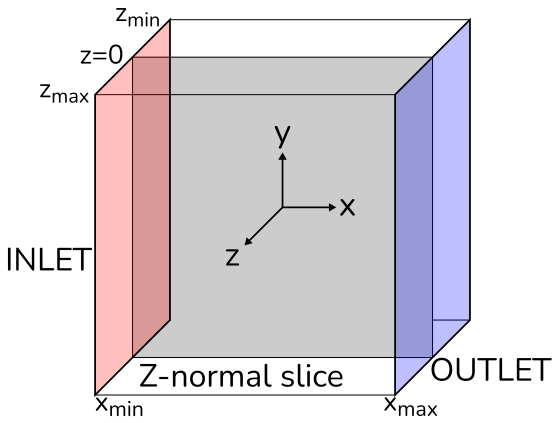

(a) z-normal slicing plane location

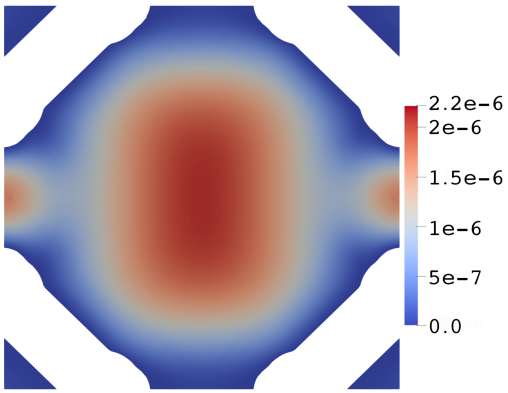

(b) KC

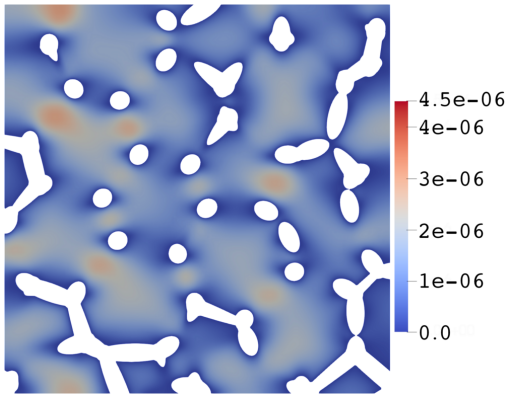

(c) MONO

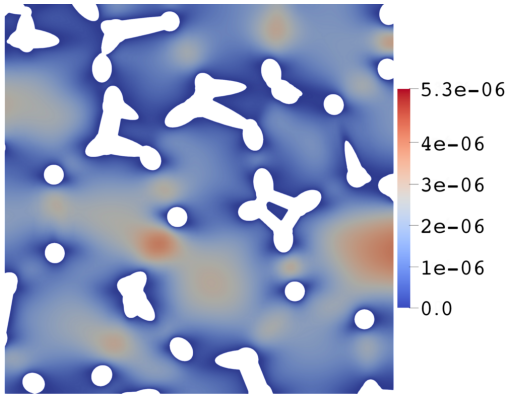

(d) CV = 0.2

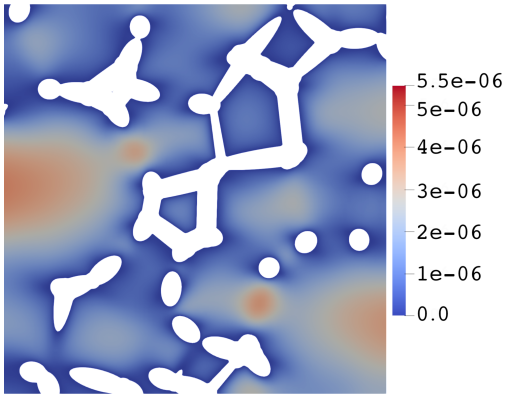

(e) CV = 0.35

Fig. 3.6 Contour plots of the velocity magnitude U (m/s) for the four different geometrical models (30 PPI and ε = 85%). In (a) an exemplification of the computational domain is reported in order to show the location of the z-normal slicing plane (at coordinate z = 0) used to extract the following contours: (b) Kelvin's Cell, (c) mono-disperse Voronoi, (d) poly-disperse Voronoi-Laguerre with CV = 0.2, (e) poly-disperse Voronoi-Laguerre with CV = 0.35

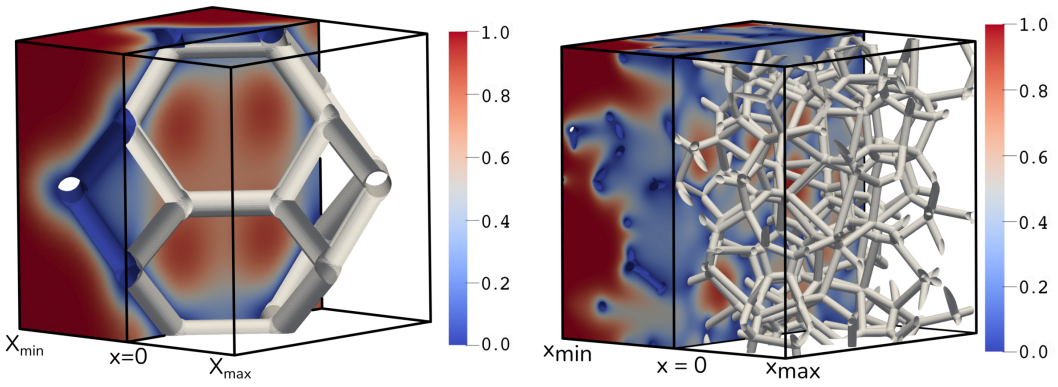

(a) KC (b) Voronoi-Laguerre

Fig. 3.7 Contour plots of normalized concentration C for foams with 30 PPI and $\varepsilon = 95\%$: (a) Kelvin's Cell, (b) poly-disperse Voronoi-Laguerre with CV = 0.35. The slicing plane is at x = 0

of the foam decreases following a power law, which was expected to some extent, considering the results of previous studies [1] on Brownian clean-bed filtration. At Pe > 100, the difference between the different geometrical models is very small. This comes from the fact that the corresponding colloidal particle size is closer to the micrometer and and the molecular diffusion coefficient becomes very small. At lower Pe number the difference between the four different model is not negligible and it should be investigated further. A new coefficient, $C_{KC} = \mathrm{Da}_{KC}/\mathrm{Da}_{VOR}$, the ratio between the Damköhler number obtained from the Kelvin's cell model and the ones derived from Voronoi tessellations, was introduced to more easily explore the effect of foam randomness specifically and also investigate the relationship with macro-scale parameters such as porosity ε, specific surface S_V and tortuosity τ. The latter defined as in Eq. (3.3):

$$\tau = \frac{\int |\mathbf{U}| d\mathbf{x}}{\int U_x d\mathbf{x}} \tag{3.3}$$

where $\mathbf{U}$ is the local velocity vector and U_x is the local velocity component along the main flow direction ([70, 71]). The values of τ are reported in Fig. 3.13, which show how for such materials with very high void fraction and for the operating condition chosen, i.e. very low values of Re, the tortuosity depart slightly from unity.

A first approach was to try to interpret C_{KC} (which, for clarity, we remind the reader, it describes a particle deposition efficiency by means of a Damköler number)

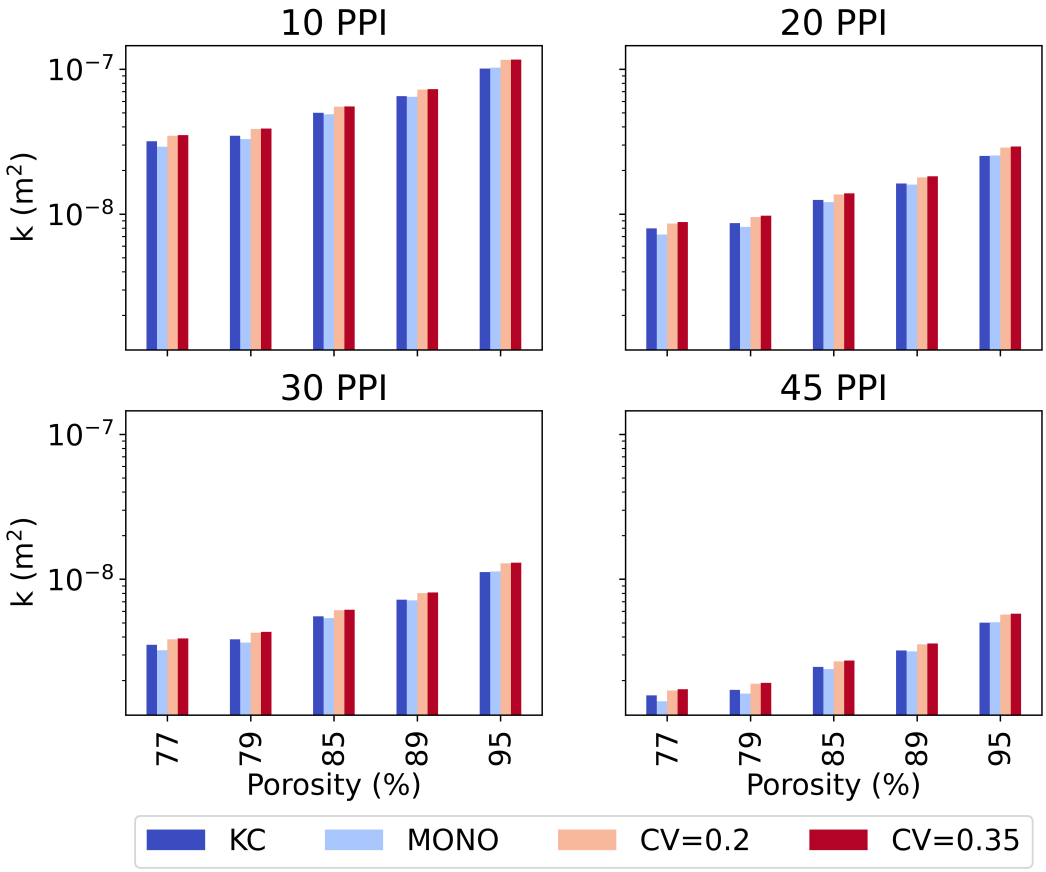

Fig. 3.8 Permeability k vs. porosity, with each subplot representing the results for the four different values of PPI. Different colors represent a different geometry: Kelvin's Cell, mono-disperse Voronoi and poly-disperse Voronoi-Laguerre foams with different coefficient of variation. For an effective interpretation of this bar plot, the reader is advised to refer to the color version of this paper available online

according to well known constitutive equations as function of the porosity, developed for fluid motion across solid obstacles, namely Happel [56] for spherical collectors and Kuwabara [58] for cylindrical collectors [1]. The results of C_{KC}, as a function of Pe number, were normalized by the values of the cited functions, which depend on porosity. The results were then fitted according to a power law, in the form $f(\varepsilon, \mathrm{Pe}) = a \cdot \mathrm{Pe}^b$. This was done to ascertain if these sole available relationships, which are capable of exactly predicting the impact of porosity on particle deposition

[1] The two cited seminal papers, together with [50] mainly explored the fluid dynamic structure of flow past different arrangements of collectors. For the reader specifically interested in the evolution of different approaches in obtaining constitutive equations for particle deposition efficiency by implementing different simplified geometrical models, we point out to (among others): the already cited [1], then [52], [53], [54], [72], and [35]

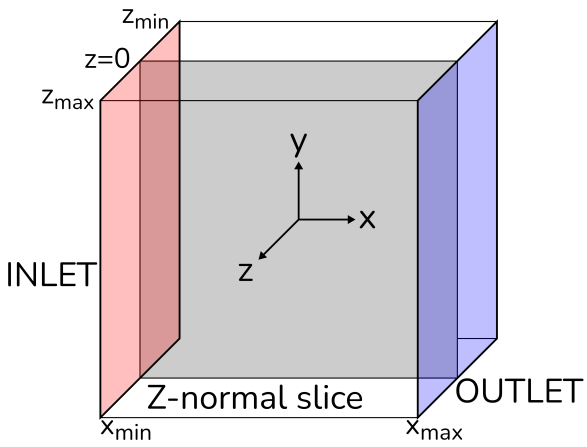

(a) z-normal slicing plane location

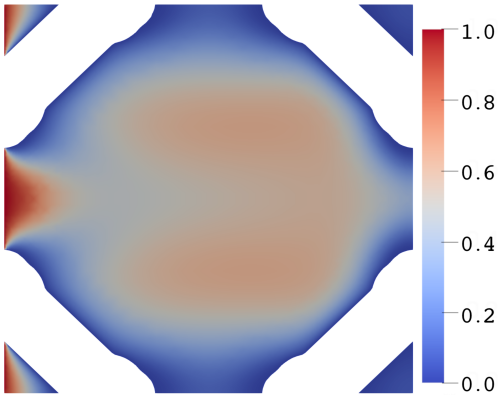

(b) KC

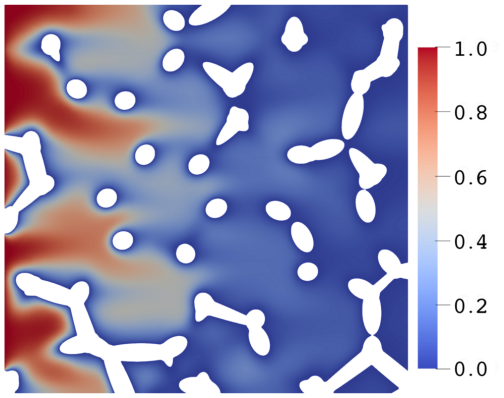

(c) MONO

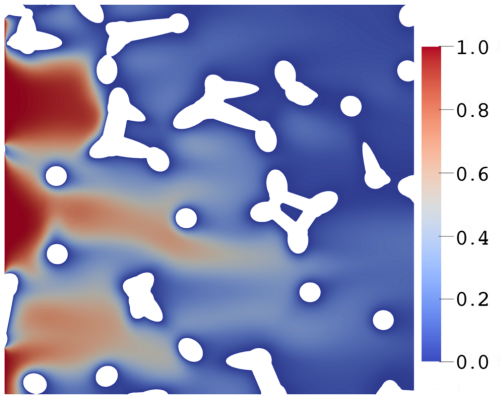

(d) CV = 0.2

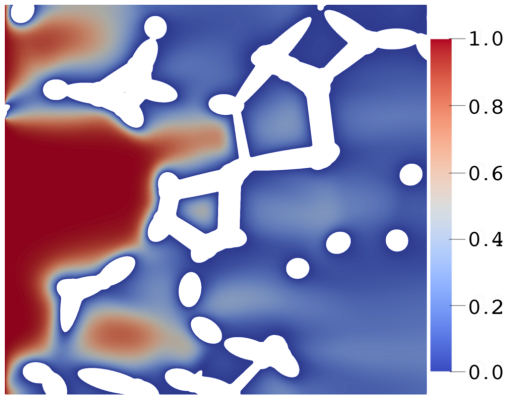

(e) CV = 0.35

Fig. 3.9 Contour plots of the normalized concentration C for the four different geometrical models (30 PPI and ε = 85%) In (a) an exemplification of the computational domain is reported in order to show the location of the z-normal slicing plane (at coordinate z = 0) used to extract the following contours: (b) Kelvin's Cell, (c) mono-disperse Voronoi, (d) poly-disperse Voronoi-Laguerre with CV = 0.2, (e) poly-disperse Voronoi-Laguerre with CV = 0.35

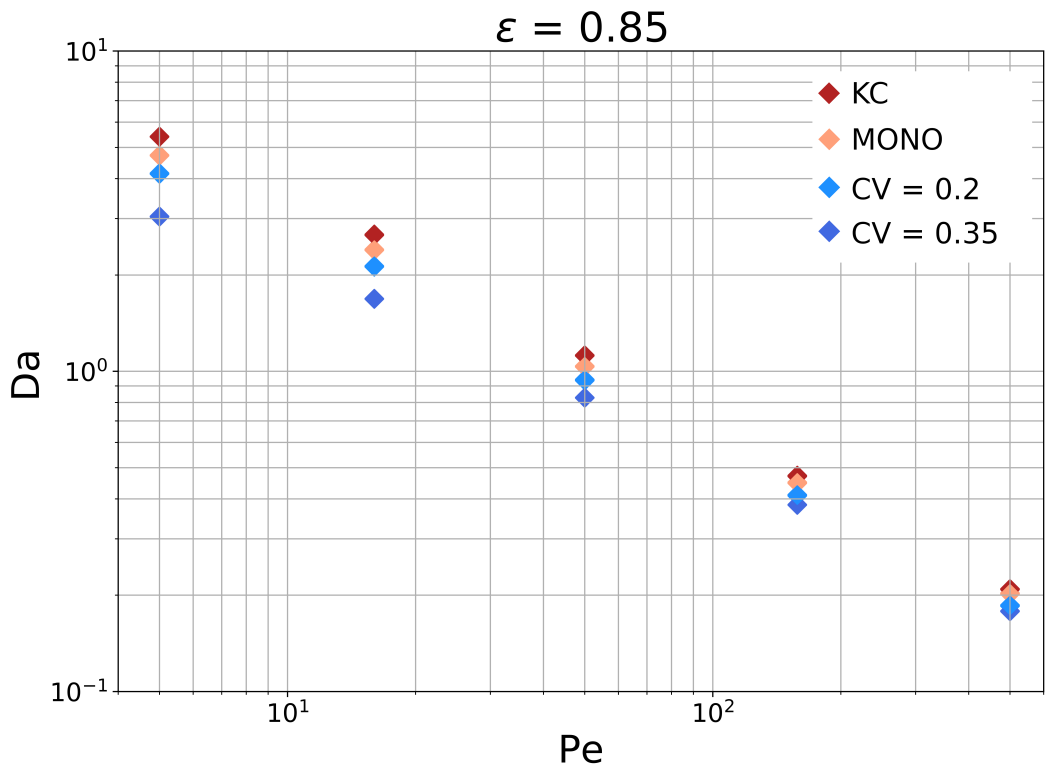

Fig. 3.10 Particle deposition efficiency, as Da at constant porosity ($\varepsilon = 0.85$) for the four different geometries showing a power-law relationship between the Damköhler number and the Péclet number.

for simplified geometries, can be used effectively for catalytic foams. However, this strategy didn't bring out any significant relationship, since the global relative error, calculated as the sum of the mean squared relative errors of the data with respect to the fitting at each Pe value, showed values well over 100%: for reference, if these correlations were able to perfectly describe the influence of porosity on particle deposition, the normalized results would collapse in a single Da-Pe power-law curve, reducing the error to zero. The underperformance of these analytical correlations was already highlighted by Boccardo et al. [32] and while it was also expected in those cases (porous foams composed of cylindrical struts) for the "Happel" model (developed for spheres arrangements), a better performance could be expected of the models based on the "Kuwabara" correlation (developed for arrangements of cylinders). Then, abandoning analytical but simplified correlations, a second approach was attempted trying to normalize the C_{KC} coefficient by adimensional numbers, i.e. ε, S_V and τ, all raised to the power of n, with the latter varying in the

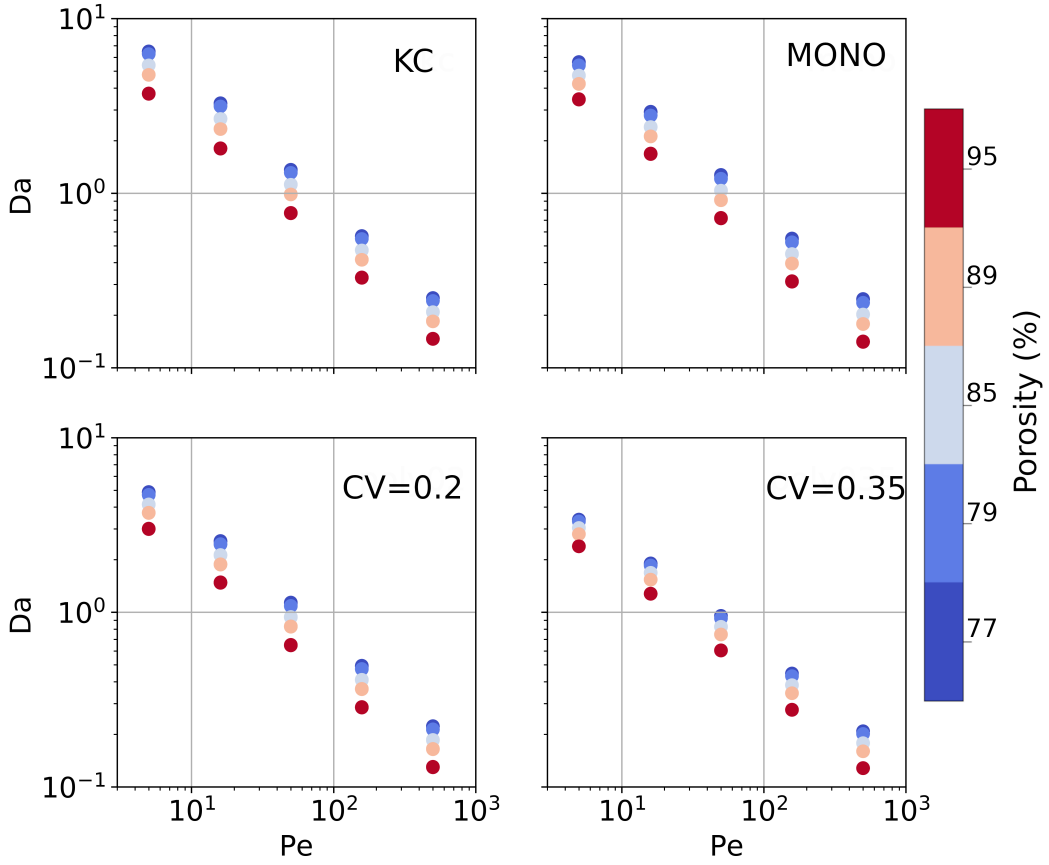

Fig. 3.11 This figure highlights the effect of the porosity on the deposition efficiency: the rate of deposition decrease for the foam with higher porosity, regardless of the geometrical model.

range $[-10;10]$. Once again the results were fitted according to a power law model and the global error was calculated. Even so, no significant relationship could be obtained. A more detailed description of this analysis, along with the correlated plots can be found in the Supporting Information available in Appendix A. Therefore, the results show how this kind of (usually employed) macroscopic geometric features are insufficient in explaining the variations in filtration performance, highlighting the need for more detailed exploration using pore-scale simulations, the objective for which this workflow was developed. Moreoever, as it is shown by Boccardo et al. [35] , the external boundary fluxes estimation have an important effect in the definition of effective parameters. In future works, more rigorous and precise definitions of the effective parameters will be considered (based for example on

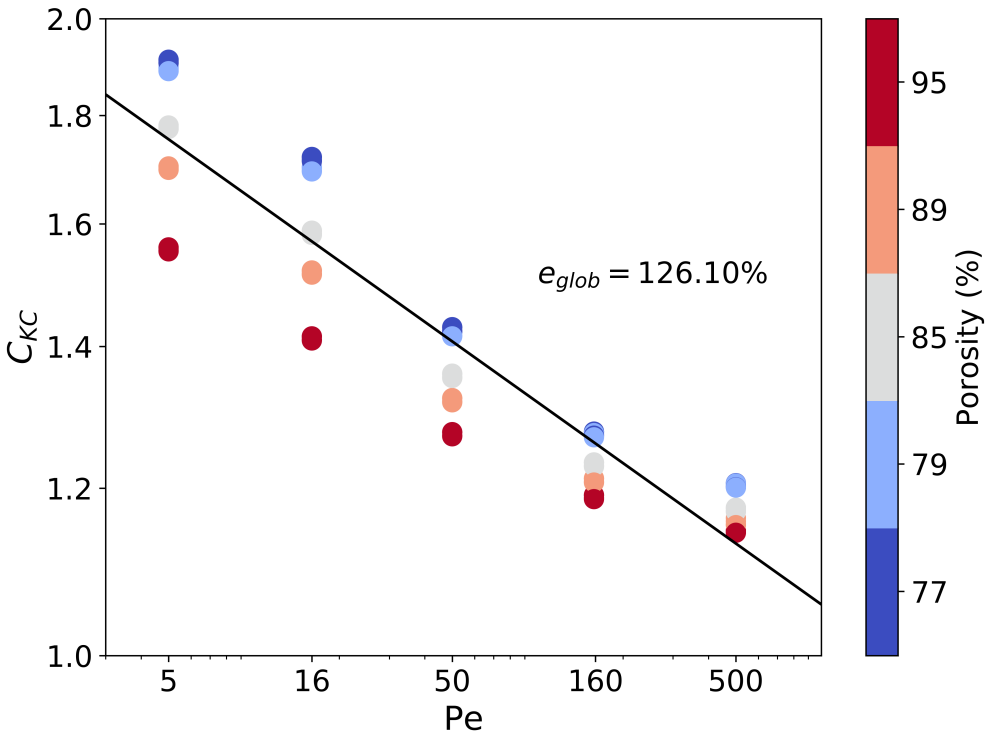

Fig. 3.12 The Kelvin's Cell coefficient C_{KC}, as function of Pe, for the poly-disperse case: this geometry was generated from a sphere packing with a normal distribution of the mean sphere diameter and coefficient of variation $CV = 0.35$. The trend line of the data set and its global error are also reported.

[73]), studying more deeply the effect of the inlet (advective and diffusive) fluxes, and the asymptotic and pre-asymptotic flow and mass transfer upscaled regimes.

3.3 Conclusions

This work shows the features of an open-source workflow which is able to generate and characterize open-cell solid foams. This in-silico tool, developed with computer graphics software `Blender` and `Python` language scripting, gives the opportunity to use different models with growing complexity in terms of pore size distribution. The choice of models ranges from the ideal periodic Kelvin's cell to random foams generated with random weighted Voronoi tessellations and poly-disperse pore size distributions. These features give the user the possibility to use this tool to investigate

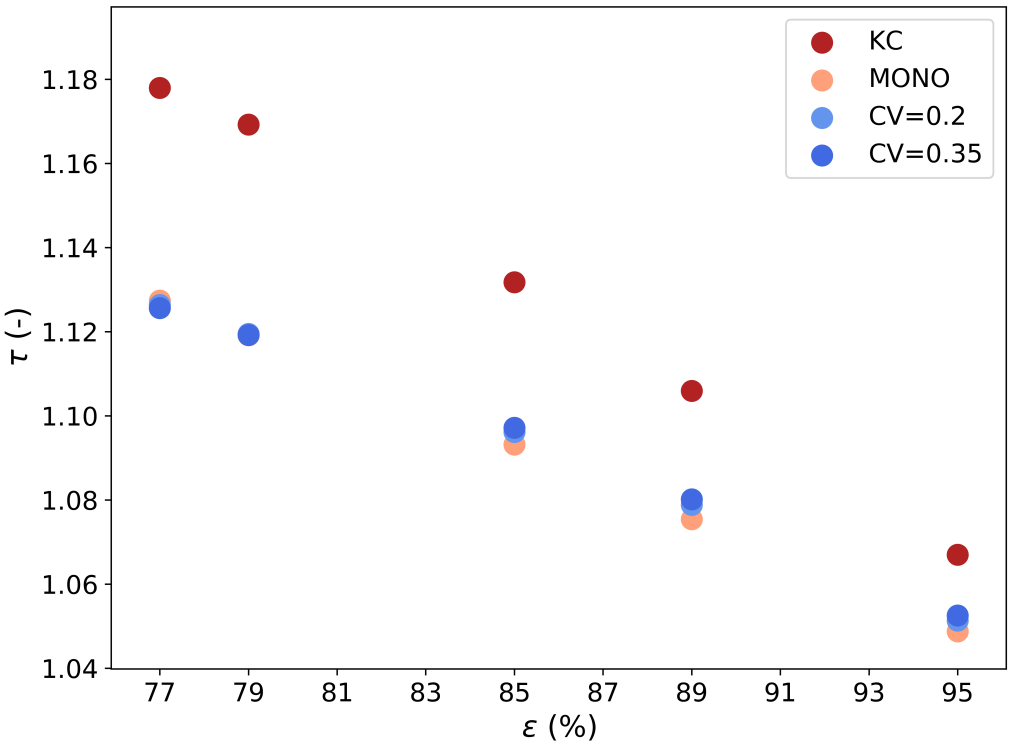

Fig. 3.13 Tortuosity, calculated with Eq. (3.3): each series of colored points is the value of τ calculated at different porosity ε for the four geometrical models (Kelvin's Cell, mono-disperse Voronoi, poly-disperse Voronoi-Laguerre with two different coefficient of variation.

several different morphologies and eventually optimize them, while the computational costs remain low. The geometries thus created have been used to perform CFD simulations, using the open-source code `OpenFOAM`, and later, as a test case, the event of an instantaneous superficial reaction/superficial deposition of colloidal particles, occurring on the solid surface, has also been investigated. The results obtained in this work by employing these models highlight that the macroscopic parameters, such as porosity, specific surface, or tortuosity alone are not enough to derive macroscopic relations to describe the particle deposition during early filtration; neither by using available and widely used (albeit simplified) analytical correlations, nor by developing new simple bespoke correlations based on these geometrical parameters. Thus, while we consider the value of the presented workflow to lie in the capacity for users to create numerical analysis campaigns at a limited cost, in particular decreasing the overhead of the foam modeling, the study of the different geometrical models and their performance in terms of colloidal particles deposition is conceived as an

example of the exploration capabilities of this workflow which we choose to limit to the work here presented. Future perspectives on this topic are then to further improve the understanding of the transport phenomena occurring inside these foams, by exploring *in-silico* a wider number of cases and especially by better discerning the geometrical peculiarities of each - beyond simple, and oft-used, descriptors like porosity or tortuosity. This motivates the choice of making the source code of this simulation platform, as well as the test cases for the simulations here presented, public and available to the community of researchers and practitioners, in order both to expand the technical capabilities of the workflow and increase the simulation data, which will prove invaluable in gaining a full understanding for these systems.

Chapter 4

An Improved Workflow For Open-Cell Foams Modelling

The aim of this Chapter is to present an innovative workflow, based on `Python` programming language and the signal and image processing software `PlugIm!` (https://plugim.fr/) to generate open-cell foam geometries using an improved version of the procedure presented in Chapter 3 and published in [3].

This improved workflow is able to reproduce a great variety of structures, like ceramic and metallic foams, and directly characterize them from the point of view of common macroscopic descriptors used for porous media, namely porosity ε, specific surface S_V and tortuosity τ. This innovative workflow makes use of a different approach for the creation of the initial *seeds* of the tessellation, namely the aggregation of spheres using a stochastic procedure proposed by Moreaud et al. [62]. Once the basic foam skeleton is calculated, the solid faction is modified using morphological operations, which results in realistic open-cell foam structures. This linking of a parametrizable procedure for the initial disposition of the spheres (hence, the foam cells) and controllable morphological operations results in a very flexible tool which gives the user the capability to represent a wide variety of open-cell foams geometries, in a format ready for use in subsequent fluid simulation software.

Moreover, the three-dimensional geometries thus obtained are validated from the geometric point of view as well as from a fluid dynamic point of view: both their geometric features and their transport properties are proven to be realistic.

Pressure drops calculated from the numerically solved flow field using the CFD codes `OpenFOAM` and `Ansys Fluent` are compared to those obtained from experimental measurements carried out on a set of two ceramic Al_2O_3 foams and two metallic NiCr ones. Additionally, CFD simulations are carried out using the reconstructed three-dimensional geometries of the experimental foam samples, obtained using the X-ray tomography technique.

4.1 Experimental and numerical details

4.1.1 Experimental set-up

Measurements of pressure drops were carried out on a vertical custom-built column packed with foam pellets in which distilled water was circulated. All the foams pellets were of cylindrical shape, having diameter equal to 44 mm and depth equal to 19 mm. The pellets were fitted co-axially inside a thermoplastic polymeric pipe, with length equal to 60 cm. This pipe was then heated in order to make it closely adhere to the pellets shapes and thus avoid any possible lateral flow bypassing the foam packing. This pipe was then fitted into a rigid polymeric pipe, with diameter equal to 6 cm and length equal to 70 cm, supported by two rubber gaskets which separated the packed column from the external pipe. The reason for this arrangement is to provide a buffer zone in both the inlet and the outlet of the packed pipe where pressure drops probes could be placed.

The custom-built column was connected to a water tank and a volumetric pump using 1/4 inch plastic pipe and the water flow-rate was adjusted using a needle valve. The differential pressure measurements were carried out by a differential pressure gauge connected to the inlet and outlet buffer zones of the packed column. The measuring device model is *EMERSON* with a working range of 0 - 620 mbar or 0 - 4 bar. Measurements in the range 5 - 60 mbar have a confidence interval of $\pm$ 1.1 mbar whereas measurements between 50 and 1000 mbar have a confidence interval of $\pm$ 4.9 mbar. A schematic representation of the experimental set-up is reported in Fig.4.1.

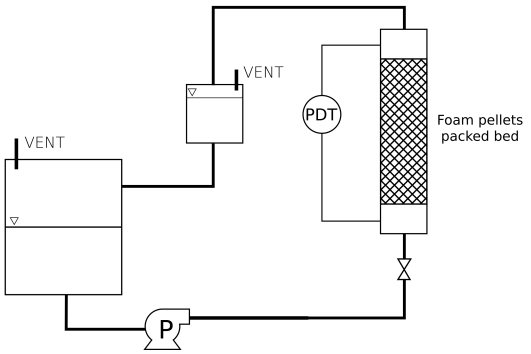

(a) PFD diagram

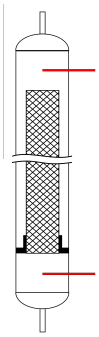

(b) A detailed view of the packed column

Fig. 4.1 The experimental set-up of the experimental measurements of the pressure drops across a foam packed column are here reported. When heated the pipe adhere firmly on the outer foam pellets surface, avoiding any lateral bypass. The packed pipe is then fitted inside a larger poly-carbonate pipe, thanks to a custom printed rubber gasket (represented in black in 4.1b).

4.1.2 Real foam samples details

For this work four different open-cell foams were investigated, two ceramic Alumina foams (Al_2O_3), respectively 20 and 40 PPI, and two metallic Nickel-Chrome foams (NiCr) respectively 14 and 30 PPI. For the latter the manufacturer provided an approximate measure of the specific surface and porosity, whereas for the ceramic foams no geometrical details were available.

In order to get a more rigorous description of the geometric parameters, the foam micro structure was obtained using the X-ray tomography technique. The stacked grey-scale `TIFF` images were segmented into binary ones using the Otsu thresholding method [74]. The binary images can be then easily exported into three-dimensional array in `Python` and used to perform micro-scale analysis to extract the size distribution respectively for the foam cells, windows and struts diameters (d_C, d_W, d_S), as well as calculate the porosity, the specific surface and the *Representative Elementary Volume* (REV) and the geometric tortuosity. To perform these analysis two main tools were used: the already cited free-software `Plug Im!` and the `Python` module `PoreSpy` [75] and the open-source software `Paraview` [76].

These softwares have a large library of functions and algorithms that are essential in the analysis of binary images of porous media. Images were first pre-processed using the *flowing bilateral filter* [77], available in `Plug Im!`, which reduces the

noise due to X-ray scattering on the solid surface of the foams, especially in the case of the metal ones, homogenizing the color intensity of the solid areas, allowing more precise void/solid threshold definition. Once the image is segmented and imported in a `Python` environment as a 3D binary array, in which the value 0 was arbitrarily assigned to the solid fraction and 1 to the void fraction, the porosity is easily computed as the mean value of the whole array. In some cases, the foams samples present solid structure with inner voids, due to the destruction of the original polymer foam during the manufacturing process. These internal voids must be filled otherwise they will unphysically increase the values of ε and S_V: while these zones are in fact void, they are not available to the fluid flow and as such are effectiely to be counted together with the solid zone. This is easily achievable since most of the codes used provide an hole-removing function which fills all void areas not directly connected to the edges of the array.

The REV can be computed by sampling the porosity of a n cubic sub-array of random size across the whole matrix, using a `PoreSpy` function which implements a method proposed by Bachmat et al. [78]. Within the same environment, the pore-network of the foam can be extracted using a method proposed by Gostick et al. [79]: this operation subdivide the overall geometries in sub-regions which represents the macro-pores, corresponding the the foam *cells*, and *throat* connecting these sub-regions, which correspond to the foam *windows*. The algorithm calculates the equivalent diameter of each of such pores and throats. The same calculation can be performed on the inverted image to obtain a size distribution on the solid fraction, from which the struts size-distribution can be calculated.

The geometric tortuosity of the structures, defined as the ratio between the geodesic and euclidean distance between two random points $\tau = \delta_{geod}/\delta_{Eucl}$, was estimated using the `Plug Im!` function *Graph-based Tortuosity* [80, 81], which after calculating the pore-network of the geometry, with an analogous operation as the one performed by `PoreSpy`, used the pores centers as nodes of a discrete graph and their connections as edges. Considering a couple of random nodes in the void fraction of the volume, the geodesic distance δ_{geod} is the sum of the graph edges connecting the two nodes. Finally, the specific surface can be calculated by extracting the solid surface applying the *Marching Cubes* algorithm and then computing the solid surface of the foam, divided by the sample volume. A synthesis of the properties of the investigated foams is reported in Tab. 4.1.

Foam label	NiCr14	NiCr30	Al_2O_320	Al_2O_340
Material	NiCr	NiCr	Al_2O_3	Al_2O_3
PPI	14 11 – 17 (*mfr.*)	30 27 – 33 (*mfr.*)	20	40
ε (%)	91.9 (*Tomo X*) 92 (*mfr.*)	92.1 (*Tomo X*) 92.2 (*mfr.*)	75.9	75.7
S_V (m^2 / m^3)	1054 (*Tomo X*) 1000 (*mfr.*)	3091 (*Tomo X*) 2800 (*mfr.*)	852	1715
τ (–)	1.24	1.22	1.2	1.17
Sample size (mm)	16.9	9.0	19.3	19.3
d_C (mm)	2.4	0.79	3.3	1.8
d_h (mm)	3.5	1.2	3.6	1.8
d_W (mm)	0.95	0.37	1.8	0.92
d_S (mm)	0.4	0.25	1.95	0.55
Tomo X sampling (voxels/µm)	24	16.9	50	50

Table 4.1 The physical and macroscopic properties of the foam samples used in this work. For both the metallic NiCr foams the values of PPI, ε and S_V are reported as nominally declared by the manufacturer and as measured from the X-ray tomography images analysis. For the ceramic foams only the values obtained from the image analysis were available. The values of d_C, d_W and d_S represent the average value calculated from the size distributions obtained by performing pore-network analysis using the `PoreSpy` software.

4.1.3 Foam generation workflow

The generation of digital replicas of the examined open-cell foams is carried out using a procedure already delineated in Chapter 3, but here heavily updated in order to achieve a realistic representation of the foam structure at the pore-scale. The procedure can be summarized as follows: first a set of spherical objects is packed inside a confined space. Afterwards, the positions of these spheres are retrieved and used as starting seeds for the computation of a Voronoi tessellation, which subdivides the space of the initial box into cells around the initial spheres. Then, spheres are placed at the nodes of the tessellation and cylinders at its corresponding edges connecting two nodes, thus generating a foam skeleton, with a *ball-and-sticks* model. Finally, the initial skeleton is modified to achieve the more realistic features that characterize an open-cell foam.

The novelty of this workflow resides in the fact that all the geometric procedures, i.e. the first, third and fourth steps, are carried out in voxelized binary three-dimensional volume, which allows for fast and powerful computations over solid binary volumes, compared to other methods which works over the solid surface [3], or the software Surface Evolver [31]. Moreover, there is a great deal of user freedom in the use of this tool, as these steps are extensively parametrizable, resulting in deep control on the obtained structures geometry and features.

The workflow to generate geometries as described above, makes use of `Python` scripting and, most importantly, several modules of the free software `Plug Im!` [82], which is used for the initial spheres generation procedure and the binary geometry manipulation. The theoretical background and the equations involved in the generation of digital foam models, namely the Voronoi algorithm, the morphological operators and the spheres aggregation process are reported in Section 2.3.2, as well as the procedure for the processing of tomography images to obtain reconstructed three-dimensional real foam geometries.

From the analysis on the pore network of the foams samples studied in this work, carried out using the `PoreSpy`, useful information can be extracted for the generation of digital replicas of the structures in exam. In particular, it is possible to define the dual structure of a foam, namely the foam pores' *equivalent spheres* packing, composed by the largest spheres fitting inside the foam cells and having their same volume. From this dual entity two key properties are identified: the dual packing

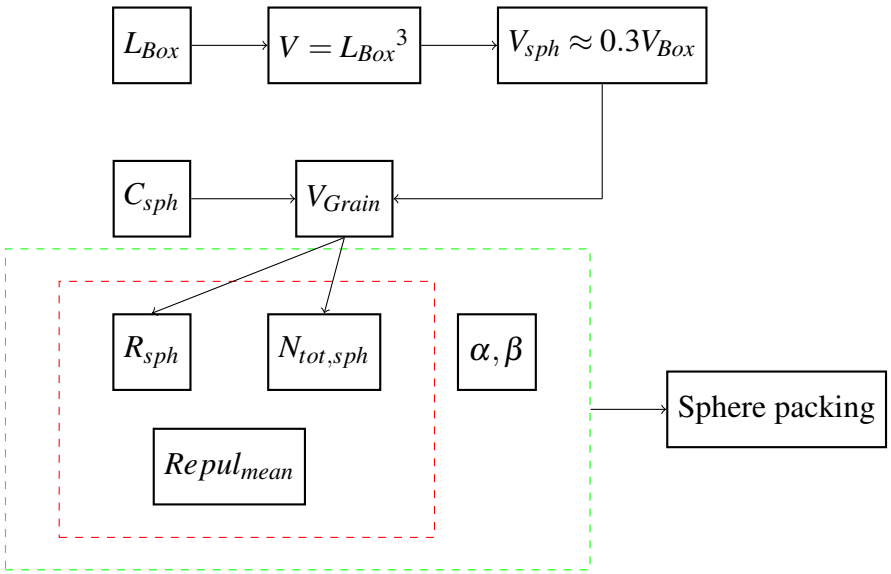

Fig. 4.2 This flowchart describes the strategy used to derive the values of the number of spheres $N_{Tot,Sph}$, their radius R_{Sph} and the repulsion, $Repul_{mean}$ used as input parameters for the sphere aggregation process. Given an initial box dimension, a *sphere concentration* C_{Sph} it is possible to obtain retrieve the number of spheres and their radii to be aggregated. The repulsion and the concentrations are, in turns, calculated from the analysis of the tomography images of the foam sample in exam. The compactness parameters of the aggregate, α and β can be taken arbitrarily to satisfy the sphere concentration constraints.

porosity ε_{dual}, defined as the ratio between the void fraction of the packing and the volume of the containing bounding box, and the spheres *concentration* $C_{sph,dual}$, defined as the ratio between the total number of spheres and the volume of the bounding box, the latter expressed in cubic voxels. An important result is the fact that independently of the foam sample the value of $\varepsilon_{dual} \approx 0.3$, which is is a typical value for a very dense sphere packing where the spheres may overlap.

The information extracted from real foams equivalent sphere distribution were used to obtain the spheres aggregate that could then be used to generate in-silico structures to replicate the original foams. A flowchart representing the calculation of the parameters needed for the sphere aggregation process is reported in Fig.4.2. The volume of a single grain in the aggregation step is obtained with the hypothesis of representing roughly the 30% of the total available volume and complying with the sphere concentration constraint. This leads to grain radius R_{sph} and the maximum number of spheres to be packed. The choice of α, β and the repulsion *Repul*

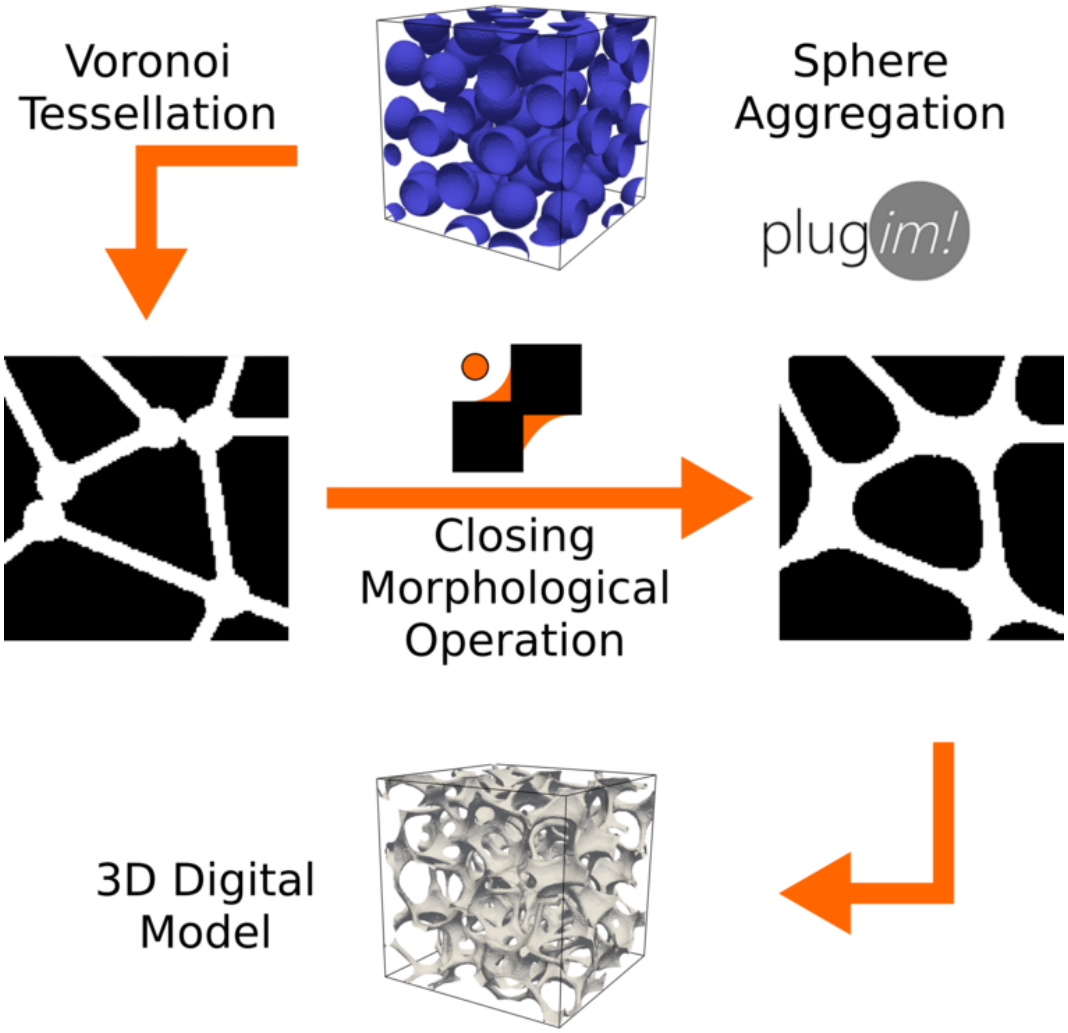

Fig. 4.3 The foam generation workflow graphical representation: a sphere aggregate is obtained using `plugIm!`(step 1) as the seeds of the tessellation. Voronoi algorithm is computed and edges and nodes of the cells are extracted. A three-dimensional voxelized binary image is created by assigning cylinder and spheres to struts and nodes respectively, to create a balls & sticks foam skeleton (step 2). The skeleton is modified by a morphological *closing* operation (step 3). The final three-dimensional geometry is generated by contouring the solid surface with the Marching Cubes algorithm, obtaining an `.stl` file (step 4).

parameters, introduced in 2.3.3 is not unique, but several combinations of these aggregation parameters lead to a starting sphere packing compliant with the initial constraints.

So called *aggregation maps*, comprising all the possible instances of the random spheres aggregation process, can be obtained. Each of the positive cases can lead to a different realization of the random aggregation process, possibly giving geometries that can vary in topology but having similar macro-descriptors. An examples of these maps is reported in Fig.4.4. The shape of the *admissible* areas, marked with an `x` symbol, is such that if α increases, namely the probability of a sphere being placed into a convex zone of the aggregate, β, i.e the probability of the convex location being closer to the center of mass of the aggregate, decreases. This is actually intuitive, since the goal of desired aggregate is to *distribute* sphere as heterogeneously as possible inside the computational box. The inverse is also true, meaning that higher β values requires lower values of α. The *admissible* zone decreases in dimension for increasing values of repulsion as demonstrated by Fig.4.4b. This aspect was not investigated further for this work.

Once an aggregate is chosen randomly between all the possible instances, the spheres centroid are extracted, a Voronoi tessellation is computed and the edges and nodes of the tessellation are extracted. On a binary voxelized domain, with the same lateral dimension L as for the initial packing, the nodes are represented by spheres and the edges by cylinders. This structure is the foams *skeleton*. The diameters of these initial shapes are chosen empirically in order to fit the final desired porosity ε. For metal foams the node-to-edge ratio $R_{node}/R_{edge} \leq 2$, whereas for ceramic foams this ratio can be higher than 3. This initial skeleton must be further modified using a *Closing* operator (cf. §2.3.5). The dimension of the structuring element for this operation is also empirically adjusted in order to generate a foams structure whose macro-descriptor, porosity ε, specific surface S_V and tortuosity τ, matches those of the original foam sample. A graphic representation summarizing the described steps is reported in Fig. 4.3.

4.1.4 CFD simulations

The solution of Eq. 2.1 and Eq. 2.2 to calculate the flow field inside the foams geometries is carried out using the CFD numerical simulation software `Ansys Fluent`

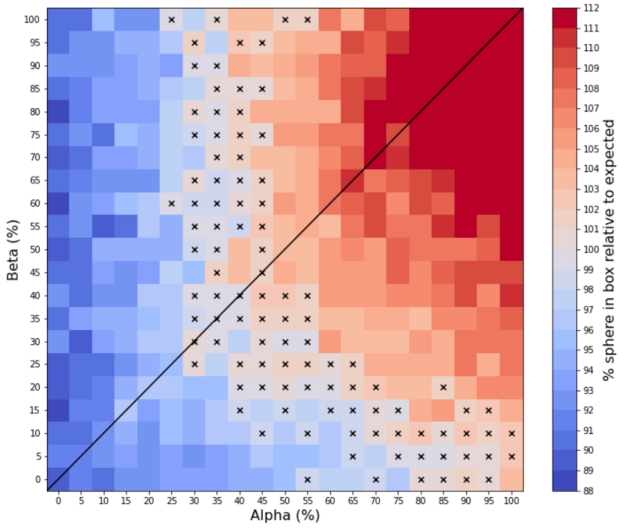

(a) Compacity map at fixed repulsion

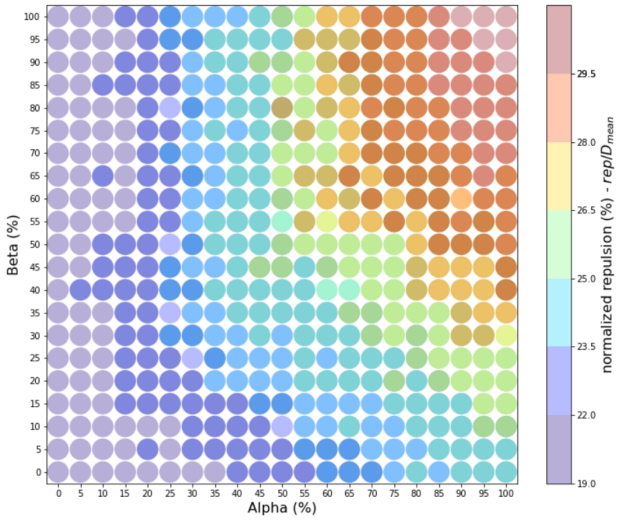

(b) Positive values at varying repulsion

Fig. 4.4 An example of the compacity maps are here reported: The contour plot of Fig.4.4a represent the *sphere concentration* parameter C_{Sph} relative to the expected parameter for a given foam as a function of α and β aggregation parameters, at a given value of repulsion. The coloring indicated how close or distant is a certain realization of sphere aggregates from the aim C_{Sph} value. The values marked with an x symbol represents those instances where the values was within a 2% error with respect to the target. The second image collects all the acceptable combination of α and β, varying the repulsion between the spheres of the aggregate.

2020 R2 [83], based on the finite volume method, with computational grids generated using utilities available within the OpenFOAM 7 software. From the obtained solution the pressure drops per unit length across a foam sample was calculated. In the first paragraph of this section, a brief description of the computational mesh generation is reported, while in the second paragraph the simulation set up and the boundary condition used are described.

Mesh generation Once a foam geometry is created, either deriving from tomographic images or generated in-silico using the workflow described in section 4.1.3, it is exported in .stl format. This file format describes the discretized surface of a solid structure by means of a triangulated mesh and it is also the format of choice to define geometries to be meshed in OpenFOAM 7.

The void/fluid fraction meshing procedure is carried out in two main steps: first a *background* structured hexahedral mesh is generated by the OpenFOAM utility blockMesh. This hexahedral mesh is used as a starting point to build a *body-fitted* grid generated by the utility snappyHexMesh, also part of the OpenFOAM suite. Given the main flow direction, which is arbitrarily chosen in the x-axis direction, the blockMesh bounding box has the same dimension of the foam sample in the y- and z-axis directions, whereas along x, on both inlet and outlet direction, a buffer zone is considered, amounting to around 5% of the total foam sample length.

The meshing strategy follows the same procedure described in section 3.1.2, adapted to the larger size of the geometries considered, thus resulting in computational grids with a number of cells raging between 5 to 7 millions, constituted mainly by hexahedral cells, ensuring good numerical performance for the solver.

The mesh is more refined closer to the solid walls, while moving farther away from the solid towards the bulk of the fluid, cells have increasing dimension. Thus, the resulting computational grid have a larger number of small cells where gradients are higher, whereas in the bulk of the fluid, where stresses are lower, the cell density is lower, thus reducing the total computational cost.

Flow field solution Numerical simulations were carried out using the CFD code Ansys Fluent 2020 R2. The computational domain used in all the simulations performed for this work has dimensions $L_x \times L_{y,z} \times L_{y,z}$ and is symmetrically centered at the origin of the axes with the diagonal vertices respectively $x_{max/min} = \pm L_x/2$ and

$y_{max/min}, z_{max/min} = \pm L_{y,z}/2$. Whereas the latter are chosen in order to make the foam sample completely fit inside the computational box, along the x-axis direction extra volumes are added on both sides of the foam geometry, to create pre/post-mixing areas.

The flow field is initialized by setting the inlet velocity equal to the superficial macroscopic velocity V on the inlet patch, a x-normal surfaces with coordinates $x_{Inlet} = -L_x/2$. At the outlet, with coordinates $x_{Outlet} = L_x/2$, a relative gauge pressure equal to 0 is specified. A *no-slip* condition for the velocity U is applied at the solid surface of the foam, whereas at the remaining sides of the domain a *symmetry* boundary conditions is applied, implying no fluid motion across those. The specific dimensions of each foam sample are reported in Tab. 4.1. A schematic graphical representation of the computational domain is reported in Fig.4.5.

The Newtonian incompressible fluid here considered is water, with density ρ = 997.78 kg m^{-3}, kinematic viscosity μ = 9.77 $\times$ 10^{-4} kg m^{-1}s^{-1}; being the solver used incompressible these quantities only serve to derive the specific simulation Reynolds number. The system is solved using the solver `SIMPLE`, at a constant temperature $T = 293K$ (the energy equation was not solved) in steady-state conditions. The Reynolds number for this work is defined as $\mathrm{Re} = U \cdot D_h/\nu$, with the hydraulic diameter of the foam, $d_h = 4\varepsilon/S_V$, where S_V is the ratio between the volume and the surface of the solid.

The flow is solved with a laminar viscous model for up to $Re \leq 150 \sim 200$, values over which the flow has too much instabilities for this model and it is necessary to use a model for turbulence [40]. The turbulent model used for higher Re number simulations is `Realizable` κ-ε with a standard wall function.

4.2 Results analysis and discussion

In this section the results of the foam generating workflow are presented, and the pressure drops calculated using numerical simulations and experimental measurements are compared. The first part will be dedicated to comment the results of the geometry generation, whereas in the second part the results of pressure drops will be discussed.

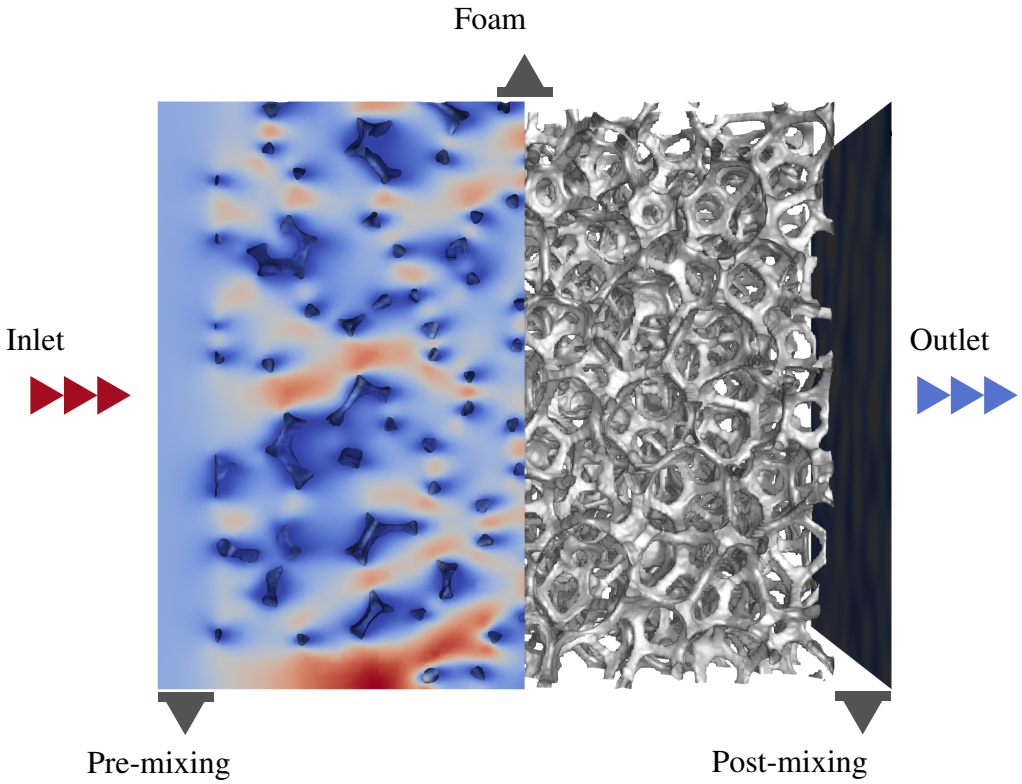

Fig. 4.5 The figure is a schematic representation of the computational domain and the boundary condition used: the inlet coincide with the negative x-normal face, followed by the pre-mixing volume. Conversely, the outlet coincide with the positive x-normal face, preceded by the post-mixing zone. A no-slip condition is used at the solid walls surface of the foam.

4.2.1 Geometrical validation

The workflow presented in section 4.1.3 was used to generate a digital replica of a sample of the foams used for the pressure drop experiments and tomography investigation, reported in Table 4.1. The generation parameters were varied in order to obtain foam structures such that their macroscopic descriptors (ε, S_V, τ) will have a relative error compared to the data extracted from the tomography images, no greater than 5 to 10 %. The foam samples obtained are then scaled to match the tomography data in order to perform a comparison. The results of this procedure are summarized in Table 4.2 and the corresponding input parameters used are reported in Table 4.3.

The geometries obtained are in good agreement with the original foams: the relative errors, for each of the target parameters, are well within the acceptability range. This shows how the generation procedure can be fine tuned to create the digital foam that replicates the desired descriptors with great accuracy. It should be noted that each set of the generating parameters reported in Table 4.3 represent one of the possible sets that can lead to the same result.

As reported in 4.1.3 and shown in Fig.4.4, the values of α, β and Rep are not unique, so different combinations can lead to foam structures different at the local scale but with the same macroscopic parameters. The computational cost for each sample is always very small, approximately 300/400 seconds in single-core runs on a Windows 7 workstation with a Intel Xeon E5-2620 @ 2.00GHz CPUs on 6 cores and 48 GB of RAM.

Figure 4.6 and Fig. 4.7 show a graphical comparison between the three-dimensional reconstructed foams and their digital replica. It is evident that this workflow is able not only to capture the macroscopic descriptors most commonly used to classify porous materials, but it also creates a realistic geometry from a qualitative point of view. Moreover, it can be observed that for the case of the metal foams (`NiCr14` and `NiCr30`), the struts shows the typical triangular cross-section profile associated with them. Figure 4.8 compare a local portion of the `NiCr14` foam and its replica, the first obtained from a slice of the tomography, the second from the .TIFF file generated by the workflow. These images as well as the previous ones show that this phenomenon tends to be more evident closer to the struts-nodes intersection, rather than at the

Target foam	ε (%)	S_V (m^2 / m^3)	τ (–)	$e_{r,\varepsilon}$ (%)	e_{r,S_V} (%)	$e_{r,\tau}$ (%)
NiCr14	92.5	996	1.17	0.6	3	5.6
NiCr30	92.2	2714	1.17	0.1	4.7	4
$Al_2O_3$20	75.2	854	1.19	0.9	0.3	0.1
$Al_2O_3$40	74.3	1737	1.18	2	1	0.9

Table 4.2 The table summarizes the macro-descriptors of the foam digitally generated with the presented workflow. The error with respect to the original foam samples are also reported. The relative errors are in all cases within an acceptable 10% error range and below.

Target foam	Sphere aggregation				Foam skeleton		Closing morphing
	α	β	R	Rep	N	S	tv
NiCr14	0.5	0.45	32	16	10	4	18
NiCr30	0.55	0.95	17	9	5	2	15
$Al_2O_3$20	0.55	0.75	25	20	11	9	15
$Al_2O_3$40	0.7	0.7	14	6	7	3	8

Table 4.3 The table reports the input parameters of the workflow used to obtained the final digitally generated foam replicas. The values of α and β are probabilities (cf. 2.3.3), thus ranging between 0 and 1, whereas the values for R, Rep, N, S, tv are reported as integer numbers indicating *voxels*, since they are referred to the three-dimensional voxel matrix used within the `plugIm!` environment to generate and modify geometries (cf. 4.1.3).

very center of the struts, where it conserves the initial circular cross-section given by the initial skeleton.

The authors deem this a remarkable feature, which is not intended by design, but is the direct result of the *Closing* morphological operation, which seems to modify the solid fraction of the binary image in the same way as the superficial tension distributes the solid during the creation process of a real foam. This peculiarity is not present on the ceramic foams replicas ($Al_2O_3$20 and $Al_2O_3$40), which have lower void fractions. These results confirm that the workflow is able to generate realistic foam structures on different level of quantitative, qualitative, and geometrical description.

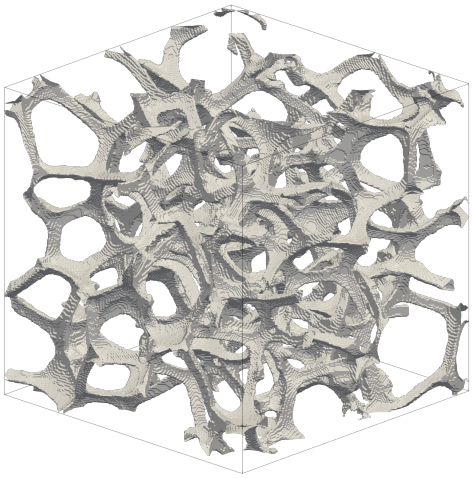

(a) NiCr 14 PPI Tomography

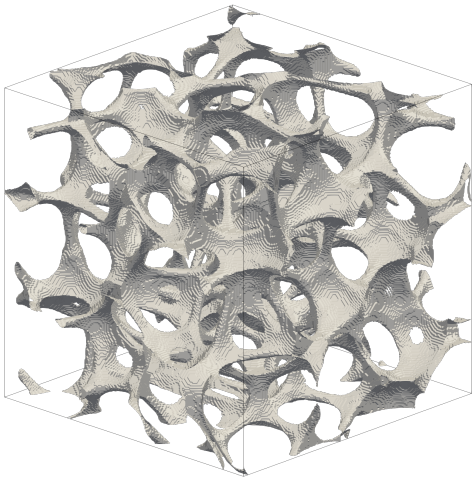

(b) NiCr 14 PPI PlugIm!

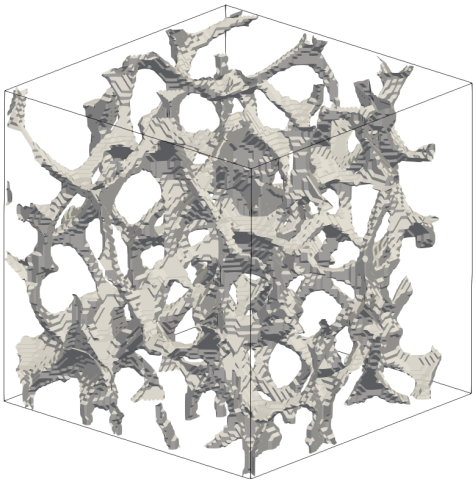

(c) NiCr 30 PPI Tomography

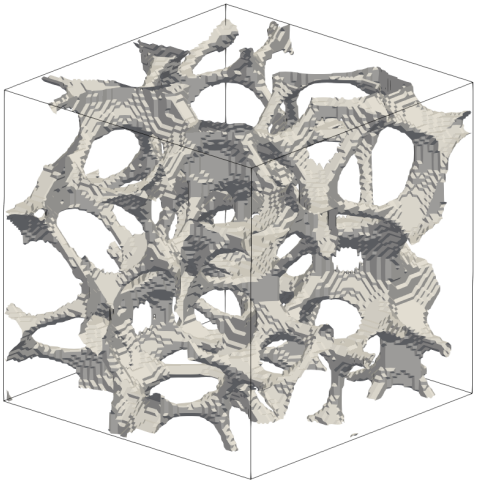

(d) NiCr 30 PPI PlugIm!

Fig. 4.6 A comparison between the original metallic foam geometries and their replicas: Fig.4.6a and 4.6b for the NiCr 14 PPI foam and Fig.4.6c and 4.6d for the NiCr 30 PPI foam. The slender and boen-like structure of the struts and strut-node intersection is well captured by the generation process thanks to the intrinsic properties of the morphological *closing* operation.

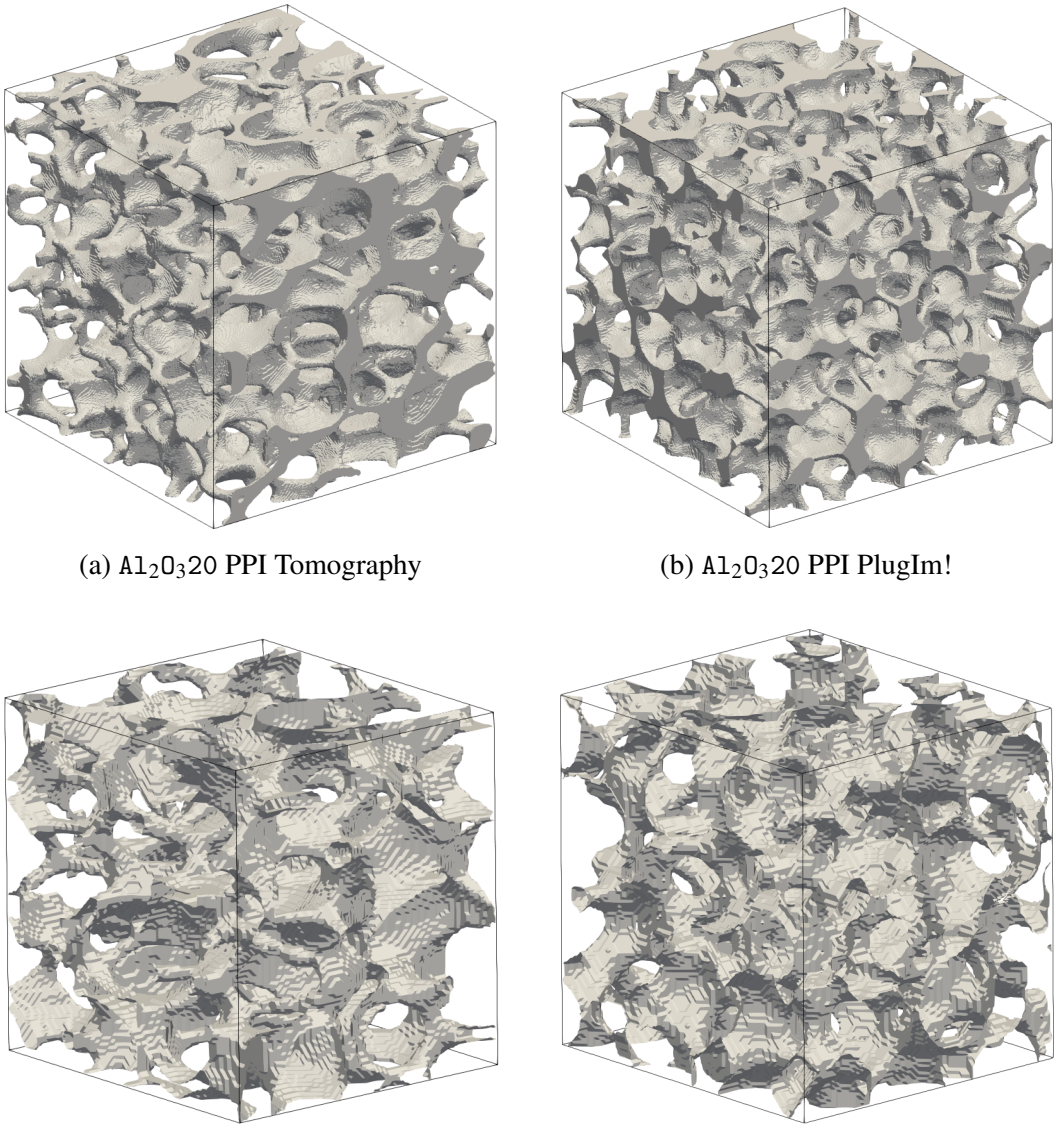

(a) Al_2O_320 PPI Tomography

(b) Al_2O_320 PPI PlugIm!

(c) Al_2O_340 PPI Tomography

(d) Al_2O_340 PPI PlugIm!

Fig. 4.7 A comparison between the original ceramic foam geometries and their replicas: Fig.4.7a and 4.7b for the Al_2O_320 PPI foam and Fig.4.7c and 4.7d for the Al_2O_340 PPI foam. In this comparison can be remarked how the *relatively* lower solid fraction, around 75%, lead the morphological operation to the fusion of several close objects, namely cylinders for struts and spheres for nodes, into a unique feature, just like in real foams. This would be not possible if defining the single edges and nodes of the tessellations as separate objects, as done for instance in [3].

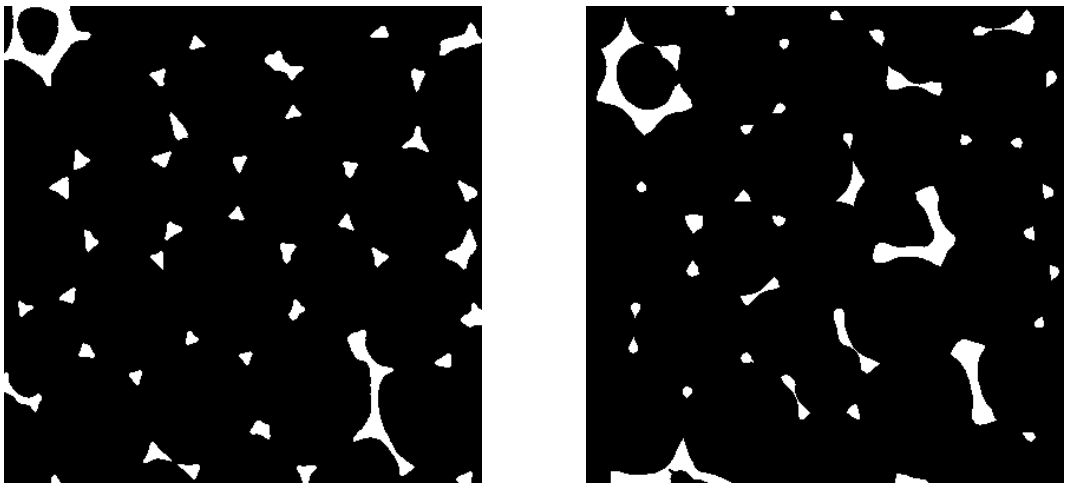

(a) NiCr14 PPI Tomography slice detail (b) NiCr14 PPI PlugIm! slice detail

Fig. 4.8 The figure show a comparison between the details of a slice of the TIFF staked-images from the NiCr14 tomography and the NiCr14 replica. It is remarkable how the *closing* operation, manages, for this highly porous structure, to smear and modify the solid fraction to the point that the cross-section of the struts and struts-nodes intersection have a triangular shape, reproducing a feature present only for metal foams, without any pre-determined shape or parameter.

4.2.2 Pressure drop results

Despite the importance of the notable results obtained from a geometrical point of view reported in the previous section, these macroscopic descriptors, used as a validation parameter for the workflow, are a volumetric average measure of the geometric features of the porous media. Although very important for the characterisation of such materials, they may not be sufficient in describing the transport phenomena occurring inside the foams at the pore-scale. These phenomena are strongly influenced by the local heterogeneity of the structure, and as such they may not be captured by these commonly used descriptors widely used in this field.

Therefore, it is important to investigate and compare the pore-scale fluid flow inside the foams and the resulting pressure drop. An experimental approach at the scale of the pores is, in most cases, complex and expensive, because of the need of set-ups coupling index of refraction and laser-diagnostic techniques [84]. CFD numerical simulation can be used instead to simulate the pore-scale fluid dynamics in porous media [3, 34] at reduced costs.

Average operating conditions for NiCr30, Al_2O_320 and Al_2O_340											
Q_L (L/hr)	12.5	25	50	100	200	400	600	800	1000		
$V_{L,S}$ (mm/s)	2.3	4.6	9.2	18.4	36.5	73	110	150	180		
Average operating conditions for NiCr14											
Q_L (L/hr)	12.5	25	50	100	158	251	350	520	705	850	950
$V_{L,S}$ (mm/s)	2.3	4.6	9.2	18.4	30	46	64	95	129	155	174

Table 4.4 The operating conditions, namely volumetric flow-rate and resulting superficial macroscopic velocity in the packed column, used for the experimental measurement and to solve the flow-field using the CFD numerical simulations.

For this work the single-phase flow field of a liquid, i.e. water, is solved across a foam sample, obtained from x-ray tomography images, using numerical simulation over a wide range of operating conditions, varying the water flow rate. The pressure drop per unit length $\Delta P/L$ across the sample is also calculated. These results are compared with differential pressure drop measurement carried out on a column mono-axially packed with foam pellets using the set-up described in 4.1.1.

Finally, the same set of simulations are carried out using the foam replicas produced by the workflow described in the previous section and the results are compared. The simulations were carried out on HPC@POLITO cluster **Legion** (https://www.hpc.polito.it/legion_cluster.php) composed by 57 computing nodes of 2x Intel Xeon Scalable Processors Gold 6130 2.10 GHz with 16 cores. The cases has been solved in parallel mode, using 8 cores per case, resulting in a wall-clock time per case of around 2 hours with `Ansys Fluent 2020R2`.

The operating flow rates taken into account for the experiments, later replicated with the simulations, range between 12.5 and $\sim$ 1000 L/hr, resulting in superficial velocities ranging between 2 and 18 mm/sec. The Reynolds number values differ for each foam, based on their hydraulic diameter d_h. Tab. 4.4 report the complete list of the average values of Q_L and V used for the experiments.

The results for the $\Delta P/L$, calculated from the experimental measurements and the simulations, as a function of the Reynolds number, are reported in Fig. 4.9, together with the values obtained from two common literature correlations developed for open-cell foams and based on a wide collection of experimental values, proposed by

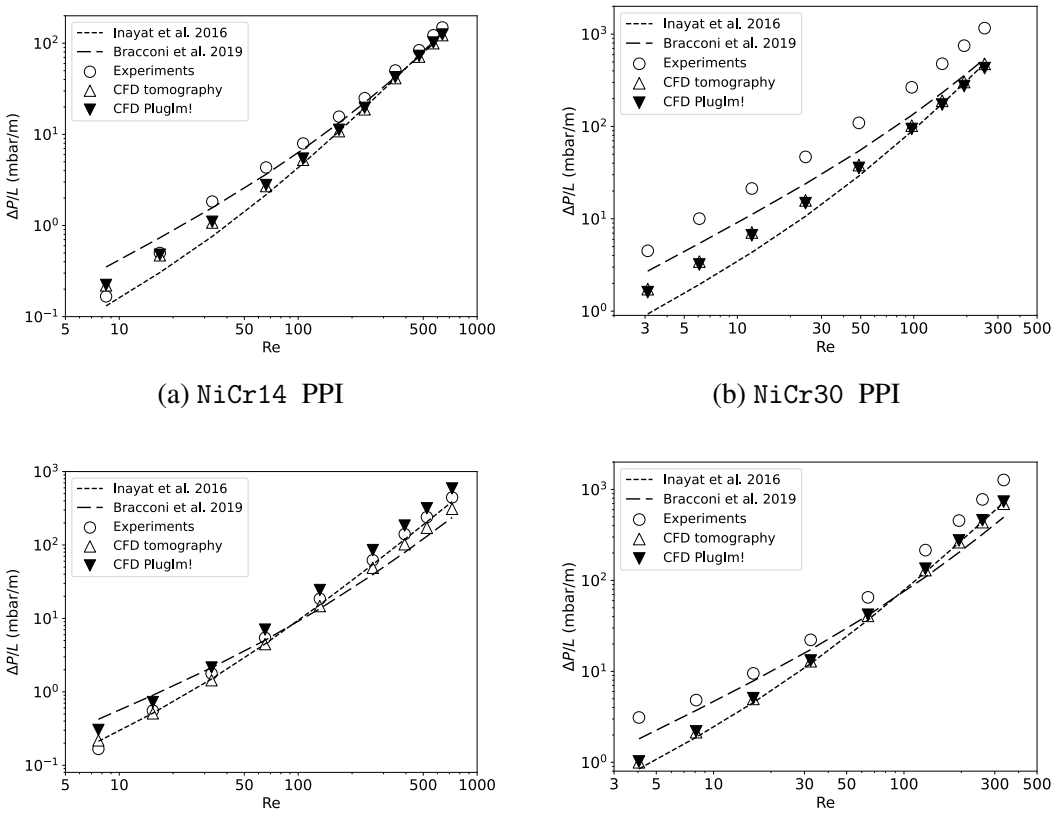

(a) NiCr14 PPI

(b) NiCr30 PPI

(c) $Al_2O_3$20 PPI tomo

(d) $Al_2O_3$40 PPI

Fig. 4.9 The figure show the results and comparison of the $\Delta P/L$ experimental measurements and calculations derived from the numerical CFD simulations for the real foam samples, obtained elaborating X-ray tomography images, and the digital generated geometries using the workflow proposed in this Chapter.

Inayat et al. [85] or a mix of experiments and CFD results, proposed by Bracconi et al. [86].

The experimental pressure drop values measured for this work are in agreement with the those predicted by the correlations, despite a general shift towards higher values. This is to be attributed to the column set-up that may have created additional losses not caused by the foam packing itself. Because of the particular arrangement it was not possible to correctly estimate these additional shifts. The results of the CFD simulations carried out on the geometries extracted from the tomography images are in very good agreement with the correlations showing how this method can give an accurate description of the macro-scale phenomena using simulations over a small (but representative) sample of foam.

Finally, also the numerical simulation results obtained from the geometries generated by the workflow presented in this work show a good agreement with correlations, simulations on the original samples and experimental results. The only case where the difference in $\Delta P/L$ is greater is for the Al_2O_320 case, despite the fact that in terms of geometric structure (i.e. their integral descriptors) this is the replica showing the smallest error of all. A possible interpretation can be the fact that despite good agreement in terms of macro-descriptors, the micro-structure is still not well captured by the the digital twin. Overall, this present foam generation workflow shows its potential in creating open-cell foams structures replicas, which have good results in terms of pressure drops prediction, in agreement with different levels of validation: geometric, experimental, literature correlations and CFD analysis of tomography data.

4.3 Conclusions

This work proposes an innovative workflow for the generation of cellular porous material like open-cell foams with different set of morphological features, most often associated with the foam material. The procedure describing the generation of the geometries is reported in detail. The generated structures are validated both in terms of geometric macro-descriptors and micro/macro-scale transport phenomena, in particular momentum transport. For the latter, pressure drop measurements obtained through different methods are compared: experimental differential pressure over a foam pellets packed column, CFD simulation through a real foam sample obtained from X-ray tomography technique and also on a structure digitally generated making use of the newly proposed workflow. Moreover, pressure drops correlations from the recent literature [85, 86] are also used as reference.

The performance of the new workflow is promising: using the right set of input parameters it is able to generate a digital twin of a target foam sample with a good level of accuracy in terms of geometric macro-descriptors (ε, S_V and τ) of the real open-cell foam, as well as a good qualitative/graphical reproduction of the features of such materials, e.g. struts with triangular cross-section of metallic highly porous foams. Moreover, this digital replica has very good performance in predicting the pressure drops $\Delta P/L$, calculated by means of numerical CFD simulations, of the real foam, indication of good accuracy in catching the micro-scale transport phenomena.

The results of this work show that presented workflow, if correctly tuned, is flexible and effective in the creation of a digital model of metallic and ceramic open-cell foams, not only by generating a geometry that accurately capture the target values of the descriptors often used for the characterization of porous media, porosity, specific surface and tortuosity, but also from a topological and and morphological point of view of view. The first step of the workflow, namely the generation of the initial seeds of the Voronoi tessellation, is attained thanks to a versatile sphere aggregation process, unlike most of the other works found in literature [3, 25, 26, 28, 87, 88]. This aggregation process, is easily adjustable and leads to a great number of arrangements, characterized by different values of compactness and heterogeneity, which can lead to a foam geometry with similar properties. The second step leads to the creation of the foam final geometry starting from a *ball and sticks* skeleton, using a procedure that does not make hard assumption on the micro-structure itself, as in [20, 25], such as a predetermined surface function describing the axial and cross-sectional shapes of the struts or nodes of the foams, or their intersection. The realistic output shapes are owed to the intrinsic properties of the volume modifying morphological operations used.

The validation of the output geometries of the workflow is important because it allows the use of such procedure for the creation of new foam structures with a close resemblance and relationship to real foams. Thus, this workflow uses innovative tools to create accurate in-silico models for open-cell foams, making use of innovative tools for the creation of the cellular structure and for the modification of the foam morphology.

This is achieved at limited computational costs available in any regular laptop computer. Future perspectives on this topic are then to further improve the understanding of how the input parameters influence the output features by exploring a wider number of cases and especially by better discerning the geometrical peculiarities of each - beyond simple, and oft-used, descriptors like porosity or tortuosity. This could be also improved with linking the operating conditions used by manufactures to achieved foams with specific characteristics, with the sphere aggregation procedure at the beginning of the workflow. This investigation could lead to the formulation of input-output parameters correlations that would allow the optimization of the foam structure for different field of applications,e.g. filtration, catalysis or heat transfer.

Chapter 5

A Filtration Industrial Application

The focus of this chapter is on the the phenomena occurring during the filtration of ferrous particulate, transported by hydrocarbons stream, in granular beds and open-cell foams. Ferrous particulates are a common impurity carried by hydrocarbon streams in the refining industry, that can be detrimental, for instance, to the performance of catalytic hydro-treatment reactors. Indeed, this solid particulate, with particles size ranging between 5 and 20 µm, can act as a poison for the catalytic particles or plug up the reactor bed to the point the head losses are too high and the the reactor bed must be changed. Therefore the removal of such particles is an important pre-treatment step to carry out. Granular beds are a common configuration for a particulate filters in this kind of operations, since they are very efficient in particle removal. However, the pressure drops associated to such systems tends to increase exponentially with time, during filtration, due to the formation of a particulate cake at the inlet of the device. For this reason, it is interesting to investigate the filtration performances of ceramic open-cell foams, which may be efficient and at the same time reduce the head loss showed by granular bed configuration, as they allow more depth filtration allowing for longer operation time before maintenance. The open cellular structure of ceramic open-cell foams can be tortuous enough to have good performances as a filter and simultaneously reduce the total pressure drops due to the high porosity associated with these materials. The filtration process is modeled using CFD numerical simulations to solve the momentum equation for the continuum phase (the liquid hydrocarbon). Then, under the hypothesis of a dilute system, Lagrangian discrete particle model (DPM) simulations are used to calculate the trajectories of solid particulate. At first the simulations were carried

out using classic mono-disperse granular bed configuration, with spherical packed bed generated in-silico using the DEM software `Yade` [89], following a procedure proposed and validated by Marcato et al. [90]. The results of these simulations are compared with the model proposed by Yao et al. [1], for the filtration of solid particles carried along by a liquid continuum through granular bed system. The results showed a good agreement between the model and the CFD/DPM simulations in describing the particle capture phenomena, validating the model. Therefore, multiple simulations at different operating condition were carried out using ceramic open-cell foams geometries digitally reconstructed into three-dimensional models using images obtained from x-ray tomographic sampling (cf. section 2.3.4).

5.1 Operating conditions and numerical details

The system taken into exam for this investigation relies on simplifying hypothesis that can be assumed in light of the particular operating conditions taken into account:

- the flow regime is not turbulent, meaning that for a system such as a spherical packed bed or open-cell foams the Reynolds number $\mathrm{Re} \leq 150 - 200$ [40]. This is in accordance with the hypothesis of the filtration model used as reference;
- the solid particle load is such that the system can be considered in dilute conditions. This means that, despite the high density of the ferrous particles, they occupy a negligible volume with respect to the continuum phase;
- particle dimension is mono-dispersed and their average size ranges between 5 and 20 µm. These particles are big enough for the Brownian diffusion phenomenon of Eq. 2.19 to be negligible compared the other phenomena driving the deposition of the solid particle on the porous media matrix, i.e. gravitational deposition and steric interception;
- the attachment rate of the solid particles on the filters walls α_D, introduced in §2.2.3, is unitary, meaning that if a particle impacts on the filtering media walls it is instantly and irreversibly captured.

The previous hypotheses allow the use of one-way coupling model [49] between discrete particles and liquid hydrocarbon, implying that the solid particle have no

influence on the flow field, but are only transported themselves by the fluid, following the streamlines. Introducing the flow Stokes number St, defined as:

$$\mathrm{St} = \frac{\tau_0 V_0}{L_0} \tag{5.1}$$

with V_0 the superficial macroscopic velocity at long distance from the filter collector, equivalent to q. L_0 is the characteristic length of the solid collector and τ_0 is the relaxation time of the particle transported by the fluid. The latter is defined by Eq. 2.13.

This dimensionless number indicates the ratio between the characteristic time of a particle and the fluid in motion. High values of St indicates that particle have high inertia, and are typical of systems such as solid particles transported by gaseous stream. In this case, an abrupt change in direction of the fluid is not followed by the solid particles which have a longer characteristic time and thus continue travel along their own trajectories. Instead, if the value of St is low and smaller than unity, the particles are transported by the fluid and have lower inertia. In case of sudden changes in direction, most of the solid particulates follow the fluid along its streamlines. For the case in exam, the system fall within the conditions of the latter case, with $\mathrm{St} \ll 0.01$ in all the combinations of operating conditions explored. In light of the hypotheses listed above, the remaining driving deposition mechanisms, according to Eq. 2.22, are the interception and the gravitational deposition. However, it was verified, by comparing the values of the single collector η_I and η_G for each of the operating conditions simulated (cfr. §5.2 and Fig. 5.3), that for the collector geometries taken into account, the interception mechanisms is negligible compared to the gravitational one, $\eta_I \ll \eta_G$. Introducing the solid particle terminal velocity U_p, written as:

$$U_p = \frac{(\rho_p - \rho)\, g {d_p}^2}{18\mu} \tag{5.2}$$

Eq. 2.22 can be written in normalized form, as reported in by Olson and Martins [6]:

$$\eta_0 = \eta_G = \frac{U_p}{V_0 + U_p}. \tag{5.3}$$

This is the expression used for the analysis of the results of the simulations performed for this investigation.

5.1.1 Geometries and computational domain

For this work three different ceramic alumina (Al_2O_3) open-cell foams were employed, respectively with size 20, 40, and 60 PPI. In order to get a more rigorous description of the geometric parameters, the foam micro structure was obtained using the X-ray tomography technique. The method of reconstruction is analogous to the one described in section 2.3.4 and 4.1.2. Also the method for computing the tortuosity, i.e. the *graph-based tortuosity*, is the same introduced in section 4.1.2.

A synthesis of the properties the investigated foams is reported in Tab. 4.1. The characteristic dimensions reported are referred to the *cells*, *windows*, *struts*, respectively d_C, d_W, d_S, the hydraulic diameter $d_h = 4\varepsilon/S_V$ and the *Sauter* diameter $d_{3,2} = 6(1-\varepsilon)/S_V$. The latter indicates the diameter of an equivalent packing of spheres having the same porosity and specific surface. Finally, the granular bed geometry used for this study are generated by the DEM software `Yade`, using monodispersed spheres, enclosed in a computational box with lateral size equivalent to 15 unitary diameter spheres (where the box constitutes the bounding limits for the DEM packing simulations). The packing has a porosity $\varepsilon = 0.39$, specific surface $S_V = 3600\ \mathrm{m^2\,m^{-3}}$ and tortuosity $\tau = 1.35$. The geometry obtained is then isotropically scaled to obtain beds with grains diameter $D_g = \{1,2,4\}$ mm.

5.1.2 CFD and DPM simulations

The solution of the Eq.2.1 and Eq.2.2 to calculate the flow field inside the foams geometries is carried out using the finite-volume CFD numerical simulation software `Ansys Fluent 2021R2`, with computational grids generated using utilities available within the `OpenFOAM` software. After the flow field is solved, the solution of the particle trajectories across the foam sample is calculated. The meshing procedure and the flow field solution are carried out as already reported in sections 4.1.4 and 4.1.4.

The meshing results in computational grids with a number of cells raging between 5 to 7 millions, constituted mainly by hexahedral cells, ensuring good numerical

Foam label	Al_2O_320	Al_2O_340	Al_2O_360
PPI	20	40	60
ε (%)	75.9	75.7	81
S_V (m^2 / m^3)	852	1715	2100
τ (–)	1.2	1.17	1.45
Sample size (mm)	19.3	19.3	16.32
d_C (mm)	3.3	1.8	1
d_h (mm)	3.6	1.8	1.5
d_W (mm)	1.8	0.92	0.54
d_S (mm)	1.95	0.55	0.31
$d_{3,2}$ (mm)	1.7	0.85	0.56
Tomo X sampling (voxels/µm)	50	50	25.5

Table 5.1 The physical and macroscopic properties of the foam samples used in this work. For both the metallic NiCr foams the values of PPI, ε and S_V are reported as nominally declared by the manufacturer and as measured from the X-ray tomography images analysis. For the ceramic foams only the values obtained from the image analysis were available. The values of d_C, d_W and d_S represent the average value calculated from the sie distributions obtained by performing pore-network analysis using the `PoreSpy` software.

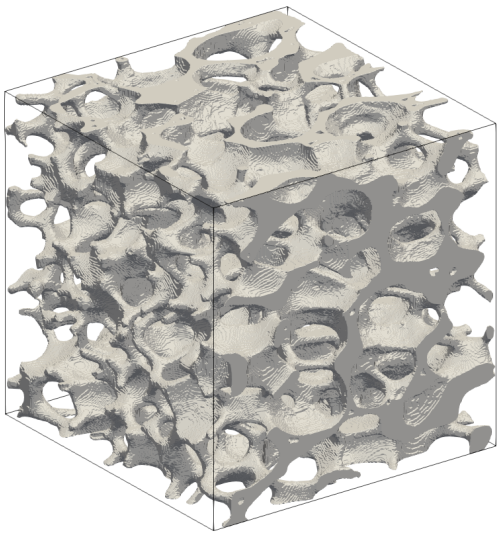

(a) $Al_2O_3$20PPI tomo

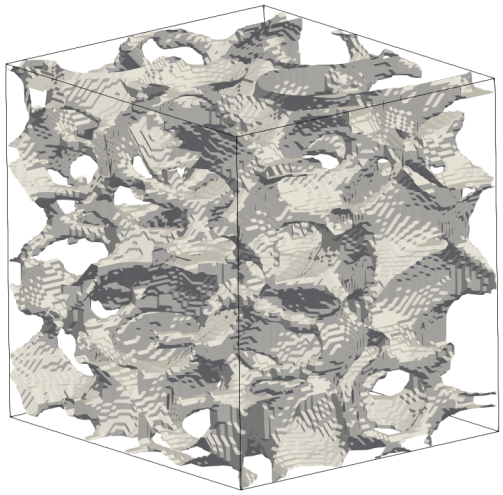

(b) $Al_2O_3$40PPI Tomo

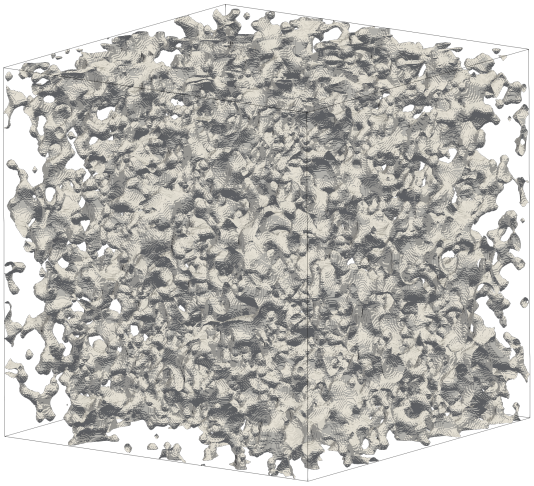

(c) $Al_2O_3$60PPI Tomo

Fig. 5.1 The ceramic foam geometries used for the present work: respectively $Al_2O_3$20 PPI, $Al_2O_3$40 PPI and $Al_2O_3$60 PPI. The images here reported are the result of the three-dimensional reconstruction of the foam structure using the procedure highlighted in section 2.3.4.

performance for the solver. The mesh is more refined closer to the solid walls, while moving farther away from the solid towards the bulk of the fluid, cells have increasing dimension. In accordance with what is reported by Loth [49], in its sistematic review of coupled Eulerian/Lagrangian simulation for one-way coupling systems, the mesh cell size is kept well above that of the discrete particle dimension in order to avoid numeric dependence of the Lagrangian particles trajectory solution. The flow field is initialized by setting the inlet velocity equal to the superficial macroscopic velocity V_0 on the inlet patch, a x-normal surface with coordinates $x_{inlet} = -L_x/2$. At the outlet, a surface with coordinates $x_{outlet} = L_x/2$, a relative pressure equal to 0 is specified. A *no-slip* condition for the velocity U is applied at the solid surface of the foam, whereas at the remaining sides of the domain a *symmetry* boundary condition is applied, implying no fluid motion across those. The specific dimension of each foam sample is reported in Tab.5.1. A schematic graphical representation of the computational domain is the same as reported in reported in Fig. 4.5. The Newtonian incompressible fluid here considered is n-heptane, with density ρ = 684 $\mathrm{kg\,m^{-3}}$, kinematic viscosity μ = 3.89 $\times$ 10^{-4} $\mathrm{kg\,m^{-1}\,s^{-1}}$. The system is solved using the `SIMPLE` algorithm, at a constant temperature $T = 293$ K (the energy equation was not solved) in steady-state condition. Gravity vector is collinear with the inlet velocity direction, that is normal to the inlet boundary surface, and its magnitude is 9.81 $\mathrm{m\,s^{-2}}$. The Reynolds number for this work is defined as $\mathrm{Re} = U \cdot d_h/\nu$. Specifically, the choice made in this definition is to use the hydraulic diameter (among all the otherwise defined diameters mentioned above) as the characteristic length in the definition of the Reynolds number. The flow is solved with a laminar viscous model for up to $Re \leq 150 \sim 200$. The inlet velocity values used for the simulations are $V_0 = \{0.16, 0.5, 1.6, 2.5, 5, 8, 10.5, 16, 50\}$ $\mathrm{mm\,s^{-1}}$.

Particles trajectories solution The calculation of the particle trajectories is carried out with the DPM model, present in `Ansys Fluent 2021 R2`. Solid particulate is hypothesized to be iron oxide, a common material entrained in refinery hydrocarbons and poisonous for a variety of catalysts, with density ρ_p = 5745 $\mathrm{kg\,m^{-3}}$. Four mono-dispersed classes of spherical particles are simulated, with diameter d_p = {5, 10, 15, 20} µm. The trajectories are calculated for each class of particle size, in four separate simulations, and for each value of inlet velocity V_0, with a total solid concentration of particles equal to 17 ppm, based on the liquid inlet mass flow-rate. This values are compatible with common operating conditions found in the refining

industry and fulfill the hypothesis of a dilute system. The trajectories are calculated in pseudo steady-state conditions solving Eq.2.12, subsequently and independently to the flow field equation, thanks to the one-way coupling assumption. An example of the solution obtained using the methods describe in this section is shown in Fig. 5.2.

5.2 Results analysis

The simulations carried out to obtain the following results were performed on the private calculation cluster `ENER440`, kindly made available by *IFP Energies nouvelles*, the industrial partner of this research. The cluster is composed by Intel `Skylake G-6140` processors with 2.3 GHz base frequency, each calculation node equipped with 2 processors composed by 18 cores and 96 GB of RAM. The simulations are performed in parallel mode on one calculation node, with an average wall-clock time per case (flow-field and trajectories solutions) of 120 minutes.

The results obtained from the CFD/DPM simulations are here compared with the filtration model in terms of global efficiency, that is expressed as $\eta_{glob} = 1 - C_z/C_0$, where C_0 is the inlet concentration and C_z is the outlet concentration at the boundaries of the computational domain. The single collector efficiency, expressed as in Eq. 5.3, is calculated from the operating conditions, that is particulate size d_p and superficial velocity V_0. This value is used to calculate the global efficiency from the integration of the concentration balance of a single spherical collector, written as:

$$\frac{\mathrm{d}C}{\mathrm{d}L} = -\frac{3}{2}\frac{(1-\varepsilon)}{d}\eta_0\alpha_D C \tag{5.4}$$

Fig. 5.3 shows the value of the ratio η_G/η_I, with $\eta_I = \frac{3}{2}\left(\frac{d_p}{D_g}\right)^2$ and D_g is the characteristic diameter of the porous media related to the deposition phenomenon. This ratio is calculated over the whole range of operating conditions of the simulations performed for this investigation. The value of the ratio remains in all cases well above unity, thus $\eta_G \gg \eta_I$.

This validates the assumption made in the previous section regarding the primary driving mechanism in the deposition of the solid particles. Thus, in Eq. 5.5 the only mechanism taken into account is gravitational deposition. Thus the integral form of the concentration balance over the whole computational domain is:

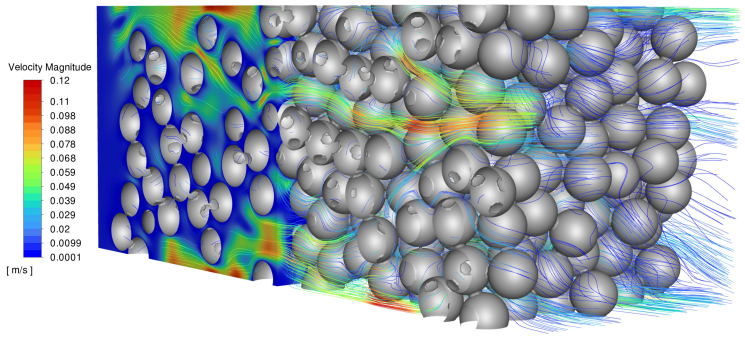

(a) Sphere packing 1 mm

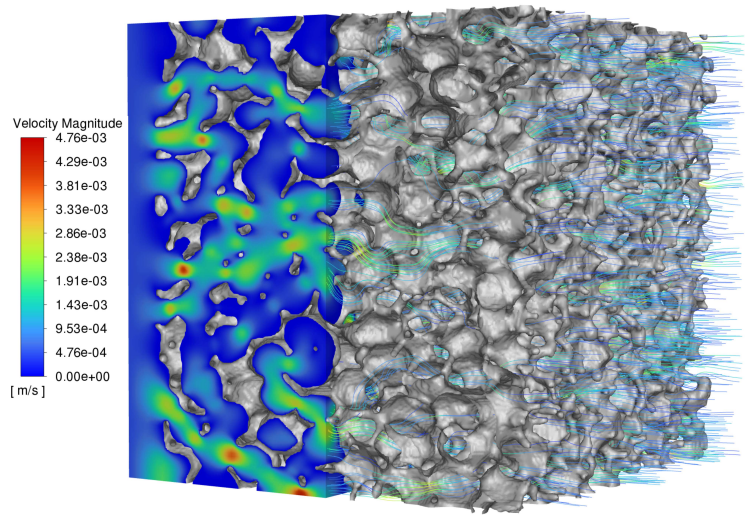

(b) Al_2O_340 PPI Tomography

Fig. 5.2 The image shows an example of the simulation results obtained with the methods detailed in this chapter. The first figure displays the particle trajectories on the granular bed configuration, $D_g = 1$ mm with $V_0 = 5$ mm/s and $d_p = 5$ µm. The second image analogously shows the trajectories results for the Al_2O_340 PPI foam, with $V_0 = 0.5$ mm/s and $d_p = 5$ µm

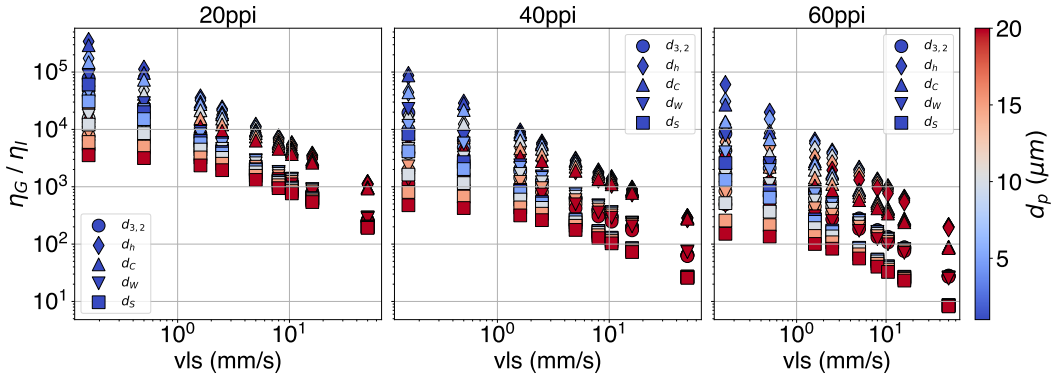

Fig. 5.3 The ratio between η_G and η_I is plotted for all the cases taken into account. Because the ratio remains well above unity, it is safe to assume that the only driving mechanism of particles deposition is the gravitational one.

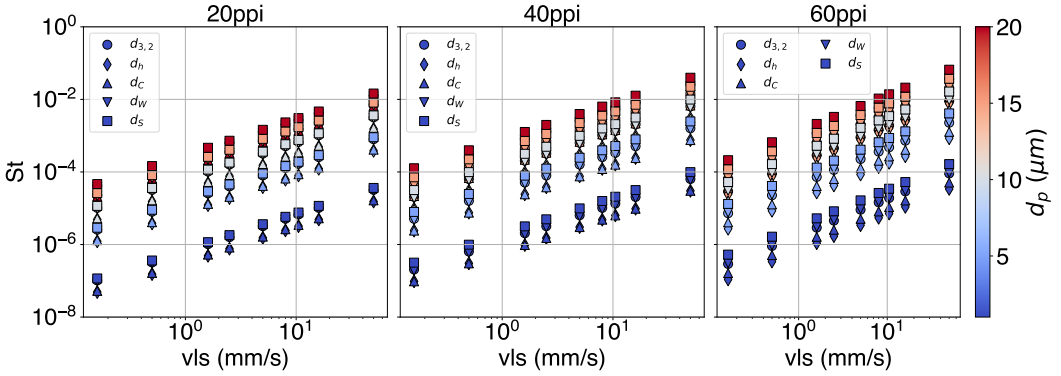

Fig. 5.4 The figure show the plot of the Stokes number St calculated for the solid particles for all the foam cases simulated. St is always well below unity, implying that the solid particles move transported by the fluid, following its streamlines and are deposed on the collectors wall because of the sole gravitational forces.

$$\ln \frac{C_z}{C_0} = -\frac{3}{2}(1-\varepsilon)\,\eta_G \frac{L}{d} \tag{5.5}$$

with unitary attachment rate α_D and single collector efficiency as in Eq. 5.3. L is the domain total length. The global efficiency is:

$$\eta_{glob} = 1 - \frac{C_z}{C_0} = 1 - \exp\left(-\frac{3}{2}(1-\varepsilon)\,\eta_G \frac{L}{d}\right) \tag{5.6}$$

It must be specified that this balance equation, as reported by Yao [1] and as later clarified by [53], was based on the solution of the flow field around a regular

arrangement of spherical collectors, as proposed by Levich [50] and Pfeffer [51]. The results obtained from the simulations performed in the random sphere packing system can be compared with high accuracy, even if the system has randomly disposed spheres, as attested by the numerous articles in literature [34, 35, 68]. In the case of the open-cell foams, this comparison is spurious since there is not a single constitutive entity that can be used, because of the particular morphology, where *struts*, *cells* and *windows* are all part of the same solid matrix. It is for this reason that the open-cell geometries are, for this work, characterized based on the hydraulic and *Sauter* diameters, defined in section 5.1.1, which refer to the diameter of spheres in a packing with equivalent properties to the foams. Therefore this comparison is nonetheless useful, since Eq. 5.6 contains information regarding the characteristic length associated to the deposition phenomena, in the form of the single collector diameter d.

Fig. 5.4 shows the Stokes number of the particles, cfr. Eq. 5.1. The values of St remains for all the cases taken into account well below 1, meaning that the particle tends to move in accordance to the streamlines of the fluid, separating only at close distance to the collectors walls, where they are captured at the surface because of the gravitational forces.

5.2.1 Filtration in random sphere packings

The results of the CFD simulations of the flow field coupled with Lagrangian DPM simulation show that the efficiency predicted by the computational model is in good agreement with the results obtained from the particle deposition model. The superficial velocities taken into account range between 0.16 and 50 mm/s, the particle size from 5 to 20 µm, the sphere packing considered have collectors of 1, 2 and 4 mm. The global deposition efficiency for all the cases is reported in Fig. 5.5. The Yao model prediction results in a single line, since the the L/d ratio in Eq. 5.6 remains constant at increasing spheres diameter, as explained in section 5.1.1 (due to the different geometries coming from isotropic scale-down procedures from the original packing created with `Yade`). . The larger solid particles are more efficiently captured by the granular bed with respect to the smallest ones, which approach the 1 µm limit, which according to Yao [1] is the dimension at which the single collector efficiency, and therefore the global one, are at its minimum. The grain size influence on η_{glob} is more pronounced for the smallest particles, whereas for higher

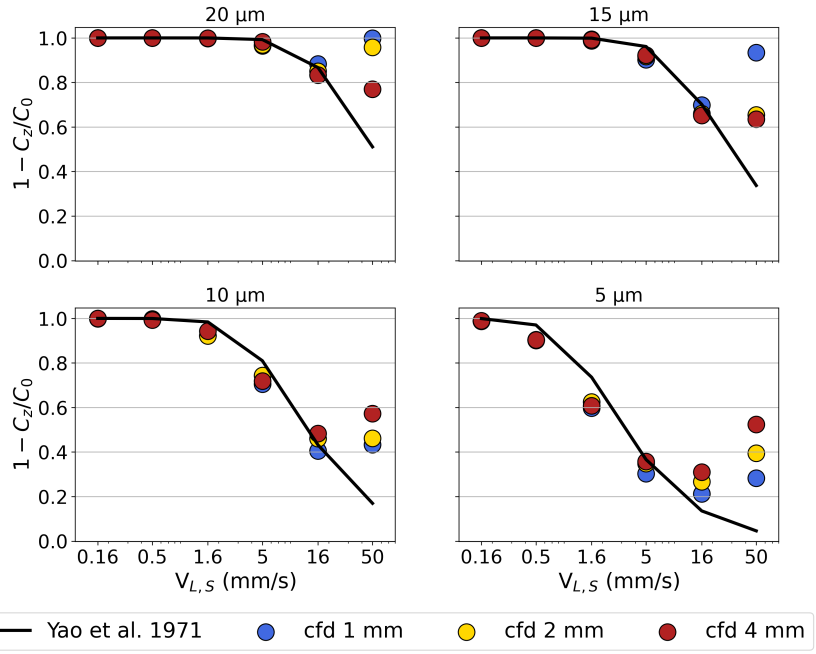

Fig. 5.5 The results of the CFD/DPM simulations campaign on the granular bed configuration are reported as colored circles: the blue, yellow and red represent respectively grain with size 1, 2 and 4 mm.The predictions obtained from the deposition model, the black line, are overlapped because in Eq. 5.6 the $\frac{L}{d}$ ratio remains constant.

particulate diameters this values are almost coincident. It is also important to stress how at higher values of superficial velocity V_0, the system has more instabilities as it approaches the turbulent regime, and for this reason the values of $1 - C_z/C_0$ are higher than those predicted by the model. This indicate that the hypothesis listed in section 5.1 does not hold true anymore in these cases with high superficial velocities, and as such these results should not be held in account.

5.2.2 Filtration in open-cell foams

Coupled CFD/DPM simulations were carried out on the three alumina open-cell foams object of this work, respectively Al_2O_320, Al_2O_340, Al_2O_360. Some additional inlet velocities V_0 are considered, with respect to the simulation on the granular bed configuration, as specified in section 5.1.2. Given the fact that there is not a unique characteristic length that can be used to described open-cell foams, the comparison with the particle deposition model must be carried out using multiple predictions with different assumptions. As a matter of fact, there is no evidence

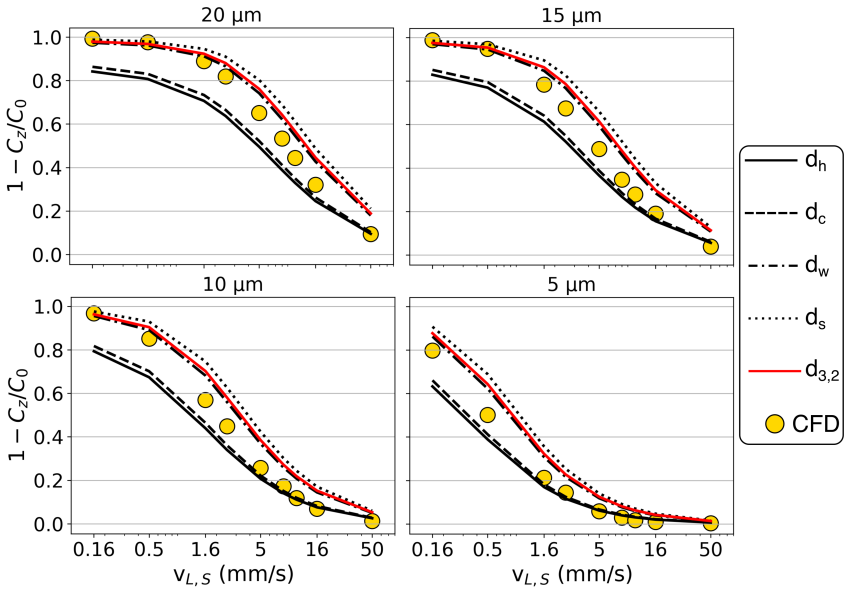

Fig. 5.6 The plot show the global efficiency η_{glob} calculated from CFD/DPM simulations for the $Al_2O_3$20 PPI foam, yellow circle, and the deposition model prediction calculated for single collector diameter equal to d_h, d_C, d_W, d_S, $d_{3,2}$, respectively.

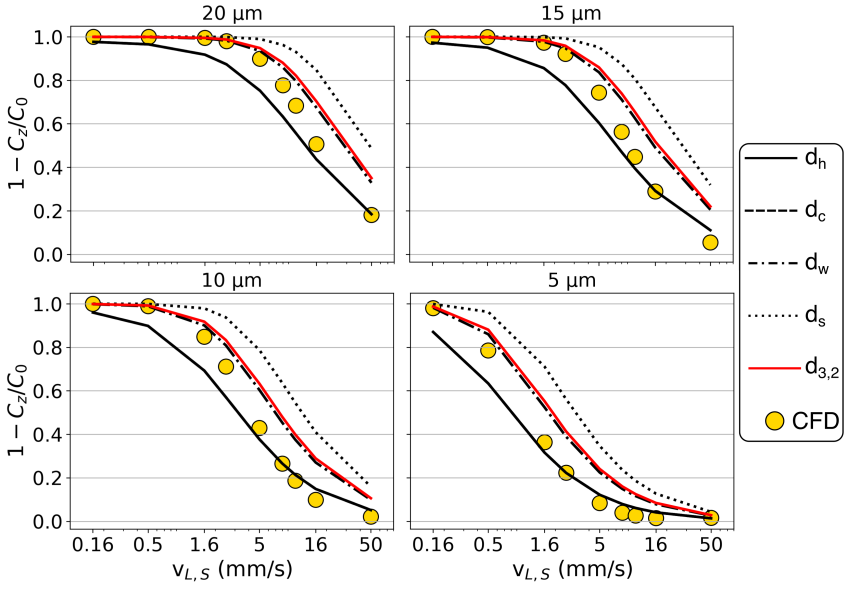

Fig. 5.7 The plot show the global efficiency η_{glob} calculated from CFD/DPM simulations for the $Al_2O_3$40 PPI foam, yellow circle, and the deposition model prediction calculated for single collector diameter equal to d_h, d_C, d_W, d_S, $d_{3,2}$, respectively.

about which of the three diameters describing the mean size of the geometric features (*struts*, *windows*, *cells*), or the equivalent diameters used (*hydraulic*, *Sauter*), is

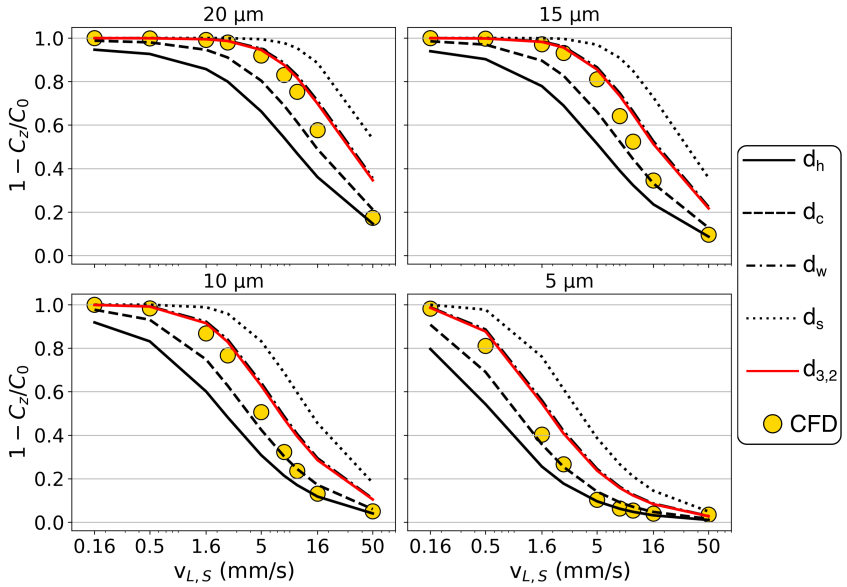

Fig. 5.8 The plot show the global efficiency η_{glob} calculated from CFD/DPM simulations for the Al_2O_360 PPI foam, yellow circle, and the deposition model prediction calculated for single collector diameter equal to d_h, d_C, d_W, d_S, $d_{3,2}$, respectively.

the most relevant to the description of the deposition phenomena at the micro-scale. In light of this, comparing the results of the simulations with the predictions given by the model using different definitions for the single collector diameters not only gives information regarding the validity of this modelling of the deposition phenomena, but could also provide important insights regarding the most descriptive characteristic length for these systems. Again, this information is important not only for a better understanding of the phenomenon, but is crucial for the design of industrial equipment. Fig. 5.8 summarizes the results obtained for the three foams in exam, showing the global efficiency η_{glob} as a function of the operating conditions, namely the inlet velocity and the particle size. It is evident how, despite the overall good performance of the CFD/DPM results in predicting the efficiency, none of the five characteristic lengths proposed can be used *alone* to describe the overall behaviour. None of the efficiencies obtained from the simulations deviate significantly from the different models predictions, approximately in a range of $\pm 20\%$ with respect to the different models lines, considering that between the smallest diameter, usually d_S or $d_{3,2}$, and the greatest, usually d_C or d_h, the ratio lies within 2 and 4. The analysis of the diagrams of Fig. 5.8 reveal that a common trend can be highlighted: the simulations results tends to be closer to the predictions based on the smallest characteristic lengths, $d_{3,2}$, d_W and d_S, when the velocity

are lower and/or the particles size is greater, $d_p \approx 15 - 20$ µm. On the contrary, if the velocity is higher or the particles are smaller, the simulations results tends to agree more with the theoretical results using from d_C or d_h. An attempt to find a unique correlation between the deposition efficiency, the operating conditions and the characteristic lengths was done, but it was ineffective: whereas $d_{3,2}$ and d_h are equivalent diameters and have not direct physical relationship with the geometric features of the open-cell foams, it is also true that only d_S refers to an actual foam structuring element, the average diameter of the struts (and in the literature ,the definition of this can change from author to author). Regarding d_C and d_W, indeed they have a physical relationship with the real geometry, however they describe the average size of *void* entities, referred to the different void features of the foams, the cells and the windows connecting them. Since the two equivalent diameters seems to be at the two limits of the deposition model prediction, an attempt to find functional correlation for the phenomenon containing these two parameters was made to obtain the characteristic length of the deposition phenomenon, written as:

$$d_{coll} = d_{3,2}{\eta_G}^a + (1 - {\eta_G}^a)\, d_h \tag{5.7}$$

where the exponent a is varied in order to minimize the global error, comparing the collector diameter obtained from Eq. 5.7 and the one obtained from Eq. 5.5. however the correlation error was always well above 30%. Another attempt was to describe the results through functional forms depending on the tortuosity, similarly to what was done for the results presented in chapter 3.2.2. However none of the attempts yielded correlations with acceptable errors. This outcome is similar to what already reported and concluded at the end of Chapter 3. The reasons reside in the complexity of the porous solid structure of the foams which, unlike granular beds of spheres, that can be described by the grains average size D_g, are characterized by multiples ones. In particular, the three characteristics length usually employed for the description of the foams, d_C, d_W and d_S, are related to geometric features very different between each other: d_S is an indication of the average solid ligaments size, whereas d_C, d_W are linked to the void fraction of the porous medium, representing respectively the characteristic lengths of the pores and of the channels connecting the latter.

5.3 Conclusions

In this part of the work ferrous particles deposition carried by liquid hydrocarbon flow in porous media was explored. The particles dimension taken into exam ranges between 5 and 20 μm, whereas the fluid velocity ranges between 0.5 and 50 mm/s. The fluid flow has been investigated using computational fluid dynamics (CFD) simulations, whereas the particles trajectories have been obtained with a Lagrangian discrete particles method (DPM) simulations. Different combinations of operating conditions are explored by varying the inlet superficial velocity V_0 and the discrete particle diameters d_p over a large range of values. The overall filtration efficiency has been calculated from results of the simulations and it has been compared to the prediction given by the deposition model firstly proposed by Yao et al.[1]. At first, the validity of the computational method has been tested using a granular bed configuration with mono-dispersed spheres, for three different grains sizes. These results show that the deposition phenomenon is well reproduced when the operating conditions remain within the limits of the model hypothesis, that is the system is dilute and the flow regime remains within the laminar limits. Afterwards, the simulation workflow has been used to explore the deposition phenomenon inside a different type of porous media: ceramic open-cell foams. Materials of this type are appreciated, between other characteristics, for theirs open cellular structure which, coupled with their medium-high tortuosity, can operate successfully as a solid particulate filter at reduced pressure drop compared to classical granular bed configurations. Three type of ceramic foam geometries have been used to carry out CFD/DPM simulations, respectively Alumina (Al_2O_3) 20, 40, 60 pores per inch, with the same operating conditions as for the granular bed configuration. The results are again compared with the deposition model predictions: since open-cell foams inherently have more than one characteristic length, the global efficiency of deposition is calculated for each of the describing diameters, namely d_h, d_C, d_W, d_S, $d_{3,2}$. This comparison shows that the CFD results are well within the limits of the model, with η_{glob}^{CFD} within the curves obtained from the deposition model varying the single collector diameter. In particular, the computational results are closer to the the predictions based on using the smallest diameters (d_W, d_S, $d_{3,2}$) when the solid particles are large and/or the velocity is lower, whereas at increasing fluid velocity and/or decreasing particle size, the efficiency tend to approach the higher describing diameters (d_h, d_C). Some attempts to investigate this behaviour have

been made, for instance by trying a power law functional form between η_{glob} as a function of d_h and $d_{3,2}$, representing the two limit behaviours. However, these attempts have been unsuccessful in finding a constitutive equation for the deposition phenomenon in open-cell foams as well as in determining which of the multiple describing characteristic length is the most important for the description of the filtration phenomena as well as for the design of the industrial equipment. Once again, as already reported in section 3.3, the results of this work highlight how the usual descriptors used to characterize a porous materials, some macroscopic, such as ε and τ, and some microscopic, such as the characteristic diameters, are not enough to thoroughly described clean bed particle filtration and further investigation are necessary. There may be several future perspectives on this topic: one is further exploring the deposition phenomena by using a wide number of geometries, produced by means of the workflow proposed in chapter 4, over a wide range of the macro and micro-descriptors values, in order to determine the influence on the deposition phenomenon and gain a full understanding of the system. Another interesting follow up will be to use the data obtained in this work to calculate the mass transfer dispersion coefficients of the solid particulate as well as the macroscopic pressure drops coefficient contained in the Darcy-Forchheimer equation, cfr. Eq. 2.8, to perform numerical simulation of a macroscopic filtration vessel packed with foam pellets and compare the results with a system packed with granular materials. This type of investigation will help to determine the range of parameters where the use of foam pellets is more beneficial in terms of energy consumption and process efficiency.

Chapter 6

Conclusions

In this manuscript, the modeling of open-cell foams using both computational and experimental methods is discussed, with particular focus in the field of filtration and particle deposition. These porous media has seen an increasing interest during the last twenty and more years, in particular in the field of the process industry, where they have been used in many different applications. Catalyst supports, heat exchanger packings and filtering media are but a few examples. The knowledge on the relevant parameters of more classical types of porous materials, such as granular beds packings, is vast and detailed, as testified by the huge amounts of scientific papers on the subject, from experimental to fully computational studies. This allowed an extensive use of these media in the process industry, allowing optimization of the equipment design and efficiency. In the case of ceramic and metallic foams, this knowledge and understanding is still very much empirical and limited to particular applications. This is, without a doubt, the result of the peculiar geometrical and morphological structure characterizing open-cell foams, and also due to the great heterogeneity with which these porous media are fabricated and labeled by the industrial manufacturers.

As already stated in the introduction of this manuscript, the most common "label" (meaning, a descriptive quantity) used for solid foams are the *pores per inch*, which gives an approximate estimation of the density of the solid matrix. However, the PPI parameter can not be directly used for the estimation of the design parameters commonly used by practitioners in the field of process engineering: the already mentioned porosity, specific surface and eventually tortuosity. On the other hand, it

is not an easy task to reduce the micro-scale geometrical descriptors of the foams, commonly identified in literature as the average diameters of the *cells*, *windows* and *struts*, to a single parameter, since they describe different feature of the geometry.

Granular beds are usually described by the dimensions of the packed spherical beads, if mono-disperse, or the average diameter if poly-disperse. In case of more *exotic* shapes, such as cylinders or trilobes, an equivalent diameter can be calculated, taking onto account the sphericity of the object. These diameters take into account the size of the obstacle the fluid encounters while flowing through the porous matrix. In open-cell foams, the solid obstacle is represented by the struts, whose diameter is related to the size of the ligaments of the solid matrix. However, while for highly porous foams ($\varepsilon \geq 0.85 - 0.9$), and especially metallic ones, this description is straightforward, since the structure is thin and struts and nodes are well defined, for lower porosity the structure is much more heterogeneous, ligaments and nodes are fused together and less defined. In these cases, particularly common for ceramic foams, the average strut diameter is an indication of the average solid matrix size, but can vary widely between the thinner part of the ligaments and the thick fused nodes. Similarly, the cell and windows diameters are characteristic lengths related to the void part of the structure, therefore not describing the obstacle but rather the open channels and volumes encountered by the fluid in its path.

These observations are here reported, as done throughout the whole manuscript, not to highlight the problems encountered when dealing with such complex materials, but rather to remark that, in alternative to reducing the description of the porous matrix to a single geometric parameter, a rational approach to the modeling of open-cell foams is the use of computational methods for the description of the porous structure, its digital replication and to investigate the transport phenomena occurring when a fluid flows through it for different application. Therefore, this manuscript report the different approaches, tools and strategies employed to achieve this aim.

A primary aim of this research is to propose a digital platform for modeling of the solid foams which is able to generate a wide range of geometries and carry out computational fluid dynamics simulations to investigate the flow field and the transport phenomena inside open-cell foams. This is the object of both Chapter 3 and Chapter 4, where two different methodologies for the generation of foam three-dimensional models are proposed, tested and validated. The first workflow is flexible and effective to explore a great number of different types of geometries by changing

the type of size distribution for the initial set of *seeds*, however the use of a simplified model for the description of the solid matrix can represent a limitation in the applicability. The second workflow, instead, was developed to overcome some of the limitations of the previous one, in several directions. First, it employs a novel method for the generation of the initial *seeds* of the tessellation which is fast and flexible in creating multiple configurations that can lead to different foams realizations. Then, it uses in an innovative fashion procedures and methods borrowed from the field of image processing. These techniques are, once again, fast and very effective in generating foam models that can replicate real foam samples at the macro-descriptors level, with a very small error. The very positive results of the validation presented in Chapter 4 show that this is achieved without making any strong assumptions on the foam geometry, but is the results of the generation process itself.

The other main purpose for this research work was to investigate the transport phenomena inside open-cell foams and what is the influence of the different macro (ε, S_V and τ) and micro (d_C, d_W, d_S) features characterizing this porous medium. This analysis is carried out using numerical CFD simulations that allows the exploration of a wide range of operating conditions and allows the acces to information on the fluid dynamics at the micro-scale level, otherwise very difficult and expensive to obtain by experimental methods. The focus is put on the mass transfer occurring at the wall surface of the foam in case of a fast wall reaction, phenomena that can take place during instantaneous catalytic reactions or during particle deposition in clean bed filtration. This topic is first addressed in Chapter 3, where the geometries generated in-silico are tested for the clean bed filtration of colloidal particles transported by Brownian mechanism, which is simulated by a scalar transported by the fluid. The four geometrical models tested show different values of the deposition efficiency, and that this value varies, as expected, with porosity and geometrical model. However, none of the strategies used to correlate this efficiency to the macroscopic foam parameters, ε, S_V and τ), or their functional power law forms, gave positive results. A more industrial-oriented application is investigated in Chapter 5, where the topic investigated is the deposition of microscopic ferrous particles transported by hydrocarbon streams. This system is common in the refinery industry, where these particles act as a poison for catalytic reactions, e.g. hydro-treatment reactions, and therefore must be separated. In this particular case, the deposition mechanism is driven by the gravitational force and therefore, to models this phenomena, Lagrangian simulations of the particles trajectories are coupled with CFD for the solution of the flow field.

This model is first tested for a granular bed configuration, to verify its validity, and then particle filtration is simulated using three foam geometry, digitally reconstructed from real ceramic foams samples. The analysis of the results is focused on verifying if one of the characteristic length of the foams (d_h, d_C, d_W, d_S, $d_{3,2}$) can be used to described and parameterize the filtration phenomenon. The results show that, as for the case in exam in Chapter 3, each of the aforementioned diameters has a different relationship with the deposition mechanisms, and therefore it is not possible to develop a unique correlation to assist the design of filtration equipment, and further investigations on the topic are required.

Future perspectives on this topic are multiple and all can have positive impact on the improvement in the use of open-cell foams in the field of process industry. An improvement in the understanding of the geometric structure of the foams and its influence on the transport phenomena could be achieved by using the workflow firstly proposed in Chapter 3 and significantly improved in Chapter 4. This tool is fast and effective in replicating the foams structure, as it has been shown, and could easily generate a large data-set of foam structures with different characteristics. This data-set can be used improve the knowledge on the geometry itself or the transport phenomena, by coupling CFD and artificial intelligence methods, a strategy that has already been successfully used for granular bed systems [68, 90]. This knowledge and these tools could be used, in a second moment, to optimize the structure of the foams for specific applications, once the main influencing factors are isolated. This procedure could be then used to improve the manufacturing process of solid foams. Finally, the experimental data obtained for the validation of the workflow of Chapter 4 and the results on filtration obtained from Chapter 3 and Chapter 5 can be used to develop a multi-scale model of a porous medium having the characterists of open-cell foams and be used to perform simulation of, for instance, a packed bed reactor, filled with pellets of foams and retrieve the macro-scale efficiency of filtration or reaction for an industrial scale reactor. The multi-scale approach could be used to compare the performance of different types of reactors packings, and the characteristics of the foam could be improved by using the results of the parametric analysis proposed before.

References

[1] Kuan-Mu Yao, Mohammad T Habibian, and Charles R O'Melia. Water and waste water filtration. concepts and applications. *Environmental science & technology*, 5(11):1105–1112, 1971.

[2] Chris H. Rycroft. VORO++: A three-dimensional Voronoi cell library in C++. *Chaos*, 19(4):1–14, 2009.

[3] Enrico Agostini, Gianluca Boccardo, and Daniele Marchisio. An open-source workflow for open-cell foams modelling: Geometry generation and cfd simulations for momentum and mass transport. *Chemical Engineering Science*, 255:117583, 2022.

[4] Martyn V. Twigg and James T. Richardson. Fundamentals and applications of structured ceramic foam catalysts. *Industrial and Engineering Chemistry Research*, 46(12):4166–4177, 2007.

[5] J. T. Richardson, D. Remue, and J. K. Hung. Properties of ceramic foam catalyst supports: Mass and heat transfer. *Applied Catalysis A: General*, 250(2):319–329, 2003.

[6] Rudolph A Olson III and Luiz CB Martins. Cellular ceramics in metal filtration. *Advanced Engineering Materials*, 7(4):187–192, 2005.

[7] Carmen W. Moncada Quintero, Giuliana Ercolino, and Stefania Specchia. Combined silicon carbide and zirconia open cell foams for the process intensification of catalytic methane combustion in lean conditions: Impact on heat and mass transfer. *Chemical Engineering Journal*, 429:132448, 2022.

[8] Carmen W Moncada Quintero, Giuliana Ercolino, and Stefania Specchia. Effect of the co3o4 load on the performance of pdo/co3o4/zro2 open cell foam catalysts for the lean combustion of methane: Kinetic and mass transfer regimes. *Catalysis Today*, 383:247–258, 2022.

[9] E. Meloni, M. Caldera, V. Palma, V. Pignatelli, and V. Gerardi. Soot abatement from biomass boilers by means of open-cell foams filters. *Renewable Energy*, 2019.

[10] Gregor D. Wehinger, Stan T. Kolaczkowski, Leonhard Schmalhorst, Didier Beton, and Lars Torkuhl. Modeling fixed-bed reactors from metal-foam pellets with detailed CFD. *Chemical Engineering Journal*, 373(May):709–719, 2019.

[11] A. August, J. Ettrich, M. Rölle, S. Schmid, M. Berghoff, M. Selzer, and B. Nestler. Prediction of heat conduction in open-cell foams via the diffuse interface representation of the phase-field method. *International Journal of Heat and Mass Transfer*, 84:800–808, 2015.

[12] Shweta Singh and Naresh Bhatnagar. A survey of fabrication and application of metallic foams (1925–2017). *Journal of Porous Materials*, 25(2):537–554, 2018.

[13] William Thomson et al. On the division of space with minimum partitional area. *Acta mathematica*, 11:121–134, 1887.

[14] Roy M. Sullivan, Louis J. Ghosn, and Bradley A. Lerch. A general tetrakaidecahedron model for open-celled foams. *International Journal of Solids and Structures*, 2008.

[15] G. Incera Garrido, F. C. Patcas, S. Lang, and B. Kraushaar-Czarnetzki. Mass transfer and pressure drop in ceramic foams: A description for different pore sizes and porosities. *Chemical Engineering Science*, 63(21):5202–5217, 2008.

[16] Amer Inayat, Hannsjörg Freund, Andreas Schwab, Thomas Zeiser, and Wilhelm Schwieger. Predicting the specific surface area and pressure drop of reticulated ceramic foams used as catalyst support. *Advanced Engineering Materials*, 13(11):990–995, 2011.

[17] Amer Inayat, Jan Schwerdtfeger, Hannsjörg Freund, Carolin Körner, Robert F. Singer, and Wilhelm Schwieger. Periodic open-cell foams: Pressure drop measurements and modeling of an ideal tetrakaidecahedra packing. *Chemical Engineering Science*, 66(12):2758–2763, 2011.

[18] Amer Inayat, Hannsjörg Freund, Thomas Zeiser, and Wilhelm Schwieger. Determining the specific surface area of ceramic foams: The tetrakaidecahedra model revisited. *Chemical Engineering Science*, 66(6):1179–1188, 2011.

[19] Prashant Kumar and Frederic Topin. The geometric and thermohydraulic characterization of ceramic foams: An analytical approach. *Acta Materialia*, 75:273–286, 2014.

[20] Matteo Ambrosetti, Mauro Bracconi, Gianpiero Groppi, and Enrico Tronconi. Analytical Geometrical Model of Open Cell Foams with Detailed Description of Strut-Node Intersection. *Chemie-Ingenieur-Technik*, 89(7):915–925, 2017.

[21] A. Della Torre, F. Lucci, G. Montenegro, A. Onorati, P. Dimopoulos Eggenschwiler, E. Tronconi, and G. Groppi. CFD modeling of catalytic reactions in open-cell foam substrates. *Computers and Chemical Engineering*, 92:55–63, 2016.

[22] C. Lautensack, M. Giertzsch, M. Godehardt, and K. Schladitz. Modelling a ceramic foam using locally adaptable morphology. *Journal of Microscopy*, 230(3):396–404, 2008.

[23] Claudia Redenbach. Microstructure models for cellular materials. *Computational Materials Science*, 2009.

[24] T. Wejrzanowski, J. Skibinski, J. Szumbarski, and K. J. Kurzydlowski. Structure of foams modeled by Laguerre-Voronoi tessellations. *Computational Materials Science*, 67(November 2017):216–221, 2013.

[25] Mauro Bracconi, Matteo Ambrosetti, Matteo Maestri, Gianpiero Groppi, and Enrico Tronconi. A systematic procedure for the virtual reconstruction of open-cell foams. *Chemical Engineering Journal*, 315:608–620, 2017.

[26] Zhengwei Nie, Yuyi Lin, and Qingbin Tong. Modeling structures of open cell foams. *Computational Materials Science*, 131:160–169, 2017.

[27] Zhengwei Nie, Yuyi Lin, and Qingbin Tong. Numerical investigation of pressure drop and heat transfer through open cell foams with 3D Laguerre-Voronoi model. *International Journal of Heat and Mass Transfer*, 113:819–839, 2017.

[28] Saurish Das, S. Sneijders, N. G. Deen, and J. A.M. Kuipers. Drag and heat transfer closures for realistic numerically generated random open-cell solid foams using an immersed boundary method. *Chemical Engineering Science*, 183:260–274, 2018.

[29] Christoph Kloss, Christoph Goniva, Alice Hager, Stefan Amberger, and Stefan Pirker. Models, algorithms and validation for opensource dem and cfd-dem. *Progress in Computational Fluid Dynamics*, 12:140 – 152, 06 2012.

[30] A. P. Thompson, H. M. Aktulga, R. Berger, D. S. Bolintineanu, W. M. Brown, P. S. Crozier, P. J. in 't Veld, A. Kohlmeyer, S. G. Moore, T. D. Nguyen, R. Shan, M. J. Stevens, J. Tranchida, C. Trott, and S. J. Plimpton. LAMMPS - a flexible simulation tool for particle-based materials modeling at the atomic, meso, and continuum scales. *Comp. Phys. Comm.*, 271:108171, 2022.

[31] Kenneth A. Brakke. The surface evolver. *Experiment. Math.*, 1(2):141–165, 1992.

[32] Gianluca Boccardo, Daniele L. Marchisio, and Rajandrea Sethi. Microscale simulation of particle deposition in porous media. *Journal of Colloid and Interface Science*, 417:227–237, 2014.

[33] Matteo Icardi, Gianluca Boccardo, Daniele L. Marchisio, Tiziana Tosco, and Rajandrea Sethi. Pore-scale simulation of fuid flow and solute dispersion in three-dimensiona porous media. *Engineering Sciences and Fundamentals 2014 - Core Programming Area at the 2014 AIChE Annual Meeting*, 2:725, 2014.

[34] Gianluca Boccardo, Frédéric Augier, Yacine Haroun, Daniel Ferré, and Daniele L. Marchisio. Validation of a novel open-source work-flow for the simulation of packed-bed reactors. *Chemical Engineering Journal*, 279:809–820–820, 2015.

[35] Gianluca Boccardo, Eleonora Crevacore, Rajandrea Sethi, and Matteo Icardi. A robust upscaling of the effective particle deposition rate in porous media. *Journal of Contaminant Hydrology*, 212(February):3–13, 2018.

[36] Shankar Krishnan, Jayathi Y. Murthy, and Suresh V. Garimella. Direct Simulation of Transport in Open-Cell Metal Foam. *Journal of Heat Transfer*, 128(8):793, 2006.

[37] Francesco Lucci, Augusto Della Torre, Jan von Rickenbach, Gianluca Montenegro, Dimos Poulikakos, and Panayotis Dimopoulos Eggenschwiler. Performance of randomized Kelvin cell structures as catalytic substrates: Mass-transfer based analysis. *Chemical Engineering Science*, 112:143–151, 2014.

[38] Francesco Lucci, Augusto Della Torre, Gianluca Montenegro, and Panayotis Dimopoulos Eggenschwiler. On the catalytic performance of open cell structures versus honeycombs. *Chemical Engineering Journal*, 264:514–521, 2015.

[39] Francesco Lucci, Augusto Della Torre, Gianluca Montenegro, Rolf Kaufmann, and Panayotis Dimopoulos Eggenschwiler. Comparison of geometrical, momentum and mass transfer characteristics of real foams to Kelvin cell lattices for catalyst applications. *International Journal of Heat and Mass Transfer*, 108:341–350, may 2017.

[40] A. Della Torre, G. Montenegro, G. R. Tabor, and M. L. Wears. CFD characterization of flow regimes inside open cell foam substrates. *International Journal of Heat and Fluid Flow*, 50:72–82, 2014.

[41] Saurish Das, Niels G. Deen, and J. A.M. Kuipers. Direct numerical simulation for flow and heat transfer through random open-cell solid foams: Development of an IBM based CFD model. *Catalysis Today*, 273:140–150, 2016.

[42] Saurish Das, Niels G. Deen, and J. A.M. Kuipers. Immersed boundary method (IBM) based direct numerical simulation of open-cell solid foams: Hydrodynamics. *AIChE Journal*, 63(3):1152–1173, 2017.

[43] V. Chandra, S. Das, E. A.J.F. Peters, and J. A.M. Kuipers. Direct numerical simulation of hydrodynamic dispersion in open-cell solid foams. *Chemical Engineering Journal*, 358(2019):1305–1323, 2019.

[44] Stephen Whitaker. *The method of volume averaging*, volume 13. Springer Science & Business Media, 2013.

[45] Henry Darcy. *Les fontaines publiques de la ville de Dijon: Exposition et application des principes à suivre et des formules à employer dans les questions de distribution d'eau: Ouvrage terminé par un appendice relatif aux fournitures*

d'eau de plusieurs villes, au filtrage des eaux et à la fabrication des tuyaux de fonte, de plomb, de tôle et de bitume, volume 2. V. Dalmont, 1856.

[46] Jacob Bear. *Dynamics of fluids in porous media*. Courier Corporation, 1988.

[47] Albert Einstein et al. On the motion of small particles suspended in liquids at rest required by the molecular-kinetic theory of heat. *Annalen der physik*, 17(549-560):208, 1905.

[48] Ansys Corp. Ansys fluent 2021r2. *Theory Guide*, 2021.

[49] E. Loth. Numerical approaches for motion of dispersed particles, droplets and bubbles. *Progress in Energy and Combustion Science*, 26(3):161–223, 2000.

[50] Veniamin Grigorevich Levich. *Physicochemical hydrodynamics*. Prentice-Hall Inc., 1962.

[51] Robert Pfeffer and John Happel. An analytical study of heat and mass transfer in multiparticle systems at low reynolds numbers. *AIChE Journal*, 10(5):605–611, 1964.

[52] Rajamani Rajagopalan and Chi Tien. Trajectory analysis of deep-bed filtration with the sphere-in-cell porous media model. *AIChE Journal*, 22(3):523–533, 1976.

[53] Bruce E Logan, DG Jewett, Robert G Arnold, EJ Bouwer, and CR O'Melia. Clarification of clean-bed filtration models. *Journal of environmental engineering*, 121(12):869–873, 1995.

[54] Nathalie Tufenkji and Menachem Elimelech. Correlation equation for predicting single-collector efficiency in physicochemical filtration in saturated porous media. *Environmental science & technology*, 38(2):529–536, 2004.

[55] Simon L Goren and Michael E O'Neill. On the hydrodynamic resistance to a particle of a dilute suspension when in the neighbourhood of a large obstacle. *Chemical Engineering Science*, 26(3):325–338, 1971.

[56] John Happel. Viscous flow in multiparticle systems: slow motion of fluids relative to beds of spherical particles. *AIChE journal*, 4(2):197–201, 1958.

[57] Athanasios G Konstandopoulos, Margaritis Kostoglou, Evangelos Skaperdas, Eleni Papaioannou, Dimitrios Zarvalis, and Evdoxia Kladopoulou. Fundamental studies of diesel particulate filters: transient loading, regeneration and aging. *SAE transactions*, pages 683–705, 2000.

[58] Sinzi Kuwabara. The forces experienced by randomly distributed parallel circular cylinders or spheres in a viscous flow at small reynolds numbers. *Journal of the physical society of Japan*, 14(4):527–532, 1959.

[59] F. Aurenhammer. Power diagrams: properties, algorithms and. *SIAM J. COMPUT.*, 16(1):78–96, 1987.

[60] Wendell Smith. Tess: A 3D cell-based Voronoi Python library based on voro++, June 2019.

[61] Jeffrey Gostik. Add an 'edges' attribute to Voronoi objects? #7103, March 2017.

[62] Maxime Moreaud, Giulia Ferri, Severine Humbert, Mathieu Digne, and Jean-Marc Schweitzer. Simulation of large aggregate particles system with a new morphological model. *Image Analysis & Stereology*, 40(2):71–84, 2021.

[63] Nobuyuki Otsu. A threshold selection method from gray-level histograms. *IEEE Transactions on Systems, Man, and Cybernetics*, 9(1):62–66, 1979.

[64] William E Lorensen and Harvey E Cline. Marching cubes: A high resolution 3d surface construction algorithm. *ACM siggraph computer graphics*, 21(4):163–169, 1987.

[65] Jean Serra. *Image Analysis and Mathematical Morphology: Vol.: 2: Theoretical Advances*. Academic Press, 1988.

[66] Samir Bensaid, Daniele L. Marchisio, and Debora Fino. Numerical simulation of soot filtration and combustion within diesel particulate filters. *Chemical Engineering Science*, 65(1):357–363, 2010.

[67] Tiziana Tosco, Julian Bosch, Rainer U Meckenstock, and Rajandrea Sethi. Transport of ferrihydrite nanoparticles in saturated porous media: role of ionic strength and flow rate. *Environmental science & technology*, 46(7):4008–4015, 2012.

[68] Agnese Marcato, Gianluca Boccardo, and Daniele Marchisio. A computational workflow to study particle transport and filtration in porous media: Coupling cfd and deep learning. *Chemical Engineering Journal*, 417:128936, 2021.

[69] E Crevacore, G Boccardo, D Marchisio, and Rajandrea Sethi. Microscale colloidal transport simulations for groundwater remediation. *Chemical Engineering Transactions*, 47:271–276, 2016.

[70] A. Koponen, M. Kataja, and J. Timonen. Tortuous flow in porous media. *Phys. Rev. E*, 54:406–410, Jul 1996.

[71] Artur Duda, Zbigniew Koza, and Maciej Matyka. Hydraulic tortuosity in arbitrary porous media flow. *Phys. Rev. E*, 84:036319, Sep 2011.

[72] Huilian Ma and William P Johnson. Colloid retention in porous media of various porosities: Predictions by the hemispheres-in-cell model. *Langmuir*, 26(3):1680–1687, 2010.

[73] Federico Municchi and Matteo Icardi. Macroscopic models for filtration and heterogeneous reactions in porous media. *Advances in Water Resources*, 141:103605, 2020.

[74] Nobuyuki Otsu. A threshold selection method from gray-level histograms. *IEEE Transactions on Systems, Man, and Cybernetics*, 9(1):62–66, 1979.

[75] Jeff T. Gostick, Zohaib A. Khan, Thomas G. Tranter, Matthew D.r. Kok, Mehrez Agnaou, Mohammadamin Sadeghi, and Rhodri Jervis. Porespy: A python toolkit for quantitative analysis of porous media images. *Journal of Open Source Software*, 4(37):1296, 2019.

[76] James Ahrens, Berk Geveci, and Charles Law. Paraview: An end-user tool for large data visualization. *The visualization handbook*, 717(8), 2005.

[77] Maxime Moreaud and François Cokelaer. Flowing bilateral filter: Definition and implementations. *Image Analysis & Stereology*, 34(2):101–110, 2015.

[78] Yehuda Bachmat and Jacob Bear. On the concept and size of a representative elementary volume (rev). In *Advances in transport phenomena in porous media*, pages 3–20. Springer, 1987.

[79] Jeff T Gostick. Versatile and efficient pore network extraction method using marker-based watershed segmentation. *Physical Review E*, 96(2):023307, 2017.

[80] Johan Chaniot, Maxime Moreaud, Loïc Sorbier, Thierry Fournel, and Jean-Marie Becker. Tortuosimetric operator for complex porous media characterization. *Image Analysis & Stereology*, 38(1):25–41, 2019.

[81] Adam Hammoumi, Maxime Moreaud, Elsa Jolimaitre, Thibaud Chevalier, Alexey Novikov, and Michaela Klotz. Graph-based m-tortuosity estimation. In Joakim Lindblad, Filip Malmberg, and Nataša Sladoje, editors, *Discrete Geometry and Mathematical Morphology*, pages 416–428, Cham, 2021. Springer International Publishing.

[82] Maxime Moreaud. IFPEN provides its internal signal and image processing platform for those who want the most advanced features combined with a simple and understandable user interface., 2021.

[83] Ansys Corp. Ansys fluent 2020r2. *User Guide*, 2020.

[84] Thien Nguyen, Stephen King, and Yassin Hassan. Experimental investigation of turbulent characteristics in pore-scale regions of porous media. *Experiments in Fluids*, 62(4):1–27, 2021.

[85] Amer Inayat, Michael Klumpp, Markus Lämmermann, Hannsjörg Freund, and Wilhelm Schwieger. Development of a new pressure drop correlation for open-cell foams based completely on theoretical grounds: Taking into account strut shape and geometric tortuosity. *Chemical Engineering Journal*, 287:704–719, 2016.

[86] Mauro Bracconi, Matteo Ambrosetti, Obinna Okafor, Victor Sans, Xun Zhang, Xiaoxia Ou, Claudio Pereira Da Fonte, Xiaolei Fan, Matteo Maestri, Gianpiero Groppi, et al. Investigation of pressure drop in 3d replicated open-cell

foams: Coupling cfd with experimental data on additively manufactured foams. *Chemical Engineering Journal*, 377:120123, 2019.

[87] Gregor D. Wehinger, Helge Heitmann, and Matthias Kraume. An artificial structure modeler for 3D CFD simulations of catalytic foams. *Chemical Engineering Journal*, 284:543–556, 2016.

[88] Sir W I L L I A M TtIOMSON. 1888.

[89] V Smilauer, E Catalano, B Chareyre, S Dorofeenko, J Duriez, A Gladky, J Kozicki, C Modenese, L Scholtes, L Sibille, et al. Yade documentation. the yade project, 2014.

[90] Agnese Marcato, Gianluca Boccardo, and Daniele Marchisio. From computational fluid dynamics to structure interpretation via neural networks: An application to flow and transport in porous media. *Industrial & Engineering Chemistry Research*, 61(24):8530–8541, 2022.

Appendix A

Supporting Information to Chapter 3

A.1 Technical details: hardware and computational costs

A.1.1 Hardware information

Both the pre-processing (meshing) and the flow and transport simulations were performed on the following systems:

- Fujitsu Workstation: CPU with 2×12 cores Intel Xeon Gold 5118 at 2.30 GHz.
- HPC@Polito Legion Cluster: CPU 2x Intel Xeon Gold 6130 at 2.10 GHz 16 cores
- CINECA Galileo Cluster: 2 x 18-cores Intel Xeon E5-2697 v4 at 2.30 GHz

A.1.2 Computational costs

Fujitsu Workstation: (2×12 cores Intel Xeon Gold 5118 at 2.30 GHz)

Random sphere packing

The process of packing around 6000 spheres in a box of side equal to 15 Blender units (i.e. 15 mean sphere diameters) with `BSand` takes 5913 seconds in a single-core configuration.

Voronoi tesselations

The tessellation algorithm for the REV portion of the packing takes about 5 seconds in single-core configuration.

Foam model creation

The foam model creation with `Blender`, using cylinders as edges and sphere at the nodes, for an average of 3500 edges and 1800 nodes takes around 30 seconds in single-core configuration.

Meshing

The meshing procedure for a REV with 4 equivalent pore diameters length per side resulted on average in about $7 \cdot 10^6$ cells and the process take 3500 seconds to complete in single-core configuration .

Fluid flow simulations

The momentum transport simulations using the solver `simpleFoam` in parallel, using 4 cores (with domain decomposition method *Scotch*, takes 3 hours.

Scalar transport simulations

The scalar transport simulations using the solver `scalarTransportFoam` in parallel, using 4 cores (with domain decomposition method *Scotch*, takes 45 minutes.

A.2 Colloidal particle deposition: results overview

The results of particle deposition simulations can be reported in a plot representing the dependence of the Damköhler number Da with respect to the Péclet number Pe, reported in Figure A.1.

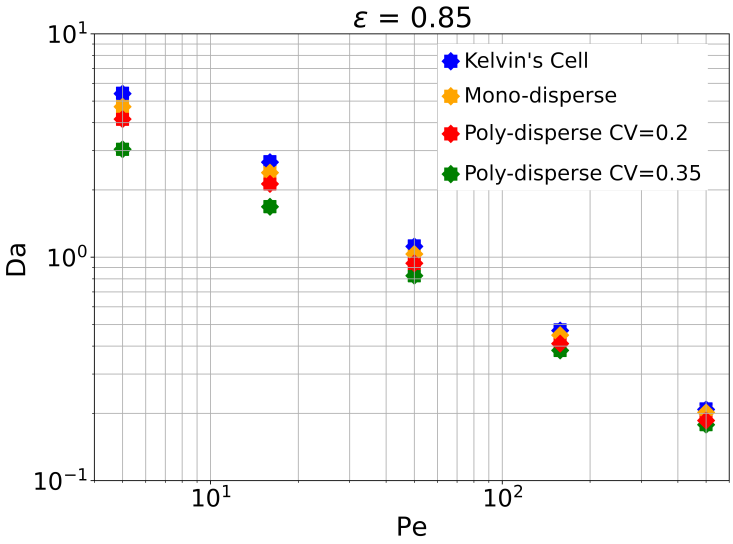

Fig. A.1 Da vs Pe at porosity $\varepsilon = 85\%$.

In order to research a possible correlation between between the results data-series for different geometric models, it has been decided to investigate the difference between the random models, which have more input parameters, with respect to the ideal , i.e. the Kelvins's Cell. Da values of the `KC` serie divided by each of the `mono`, `poly02` and `poly035` series respectively, obtaining a new coefficient, named C_{KC}. The results of this operation are reported in Figure A.2, where the KC factor is compared between the three random models derived from Voronoi tessellations.

In particular the values of the poly-disperse foam with highest coefficient of variation, $CV = 0.35$ is further from unity than the other results sets. Thus, the decision was made to work mainly on this set of data and in particular to investigate the trend at varying porosity ε. Figure A.3 show the values of C_{KC} for the `poly035` data at different porosity values. It can be noticed that the higher the porosity the closest the values of the KC factor to the unity, i.e. the closest to the ideal model. The scatter plots (this and subsequent Figures) also feature a trend line, representing the power law least square fitting of the data. The global error $E_{r,glob}$ of the fitting is

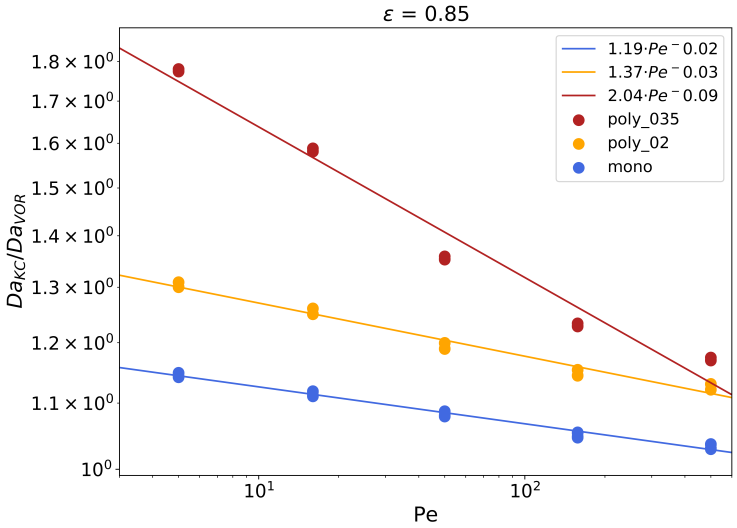

Fig. A.2 C_{KC} for `mono`, `poly02`, `poly035` series at porosity $\varepsilon = 85\%$.

calculated as the sum of the fitting error at each value of Pe. The general idea of this analysis was to normalize the C_{KC} by a combination of parameters, such as ε, S_V or τ, and to find the correlation which minimized the global error.

A.2.1 Results analysis: Dimensionless coefficients

The first approach taken in consideration was to subdivide C_{KC} by dimensionless groups derived from the main parameters, namely porosity ε, permeability k, mean pore diameter d_p and the specific surface $S_{V,bulk}$, which is calculated with respect to the bulk volume, i.e. the sum of the solid and liquid volumes. The following groups were obtained:

$$f_1 = S_{V,bulk} \cdot d_p \tag{A.1}$$

$$f_2 = \frac{k \cdot S_{V,bulk}}{d_p} \tag{A.2}$$

$$f_3 = \frac{k}{S_{V,bulk} \cdot d_p^3} \tag{A.3}$$

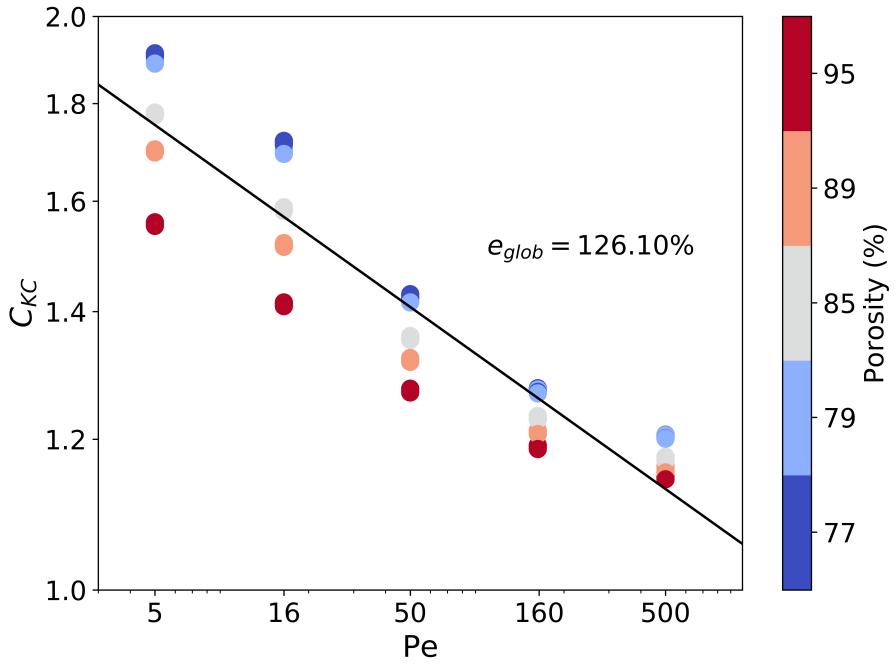

Fig. A.3 C_{KC} for the `poly035` set

The results, reported in Figure A.4, show that none of these dimensionless quantities is able to give a good interpretation of the results of the simulations, yielding global errors which are greater than that of the C_{KC} alone.

A.2.2 Results analysis: analytical principle correlations

The second approach adopted was to interpret the data according to first principle, analytical correlations developed in the field of colloid filtration for the fluid flow across solid collectors. In particular, the *Kuwabara* correlation, reported in Eq.(A.4), was developed for flow across cylindrical collectors, whereas the *Happel* correlation, reported in Eq.(A.5), relates to fluid flowing across spherical obstacles.

$$g(\varepsilon) = \frac{\varepsilon}{2-\varepsilon-\frac{9}{5}(1-\varepsilon)^{\frac{1}{3}}-\frac{1}{5}(1-\varepsilon)^2} \tag{A.4}$$

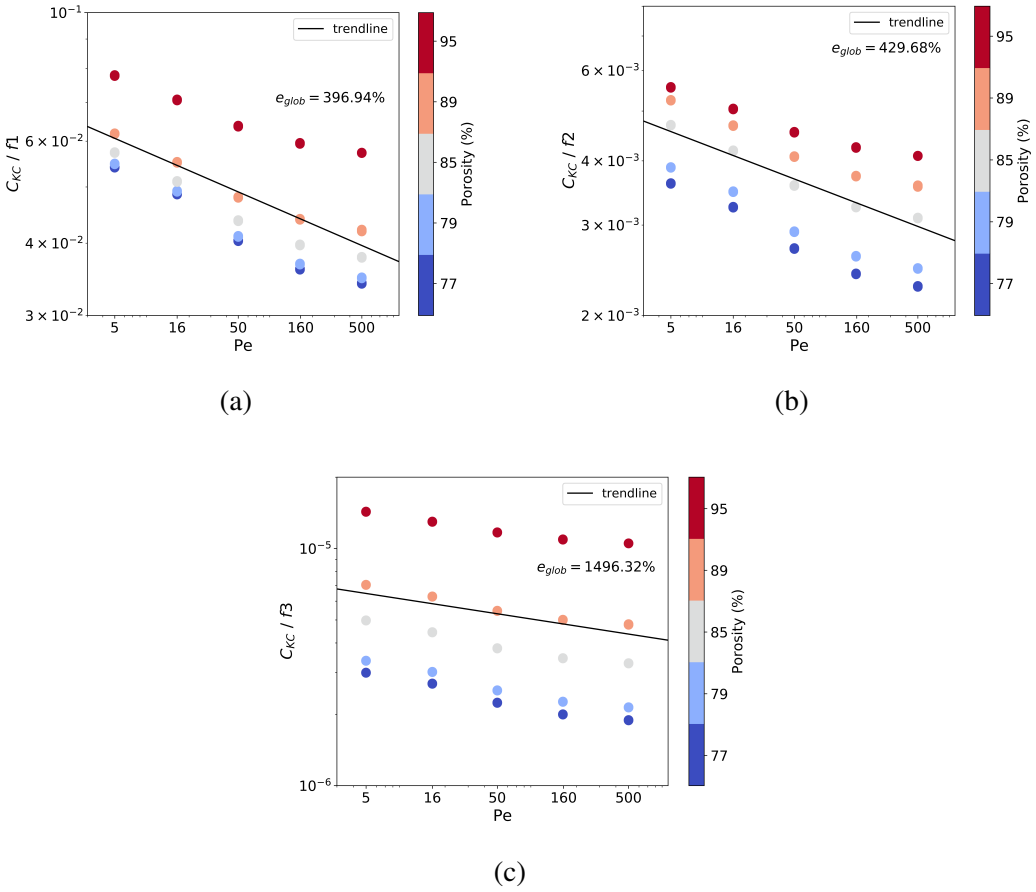

Fig. A.4 The dimensionless groups derived by dividing C_{KC} by Eq.(A.1) in (a), Eq.(A.2) in (b) and Eq.(A.3) in (c)

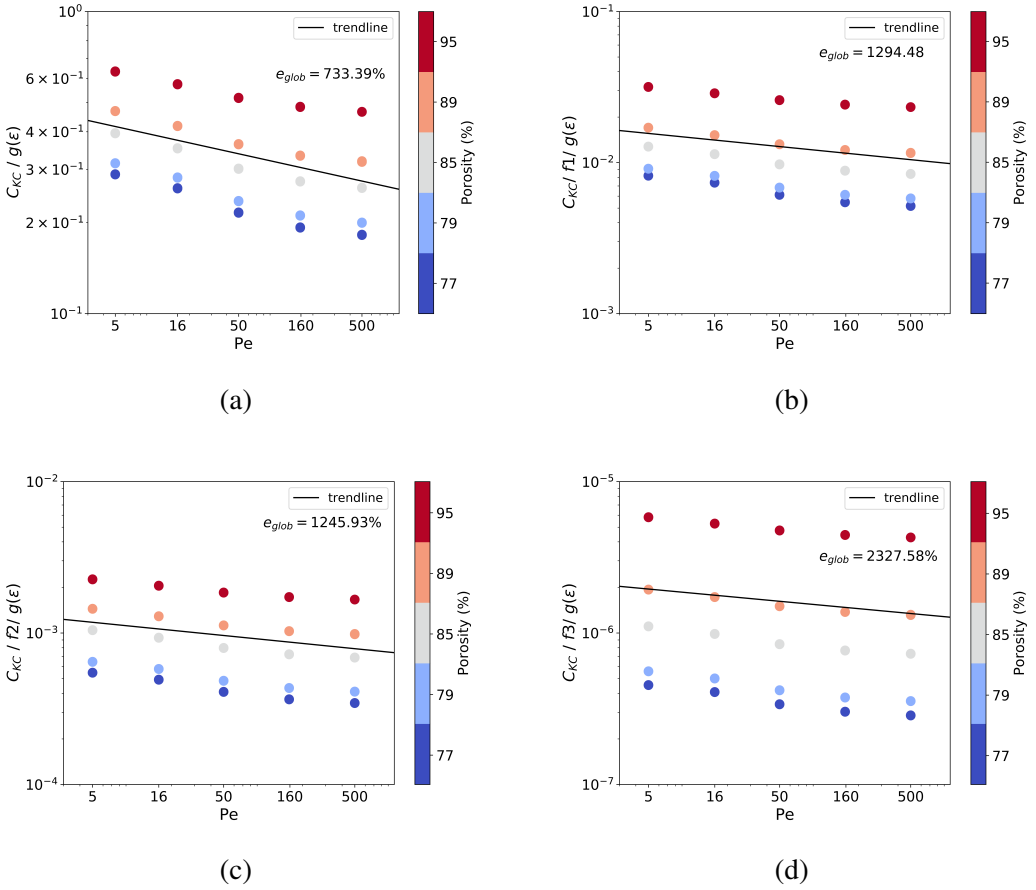

Fig. A.5 C_{KC} divided by Kuwabara correlation from Eq.(A.4) in (a). The dimensionless groups, derived by dividing by Eq.(A.1), Eq.(A.2) and Eq.(A.3), divided by Kuwabara correlation respectively in (b), (c) and (d)

$$As(\varepsilon) = \frac{2(1-\gamma^5)}{2-3\gamma+3\gamma^5-2\gamma^6}, \text{ with}$$
$$\gamma(\varepsilon) = (1-\varepsilon)^{\frac{1}{3}} \tag{A.5}$$

These functions were applied to all the previously obtained groups, namely C_{KC} and the ones obtained with f_1, f_2, f_3. The results relative to Eq.(A.4) are reported in Figure A.5(a - d) and the ones relative to Eq.(A.5) are reported in Figure A.6 (a - d). Once again, the resulting fitting error for all these combinations is very high and, thus, it is clear that the approaches applied thus far were not able to extract any relevant correlation between the macroscopic parameters and the results for the mass transfer simulations.

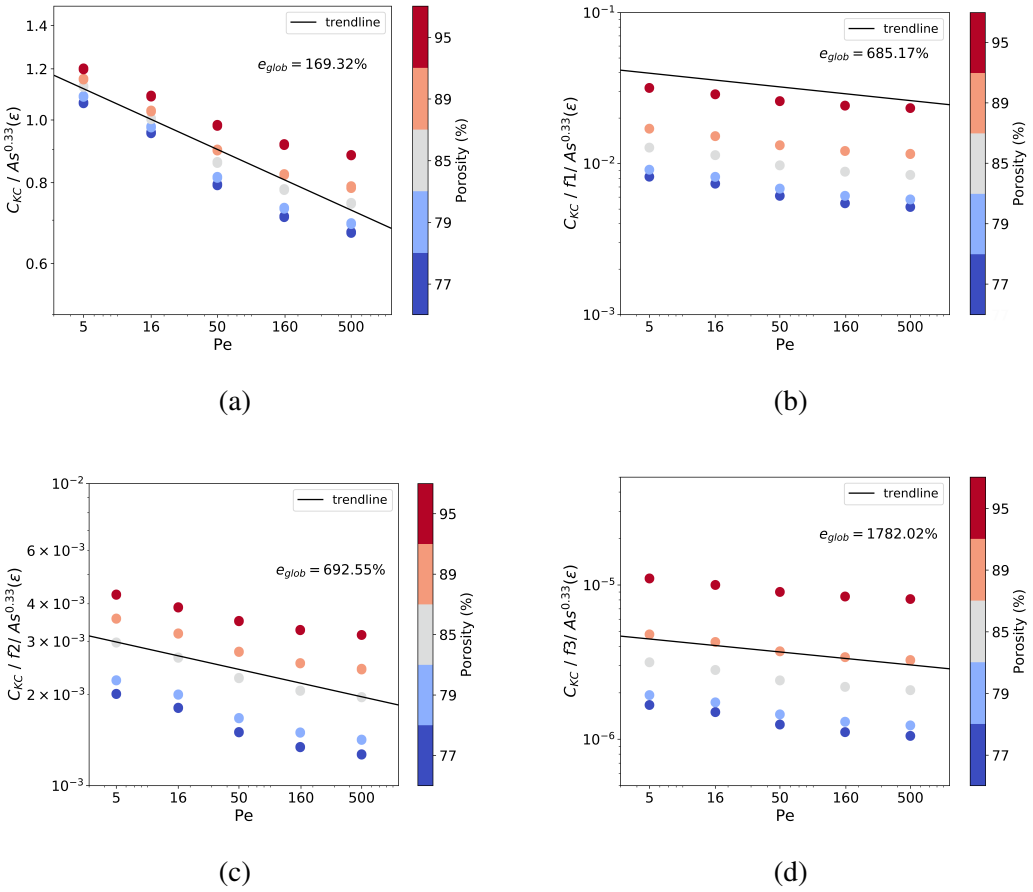

Fig. A.6 C_{KC} divided by Happel correlation from Eq.(A.5) in (a). The dimensionless groups, derived by dividing by Eq.(A.1), Eq.(A.2) and Eq.(A.3), divided by Happel correlation respectively in (b), (c) and (d)

A.2.3 Results analysis: fitting error optimization with arbitrary, geometric-dependent, functional forms

The final approach taken into account was to try to find a functional form dependent on ε, τ, or S_V which could result in minimal error. The obvious choice for this *functional form* analysis fell on the power-law, which allows to vary the exponent n in a wide range. The functions used are reported in Eq.(A.6), A.7, A.8:

$$h(\varepsilon) = \varepsilon^n \tag{A.6}$$

$$h\left(S_{V,bulk}\right) = {f_1}^n = \left(S_{V,bulk} \cdot d_p\right)^n \tag{A.7}$$

$$h(\tau) = \tau^n \tag{A.8}$$

where $n \in \mathbb{R}$ is the exponent. The results of this error optimization operation are reported in the Figures A.7(a - f), which show the global $e_{r,glob}$ as function of the porosity ε. These plots clearly shows how none of the functions in Eq.(A.6), A.7, A.8 is able to reduce the error to an acceptable value. The results that come from employing functional forms of functional forms of the macroscopic parameters, such as porosity, specific surface, or tortuosity alone are not enough to derive macroscopic relation to describe the particle deposition during early filtration.

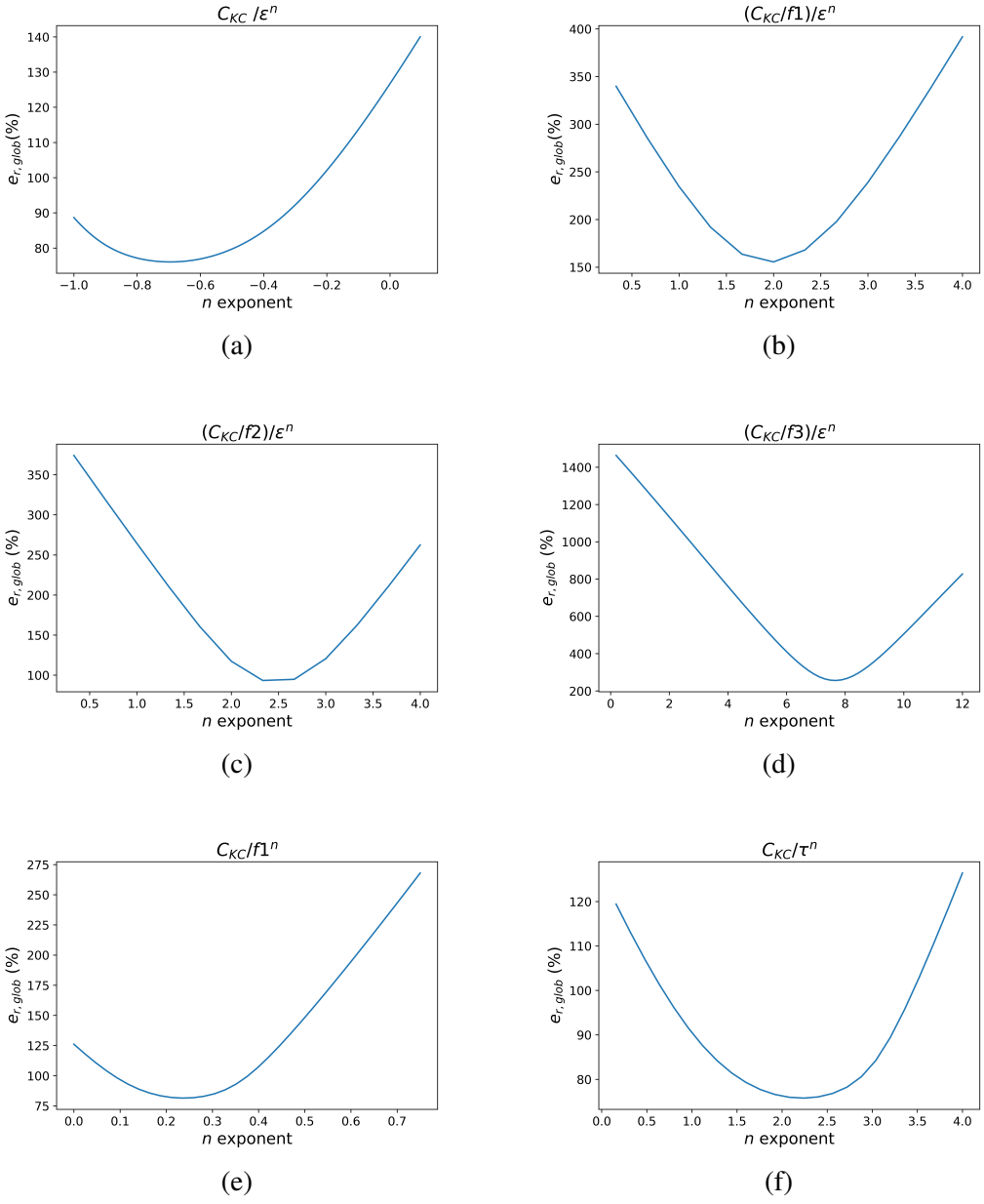

Fig. A.7 The global error trend as a function of the exponent n for the functional form reported in Eq.(A.6), Eq.(A.7) and Eq.(A.8).